FAST ALGORITHM AND SURFACE INTEGRAL EQUATIONS FOR TWO-DIMENSIONAL MATERIALS MODELING

BY

LINGLING MENG

DISSERTATION

Submitted in partial fulfillment of the requirements
for the degree of Doctor of Philosophy in Electrical and Computer Engineering
in the Graduate College of the
University of Illinois Urbana-Champaign, 2021

Urbana, Illinois

Doctoral Committee:

Professor Weng Cho Chew, Chair
Professor Erhan Kudeki
Professor Jose E. Schutt-Aine
Associate Professor Wenjuan Zhu

ABSTRACT

In this dissertation, a wide-band two-dimensional (2D) fast multipole algorithm (FMA) with a novel diagonalization form is presented. The conventional diagonalization of 2D FMA can be derived based on the interpretation of Parseval's theorem. The performance of FMA in the twilight zone (between the low-frequency and high-frequency regimes) is not good enough. By scaling special functions and applying discrete Fourier transform (DFT), the multipole expansions with dense matrices can be transformed to diagonal matrices with stable accuracy. Therefore a broadband 2D FMA with high efficiency and accuracy is achieved with a multi-level scheme.

Then a metasurface platform to generate structured light at second harmonics is proposed with transition-metal dichalcogenide (TMDC) flakes. With the aid of the electric field integral equation and impedance boundary condition, the surface currents on TMDC flakes can be calculated at fundamental frequencies. By applying three-fold rotational symmetry of the quadratically nonlinear susceptibility of TMDC monolayer, radial (or azimuthal) polarization and orbital angular momentum can be generated at second harmonics with linearly polarized and circularly polarized incident wave at the fundamental frequency, respectively.

Finally, the radiative heat transfer between two graphene-wrapped objects with arbitrary shapes is studied by a fluctuating-surface current formulation derived from surface integral equations with impedance boundary conditions. The surface conductivity of graphene can be tuned by the temperature, chemical doping or electrical gating. The near-field thermal radiation can be enhanced due to graphene plasmonics in terahertz regime. Off resonance, the graphene coating has a shielding effect on the dielectric bodies containing fluctuating-current sources. This formulation can be extended to multi-body problem and other two-dimensional materials.

To my parents and Xinhao, for their love and support.

ACKNOWLEDGMENTS

Time flies. I still remember that evening in the summer of 2014 when I got off the bus at the campus of the University of Illinois Urbana-Champaign. The weather is totally different from that in Hong Kong, cooler and breezier. Before I joined the team at UIUC, I already knew some of them when I studied in the University of Hong Kong. This relaxed me a lot, and cheered me up.

Before I began my study here, I knew Prof. Weng Cho Chew in Hong Kong, a charming scientist with profound knowledge. I always dreamed to study on his team and learn from him. So when I got the news that he accepted my application, I was so excited and a bit nervous. His patient and careful guidance has changed my way of study and thinking, making me understand the essence of methodology and the significance of research. His enthusiasm and persistence with his deep insight in research make me learn the beauty of the connections between physics and mathematics, which would affect my career and life. "Do not dabble in the math, read the physics from it." "Always give credit to the one who owns it." ... These words definitely impressed me deeply, teaching me how to be a better researcher. I will always be grateful to Professor Chew for providing me this opportunity to study with him.

I would also like to thank Professor Li Jun Jiang and Professor Wei Sha for sharing their knowledge in my research projects, which broadened my view in these areas. I am very grateful to the professors in the department for their excellent courses and guidance. These lectures helped me to solidly understand electromagnetics and its applications in electromagnetics engineering, and inspired my interest in quantum physics. I would also like express my special appreciation to Professor Erhan Kudeki, Professor Jose Schutt-Aine and Professor Wenjuan Zhu for serving on my doctoral committee and offering valuable suggestions.

My colleagues and friends have been very helpful in many aspects. I would like to thank Dr. Tian Xia, Dr. Hui Gan, Dr. Aiyin Liu, Dr. Shu Chen, Dr. Qi Dai, Dr. Qin Liu, Dr. Xiaoyan Xiong, Dr. Joe Rutherford, Dr. Carlos Salazar-Lazaro, Dr. Thomas Roth, Mert Hidayetoğlu, Christopher Ryu, and Mike Wei for sharing their brilliant ideas and for their friendship.

My final gratitude goes to my parents and my husband Xinhao for their love and support. I met Xinhao on campus. We are both in the Department of Electrical and Computer Engineering. He has always been my best mate, sharing my happiness, encouraging and helping me whenever and wherever. All I can feel is that home is the warmest harbor.

TABLE OF CONTENTS

CHAPTER 1

INTRODUCTION

1.1 Introduction for Computational Electromagnetics

As computer techniques and scientific computation have developed by leaps and bounds, numerical methods for analysis of electromagnetics (EM) problems have gradually replaced traditional calculation methods that only solve for closed form and provide approximate solutions. These advancements have expanded the influence of computational electromagnetics (CEM), pushing the development of electrical engineering forward greatly [1].

In CEM, the existing numerical methods can be classified according to their computation domain, i.e., time domain or frequency domain. In the time domain methods, the finite-difference time domain (FDTD) method might be the earliest developed method and is very popular in transient simulations [2]. In the frequency domain methods, the finite element method (FEM) is the most widely employed in industry to deal with inhomogeneous medium problems [3]. Another powerful method is the method of moments (MoM) or the integral equation method, which is particularly well suited to open-region EM problems and usually formulated in the frequency domain [4, 5]. Methods in time domain may have their counterparts in frequency domain, and vice versa. For instance, there are the finite-difference frequency domain (FDFD), the time-domain finite element (TDFE) and time-domain integral equation (TDIE).

Alternatively, these methods can be sorted by the forms applied to solve the Maxwell equations, i.e., differential equation form or integral equation form. The former solves the Maxwell's equations in differential equation form directly, either by applying differentiation to electric field and magnetic field with time step (FDTD), or by using basis functions to represent electric or magnetic field with unknown coefficients to be solved (FEM). In the

integral equation form, the solution to the original problem is expressed as an integral equation with the Green's function as kernel by the principle of linear superposition.

Computational electromagnetics is never a simple research area. Instead, it is highly interdisciplinary, combining physics, mathematics and computer science tightly [1]. All the methods in CEM have their own merits and limits, which require a good understanding of these methods and their appropriate scenarios. Though the mainstream methods in CEM have been developed into commercial simulation software or CAD tools as mature techniques, there are still some new challenges in EM engineering as new materials emerge and new technology is acquired.

1.2 Integral Equations and Fast Multipole Algorithm

In this section, the integral equations and fast multipole algorithm are introduced briefly. Basically, there are two categories of integral equations: volume integral equations (VIE) and surface integral equations (SIE) [4]. In VIE, the volume of the object is discretized into small volumetric simplexes; therefore it can deal with inhomogeneous objects. In contrast, in SIE only the surface is discretized and the unknowns reside on the surface of the object. Hence, it can only solve homogeneous objects, but the workload can be reduced greatly compared to VIE due to reduced unknown count. Both VIE and SIE have several variations, depending on the EM problems to be solved. Important advances in this area have overcome a lot of challenges, such as eliminating internal resonances by combining electric-field and magnetic-field integral equations, designing appropriate basis functions to deal with the low-frequency breakdown issue, employing pre-conditioners in iterative solver, etc.

Both VIE and SIE have the Green's function as the integral kernel. Due to limited space, here we will just discuss the cases that are employed in this dissertation, i.e., three-dimensional SIE and two-dimensional VIE. A two-dimensional (2D) VIE for scattering problem can be expressed as:

$$\phi^{inc}(\boldsymbol{\rho}) = \phi(\boldsymbol{\rho}) - \int_V d\boldsymbol{\rho}' H_0^{(1)}(\boldsymbol{\rho}, \boldsymbol{\rho}') O(\boldsymbol{\rho}') \phi(\boldsymbol{\rho}'), \tag{1.1}$$

where $H_0^{(1)}(\boldsymbol{\rho}, \boldsymbol{\rho}')$ is the Green's function in the 2D case, and $O(\boldsymbol{\rho}') = k^2(\boldsymbol{\rho}') - k_b^2$ is the contrast or object function with respect to the background medium for representing the inhomogeneity. In Chapter 2, we will use Eq. (1.1) to calculate E_z in the TM modes (E_z, H_x, H_y) for applications in photonic crystals. The simplest SIE is the EFIE to the solve scattering problem of a perfect electric conductor (PEC):

$$-\mathbf{E}^{inc}(\mathbf{r}) = i\omega\mu \int_S \overline{\boldsymbol{G}}(\mathbf{r}, \mathbf{r}') \cdot \mathbf{J}_s(\mathbf{r}'), \tag{1.2}$$

where $\overline{\boldsymbol{G}}(\mathbf{r}, \mathbf{r}')$ is the dyadic Green's function and $\mathbf{J}_s(\mathbf{r}')$ is the surface current with $\mathbf{r}'$ on the inner surface of the PEC. In Chapters 3 and 4, more details of SIE will be discussed to solve structures with two-dimensional materials.

To numerically solve the integral equations, the method of moments transforms the governing equation into a matrix equation by expanding the unknowns with basis functions and then testing the system with testing functions. Therefore, the computational complexity of $O(N^2)$ is inevitable when calculating all mutual interactions in the Green's function. Multi-level fast multipole algorithm is a multi-level scheme to calculate the interactions efficiently based on the addition theorem and the Green's function. The computation complexity can be reduced to $O(N\log N)$ or $O(N)$ [1].

The 2D FMA and 3D FMA share the same interpretation of physics. The low-frequency FMA (LF-FMA) and multi-level FMA (MLFMA, conventionally is applied in middle frequency) manifest two very different forms, i.e., multipole expansions and plane wave expansions, although both of them are marked with the term "FMA". The multipole expansions require high-order multipoles to achieve certain accuracy as the frequency goes high, making computation workload unaffordable. The plane wave expansions have low-frequency breakdown issue due to inability to capture the evanescent waves as the frequency goes low. As a result, LF-FMA and MLFMA can operate in their respective regimes efficiently, but are not applicable in the other regime. Later a novel mixed-form FMA (MF-FMA) was proposed to provide a complete solution for wide-band applications. The MF-FMA contains transformers between multipoles and plane waves [6]. Hence, it combines both expansions into one oct-tree browsing process to cover both low and middle frequencies efficiently. However, the accuracy in the transition region (called the twilight zone between low and middle frequencies) is not very

satisfactory. For 3D FMA, to expedite efficiency, a rotation technique can be applied to multipole expansions, making the original dense matrices sparse [7]. Therefore, multipoles with high orders can be used in the expansion and maintain the accuracy in the twilight zone. Another novel hybridization of the multipole and plane wave expansions for broadband simulation is proposed by separating evanescent and plane waves explicitly within FMA [8]. In this dissertation, the 2D FMA is revisited and a novel diagonalization is introduced, due to the demands in recent applications, such as photonic crystals with inhomogeneous medium and imaging with inverse scattering problems [9].

1.3 Surface Integral Equations for Two-dimensional Materials

Emerging two-dimensional materials have drawn a lot of attention. Basically they can be classified into two categories [10]. One is graphene (monolayer of graphite), and the other is transition-metal dichalcogenide monolayer. The former is centro-symmetric and has strong third-harmonic generation. The latter is noncentro-symmetric and has strong second-harmonic generation. Since they have thickness of atomic level and proper conductivity, it is best to model the monolayer as a conducting surface. Therefore, the surface integral equation is applicable in solving models with two-dimensional materials. We have studied two scenarios for 2D materials according to their electrical and optical properties with surface integral equations.

For the noncentro-symmetric material, we focus on its second-harmonic generations since they have strong quadratically nonlinear susceptibility [11]. A metasurface platform to generate structured light at second harmonics is designed. To simplify the modeling and exclude the effects from substrate, the metasurface composite with TMDC flakes is suspended in the air. The electric field integral equation with impedance boundary condition is used to calculate the surface current on each flake at the fundamental frequency. Then the electric currents at second harmonics are calculated by the relation between second-order currents and the electric fields at fundamental frequency. Furthermore, the scattered electromagnetic fields at second harmonics are obtained by the corresponding operators.

For the centro-symmetric material, i.e., graphene, we study the radiative heat transfer between two graphene-wrapped objects in the interest of the graphene plasmonics in that regime. In this configuration, a PMCHWT form with impedance boundary conditions is required for the existence of dielectric bodies and the surface conductivity of graphene. Two kinds of the fluctuating sources are considered: one is from the dielectric body due to the complex permittivity, and the other is from the graphene layer due to the complex surface conductivity. To maintain the flux reciprocity between the object of sources and the object absorbing the power, the matrix of the system should be symmetric. More details will be discussed in Chapter 4.

1.4 An Overview of the Dissertation

Fast algorithms and surface integral equations in computational electromagnetics with new applications are studied in this dissertation.

In Chapter 2, a wide-band two-dimensional fast multipole algorithm (2D-FMA) with a novel diagonalization form is presented. Invoking Parseval's theorem and scaling the special functions, the new 2D-FMA is highly efficient and accurate for broadband. Applying the 2D-FMA into VIE (volume integral equation), the performance has been demonstrated in the study of photonic crystal defects and waveguides.

In Chapter 3, a metasurface platform based on transition-metal dichalcogenide flakes is designed to generate structured light at second-harmonic frequency. The electric field integral equation (EFIE) with impedance boundary condition is introduced to calculate the surface currents at the fundamental frequency, which will be used to obtain the scattered electric field at the second-harmonics. Both radial and azimuthal polarizations can be generated when the incident wave at the fundamental frequency is linearly polarized. Orbital angular momentum with several modes can be generated when the incident wave is circularly polarized.

In Chapter 4, we propose a PMCHWT form based method to study the heat transfer problem for graphene-wrapped objects with arbitrary shapes. The scattering problem for a graphene-wrapped sphere is analyzed first for the benchmark operators established. Then the fluctuating-surface-current formulation of radiative heat transfer for two dielectric objects is revisited.

This formulation is extended to the scenarios when the dielectric objects are coated with graphene layers by applying the operators verified in the scattering problem and the two-dimensional fluctuation-dissipation theorem. Numerical results demonstrate the reciprocity of fluxes for the two objects.

Finally we draw the conclusions in Chapter 5 and propose some possible future work.

CHAPTER 2

A WIDE-BAND TWO-DIMENSIONAL FAST MULTIPOLE ALGORITHM WITH A NOVEL DIAGONALIZATION FORM

2.1 Introduction

The fast multipole algorithm (FMA) has been proposed for two decades since its initial version for solving coulombic interactions in large-scale particle problems [12, 13]. A lot of research has made contributions to the study in FMA, among which the multi-level FMA with interpolation and anterpolation is the most popular [1, 14], which has been extended to mixed-form FMA and applied to dielectric problems [7, 15]. It can be used to solve problems of three billion unknowns with the advancements in parallel computer hardware and efficient implementations [16]. Less attention is paid to the two-dimensional (2D) FMA, since it is easier, less complicated and even less applicable to real world situations than the 3D counterpart. A normalized plane-wave method for 2D Helmholtz problems has been proposed for a wide-band algorithm [17]. Recent studies in devices with dielectric materials and imaging with inverse scattering problems require a fast and efficient algorithm for inhomogeneous media. The 2D FMA with the plane-wave expansion has been successfully incorporated for fast full-wave tomographic image reconstruction, where the Helmholtz equation is solved without any approximation [18]. However, these implementations suffer from low-frequency breakdown and therefore cannot be employed for many ultrasound and seismic imaging methods where the incident wave is a pulse with a wide bandwidth. Therefore a scalable, wide-band FMA solver is highly desirable for real-world imaging applications. Besides, the study of the 2D FMA provides insights for the solutions to 3D case as they share the same physics.

The addition theorem applied to the Green's function can be interpreted as Parseval's theorem in Fourier transform for 2D cases [1]. This naturally leads to the two forms of FMA, i.e., multipole expansion in coordinate space and

plane-wave expansion in Fourier space. Then the diagonalization of FMA from a dense matrix in the multipole expansion to a diagonal matrix in the plane-wave expansion can be taken as the transformation of a convolution in coordinate space to an ordinary multiplication in Fourier space, which reduces the computational complexity greatly. The plane-wave expansion has the low-frequency breakdown issue due to its failure to capture the evanescent spectra. Mathematically, this issue is caused by a finite summation of Hankel functions with extremely large values when the argument is close to the singularity point. Meanwhile the multipole expansion is inefficient at high frequencies, since more higher order multipoles are required which adds an impractical cost in the computation of dense matrices. Therefore, a twilight zone exists between the low-frequency and high-frequency regimes, where the FMA is not that accurate or not efficient. Similar scenarios exist in 3D case. A broadband 3D FMA can be achieved by the enhanced mixed-form FMA with rotation matrices in high-order multipoles [7], or by the approximated diagonalization of the Green's function with normalization technique [19, 20]. The spectral representation of the Green's function can also achieve a broadband scheme by expressing the fields with both propagating and evanescent parts explicitly. To find an efficient integral path in spectral representation, it introduces direction-dependent integrals (six directions have to be considered) that require other techniques (like rotation [21], QR-algorithm [22]) or more memory storage and operations in the FMA procedure [23].

In this chapter, we focus on the 2D case due to its potential applications mentioned before. Besides, we prefer not to introduce the direction-dependent integrals; therefore, the spectral representation in 2D case is not considered here. To close the gap in the twilight zone, a novel diagonalization is proposed in this work based on the aforementioned idea of Fourier transform with scaled special functions. This is different from the derivations in [17], which inserted identities of Kronecker delta function. To clarify the novelty of our work, it is noted that, the proposed idea to achieve a broadband FMA is essentially different from the work in [19] (in which the approximated formulas of Bessel functions are used), though both of them use the normalization technique. The translators in multipole expansions are set up as a set of Fourier coefficients with a scaling parameter, so there is no longer a dense matrix. Then the subsequent aggregation, translation and disaggregation are calculated in Fourier space. Since the Hankel functions

have been normalized, the breakdown issue is overcome in the gap region with comparable complexity in the plane-wave expansion.

This chapter is organized as follows: Section 2.2 gives the derivation of this novel diagonalization and the numerical treatments. In Section 2.3, numerical analysis is provided. The proposed broadband FMA is applied to the volume integral equation (VIE) [24] to study the scattering of dielectric cylinders in 2D photonic crystals. The analysis of defect modes serves as the application in the low-frequency regime. On the other hand, the study of wave propagation in photonic crystal waveguides plays a role in the application for the high-frequency regime. Section 2.4 concludes the chapter and discusses extending the algorithm to the 3D case.

2.2 Theory of Combined-form Fast Multipole Algorithm

In this section, the conventional diagonalization in 2D FMA is briefly introduced based on the interpretation of Parseval's theorem. Then, the DFT-FMA is proposed with scaled special functions. Afterwards, its extension to multi-level structures and conversion to the plane-wave expansion are given.

2.2.1 Parseval's Theorem and Diagonalization in FMA

In Fourier transform. Any arbitrary periodic function can be expressed as a Fourier series:

$$F(\phi) = \sum_{n=-\infty}^{+\infty} f_n e^{in\phi}, \tag{2.1}$$

where f_n is the set of Fourier coefficients. Assume $G(\phi)$ is another periodic function expressible as:

$$G(\phi) = \sum_{n=-\infty}^{+\infty} g_n e^{in\phi}. \tag{2.2}$$

According to Parseval's theorem, we have

$$\sum_{n=-\infty}^{+\infty} f_n \overline{g_n} = \frac{1}{2\pi} \int_{-\pi}^{\pi} d\phi F(\phi) \overline{G(\phi)}, \tag{2.3}$$

where the horizontal bars indicate complex conjugation. Based on the above theorems, the multipole expansion of the Green's function can be diagonalized to plane-wave expansion by Fourier transform. According to the addition theorem, the factorization of Green's function has the following multipole expansion [1], if $\boldsymbol{\rho}_{ji} = \boldsymbol{\rho}_{jl'} + \boldsymbol{\rho}_{l'l} + \boldsymbol{\rho}_{li}$:

$$\begin{aligned} H_0^{(1)}(k\rho_{ji}) &= \sum_{m=-\infty}^{+\infty} J_m(k\rho_{jl'}) e^{im(\phi_{jl'}-\pi)} \\ &\cdot \sum_{n=-\infty}^{+\infty} H_{m-n}^{(1)}(k\rho_{l'l}) e^{-i(m-n)\phi_{l'l}} J_n(k\rho_{li}) e^{-in\phi_{li}}. \end{aligned} \tag{2.4}$$

The plane-waves for receiving and radiation patterns can be expressed as a Fourier series:

$$A(\phi) = e^{ik\rho_{jl'}cos(\phi-\phi_{jl'})} = \sum_{m=-\infty}^{+\infty} J_m(k\rho_{jl'}) e^{-im(\phi_{jl'}-\pi)} e^{im(\phi-\pi/2)} \tag{2.5}$$

$$= \sum_{m=-\infty}^{+\infty} a_m e^{im(\phi-\pi/2)} \tag{2.6}$$

and

$$D(\phi) = e^{-ik\rho_{li}cos(\phi-\phi_{li})} = \sum_{n=-\infty}^{+\infty} J_n(k\rho_{li}) e^{-in(\phi_{li})} e^{in(\phi-\pi/2)} \tag{2.7}$$

$$= \sum_{n=-\infty}^{+\infty} d_n e^{in(\phi-\pi/2)}, \tag{2.8}$$

where

$$a_m = J_m(k\rho_{jl'}) e^{-im(\phi_{jl'}-\pi)} \tag{2.9}$$

and

$$d_n = J_n(k\rho_{li}) e^{-in(\phi_{li})}. \tag{2.10}$$

are the Fourier coefficients. Note that a_m and d_n here are slightly different from the standard Fourier coefficients, since the basis used here is $e^{in(\phi-\pi/2)}$ instead of $e^{in\phi}$. Then the Green's function in Eq. (2.4) is actually expressed

by these Fourier coefficients:

$$H_0^{(1)}(k\rho_{ji}) = \sum_{m=-\infty}^{+\infty} a_m^* \cdot \sum_{n=-\infty}^{+\infty} H_{m-n}^{(1)}(k\rho_{l'l}) e^{-i(m-n)\phi_{l'l}} d_n. \tag{2.11}$$

The inner summation over n of Eq. (2.11) is a convolution which is a product in Fourier space. Denote the periodic function with Hankel functions inside Eq. (2.11) as Fourier series $C(\phi)$:

$$\begin{aligned} C(\phi) &= \sum_{n=-\infty}^{+\infty} H_n^{(1)}(k\rho_{l'l}) e^{-in\phi_{l'l}} e^{in(\phi-\pi/2)} &(2.12)\\ &= \sum_{n=-\infty}^{+\infty} c_n e^{in(\phi-\pi/2)}. &(2.13)\end{aligned}$$

Then, the product in Fourier space of the above convolution can be expressed as:

$$\begin{aligned} B(\phi) = C(\phi)D(\phi) &= \sum_{m=-\infty}^{+\infty} \Big(\sum_{n=-\infty}^{+\infty} c_{m-n} d_n \Big) e^{in(\phi-\pi/2)} &(2.14)\\ &= \sum_{m=-\infty}^{+\infty} b_m e^{in(\phi-\pi/2)}. &(2.15)\end{aligned}$$

Invoking Parseval's theorem to Eq. (2.11), the Green's function can be expressed as:

$$\begin{aligned} H_0^{(1)}(k\rho_{ji}) &= \sum_{m=-\infty}^{+\infty} \overline{a_m} b_m = \sum_{m=-\infty}^{+\infty} \overline{a_m} \Big(\sum_{n=-\infty}^{+\infty} c_{m-n} d_n \Big)\\ &= \frac{1}{2\pi} \int_0^{2\pi} d\phi \overline{A(\phi)} B(\phi) = \frac{1}{2\pi} \int_0^{2\pi} d\phi \overline{A(\phi)} C(\phi) D(\phi)\\ &= \frac{1}{2\pi} \int_0^{2\pi} d\phi e^{-ik\rho_{jl'} cos(\phi-\phi_{jl'})} \tilde{\alpha}(\phi) e^{-ik\rho_{li} cos(\phi-\phi_{li})}, &(2.16)\end{aligned}$$

where

$$\begin{aligned} \tilde{\alpha}(\phi) &= \sum_{n=-P}^{+P} H_n^{(1)}(k\rho_{l'l}) e^{-in\phi_{l'l}} e^{in(\phi-\pi/2)} &(2.17)\\ &= \sum_{n=-P}^{+P} H_n^{(1)}(k\rho_{l'l}) e^{-in(\phi_{l'l}-\phi+\pi/2)}, &(2.18)\end{aligned}$$

which is $C(\phi)$ with truncation. Rewriting Eq. (2.16), the diagonalization of multipole expansions can be achieved as

$$H_0^{(1)}(k\rho_{ji}) = \frac{1}{2\pi}\int_0^{2\pi} d\phi e^{-i\mathbf{k}\cdot\boldsymbol{\rho}_{jl'}}\tilde{\alpha}(\phi)e^{-i\mathbf{k}\cdot\boldsymbol{\rho}_{li}}, \tag{2.19}$$

which is also named as plane-wave expansions of the Green's function.

2.2.2 Diagonalization with Scaled Special Functions

Although the diagonalization of the multipole expansion reduces the computation cost greatly (from dense matrices to diagonal matrices), the plane-wave expansion has the low-frequency breakdown issue. This can be explained from two factors in mathematics: One is that the summation in $\tilde{\alpha}(\phi)$ [Eq. (2.18)] is divergent due to the singular property of Hankel function for small arguments. The other is the inaccuracy of extracting extremely small values from exponential functions (as the radiation pattern in plane-wave expansion) because of machine precision. A normalization technique can be applied to scale the Hankel function. However, if we normalize those Fourier coefficients, the analytical relation of Fourier pairs is not approachable. We can use discrete Fourier transform (DFT) to calculate the periodic functions in Fourier space numerically, by modifying a_m, c_n and d_n to standard form, i.e.,

$$a_m^{'} = J_m(k\rho_{jl'})e^{-im(\phi_{jl'}-\pi)}e^{-im\pi/2}, \tag{2.20}$$

$$c_n^{'} = H_n^{(1)}(k\rho_{l'l})e^{-in\phi_{l'l}}e^{-in\pi/2} \tag{2.21}$$

and

$$d_n^{'} = J_n(k\rho_{li})e^{-in(\phi_{li})}e^{-in\pi/2}. \tag{2.22}$$

Furthermore, we split the normalization into two parts based on the sign of the subscripts of Hankel functions. It is easier to see the cancellation of

the normalization from the multipole expansion of the Green's function:

$$H_0^{(1)}(k\rho_{ji}) = \sum_{m=-P}^{m=P} a_m t^{-m} \sum_{n=m-P}^{m+P} c_{m-n,m\geq n} t^{m-n} d_n t^{+n} + \sum_{m=-P}^{m=P} a_m t^{+m} \sum_{n=m-P}^{m+P} c_{m-n,m<n} t^{n-m} d_n t^{-n}, \tag{2.23}$$

where t is the normalization factor ($0 < t \leq 1$). The value of t is determined according to the asymptotic form of the Hankel function and its maximum value for a certain argument as $t = (C_{max}/|H_P|)^{1/P}$, where C_{max} is a preset constant used to confine the maximum magnitude of the Hankel function within the range $0 \sim C_{max}$. For instance, C_{max} can be set as $1.0E2$, then the magnitude values of all the normalized Hankel functions are smaller than $1.0E2$, eliminating those extremely large values in unnormalized Hankel functions.

To apply DFT, the normalized Fourier coefficients for the positive part are

$$\hat{a}_m^+ = a_m^{'} t^{-m} = J_m(k\rho_{jl'}) e^{-im(\phi_{jl'}-\pi)} e^{-im\pi/2} t^{-m}, \tag{2.24}$$

$$\hat{d}_n^+ = d_n^{'} t^{+n} = J_n(k\rho_{li}) e^{-in(\phi_{li})} e^{-in\pi/2} t^{+n}, \tag{2.25}$$

$$\hat{c}_{n,n\geq 0}^+ = \begin{cases} H_n^{(1)}(k\rho_{l'l}) e^{-in\phi_{l'l}} e^{-in\pi/2} t^{+n}, & n \geq 0 \\ 0, & n < 0 \end{cases} . \tag{2.26}$$

For the negative part, we have

$$\hat{a}_m^- = a_m^{'} t^{+m} = J_m(k\rho_{jl'}) e^{-im(\phi_{jl'}-\pi)} e^{-im\pi/2} t^{+m}, \tag{2.27}$$

$$\hat{d}_n^- = d_n^{'} t^{-n} = J_n(k\rho_{li}) e^{-in(\phi_{li})} e^{-in\pi/2} t^{-n}, \tag{2.28}$$

$$\hat{c}_{n,n<0}^- = \begin{cases} 0, & n \geq 0 \\ H_n^{(1)}(k\rho_{l'l}) e^{-in\phi_{l'l}} e^{-in\pi/2} t^{-n}, & n < 0. \end{cases} \tag{2.29}$$

Now, we can write the diagonalization of normalized multipole expansions as

$$\begin{aligned} H_0^{(1)}(k\rho_{ji}) &= \frac{1}{2\pi}\int_0^{2\pi} d\phi \mathcal{F}\left[\hat{a}_m^+\right]^* \mathcal{F}\left[\hat{c}_{n,n\geq 0}^+\right] \mathcal{F}\left[\hat{d}_n^+\right] \\ &+ \frac{1}{2\pi}\int_0^{2\pi} d\phi \mathcal{F}\left[\hat{a}_m^-\right]^* \mathcal{F}\left[\hat{c}_{n,n<0}^-\right] \mathcal{F}\left[\hat{d}_n^-\right], \end{aligned} \tag{2.30}$$

where $\mathcal{F}$ denotes DFT. In implementation, we can use fast Fourier transform (FFT) to accelerate the algorithm further.

2.2.3 A Scheme for Wide-band Algorithm

The DFT-FMA has the same complexity with the plane-wave expansion. It is stable at low frequency where plane-wave expansion fails. Error analysis for one-level multipole expansion (named as LF-FMA in convention), DFT-FMA and plane-wave expansion can be found in Fig. 2.1 (b) where the worst case is studied (radiation and receiving points are the diagonal vertices of the buffer box as (a) shows).

The multi-level scheme makes the algorithm into a fast solver. Since the singular property of Hankel function is rather sensitive with the argument in low-frequency regime, different normalization factors should be used at each level. For one matrix-vector product operation (MVP), the radiation patterns start as unnormalized Fourier coefficients. During the process of aggregation, those Fourier coefficients from the children level are normalized in both negative and positive forms, then shifted with negative and positive outer-to-outer (o2o) translators. Then renormalization is applied to the aggregated radiation pattern, making them as unnormalized Fourier coefficients in the parent level.

Ideally, the set of Fourier coefficients recovered from the negative normalization should be equal to the set from the positive one. However, due to the finite machine precision, the re-normalization introduces errors (see Fig. 2.2).

The recovered coefficients can be obtained accurately by combining the left half from the positive normalization and the right half from the negative normalization (see the black cross line in Fig. 2.2). Assume $\{u_n\}$ is the set

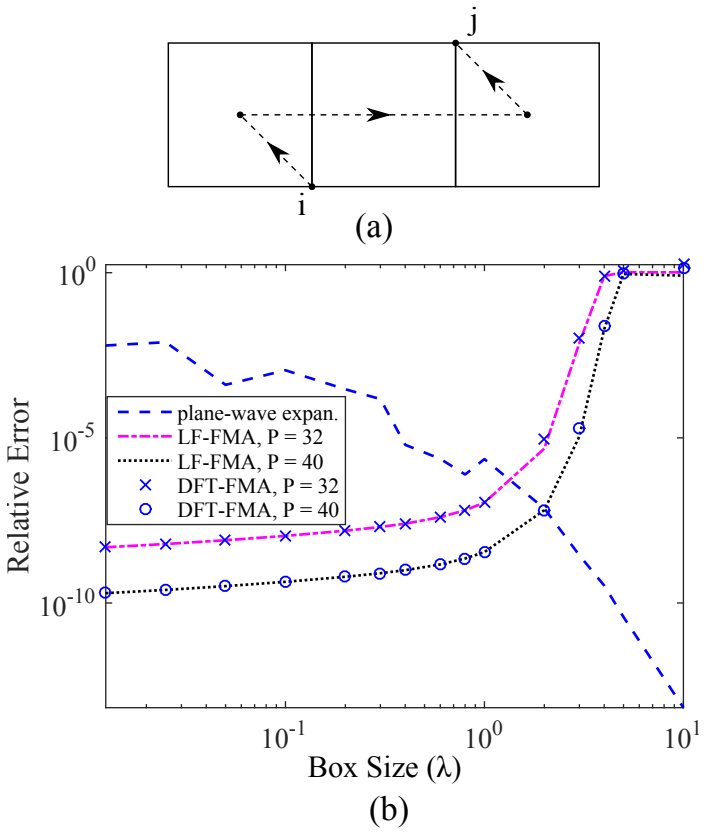

Figure 2.1: (a) Configuration of the test for a set of point-to-point. (b) Error comparisons for the one-level multipole expansion, DFT-FMA, plane-wave expansion.

of Fourier coefficients in the parent level, then the o2o translation can be expressed as the following compact form:

$$\begin{aligned}\{u_n\} \;=\; & [\bar{S}]\cdot\{t^{-n}\}\cdot[\bar{F}]^{-1}\cdot\tilde{\bar{\beta}}^{+}\cdot[\bar{F}]\cdot\{d_n' t^{+n}\}+[\bar{I}-\bar{S}] \\ & \cdot\{t^{+n}\}\cdot[\bar{F}]^{-1}\cdot\tilde{\bar{\beta}}^{-}\cdot[\bar{F}]\cdot\{d_n' t^{-n}\},\end{aligned} \tag{2.31}$$

where $[\bar{F}]$ and $[\bar{F}]^{-1}$ denote the operations of Fourier transform and inverse Fourier transform, respectively. Symbolic matrices $[\bar{S}]$ and $[\bar{I}-\bar{S}]$ represent the manipulation of taking the proper half parts from the negative and positive renormalized coefficients.

A similar process happens during the outer-to-inner (o2i) translation in the DFT-FMA. When the ratio of box size over the wavelength at a certain level enters the middle frequency regime (for instance, the ratio of 2.0 in Fig. 2.1), no normalization is required, since the plane-wave expansion works very

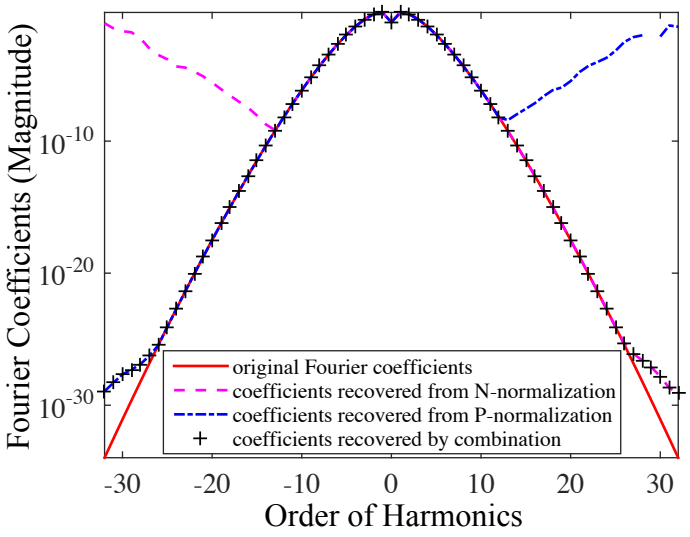

Figure 2.2: Comparison of the Fourier coefficients recovered from DFT-FMA.

well. Then the stored Fourier coefficients are transformed to the plane-wave form followed by the o2o shifting. Figure 2.3 shows the relative error of the radiation pattern generated from the combined coefficients, recovered coefficients only from the negative normalization and recovered coefficients only from the positive normalization in reference to the analytical plane-wave expression. It can be found that the conversion from the DFT-FMA to the plane-wave expansion is highly accurate.

It should be noted that the disaggregation part is the transpose conjugate of the aggregation part, and thus we can arrive at a wide-band multi-level algorithm with high accuracy.

2.3 Numerical Results

Numerical analyses of the pure DFT-FMA and the aforementioned FMA with combination of different forms (denoted as comb-form-FMA, in which the DFT-FMA serves in the transition region between the multipole expansion and the plane-wave expansion) are given in this section. Then, this new wide-band fast technique is applied to VIE to solve the scattering problems of dielectric cylinders in 2D photonic crystals.

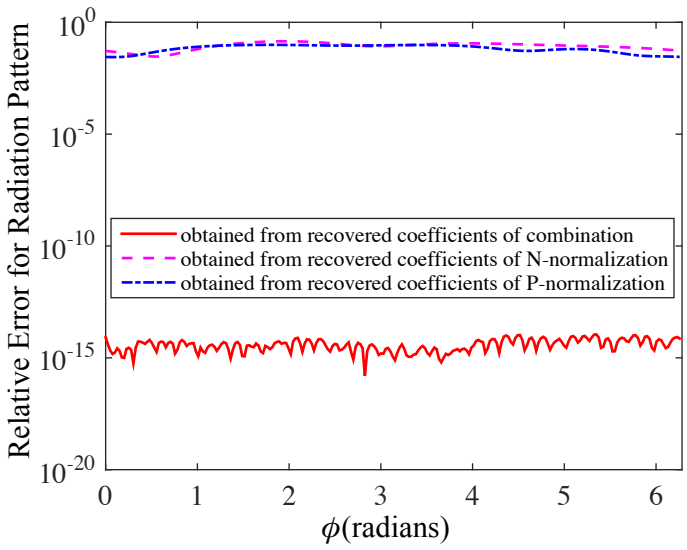

Figure 2.3: Relative error of radiation patterns generated from the recovered coefficients in Fourier space.

2.3.1 Complexities and error analysis of DFT-FMA

First, we compare the performance of the DFT-FMA with the multipole expansion by changing the number of levels when the leaf box size is fixed (this changes the number of unknowns). The source points and field points are distributed on each grid of the whole domain. A simple illustration of the multi-level structure is given in Fig. 2.4, where only partial points are shown. Figures 2.5 and 2.6 show the normalized memory cost and time cost for FMA setup with the number of harmonics of 32, 40, 58. It can be seen that the DFT-FMA reduces both the memory and time cost greatly. Larger number of harmonics results in larger difference. The normalized time cost in MVP is in Fig. 2.7, in which the difference between the LF-FMA and the DFT-FMA is not as huge as the time cost in FMA setup due to the computation of normalization and renormalization, FFT and inverse FFT for each translation.

The error analysis can be found in Fig. 2.8 with the number of levels as 4. Similar to the error of the one level case (see Fig. 2.1) in previous section, the plane-wave expansion has the low-frequency breakdown issue and the LF-FMA is inefficient in the middle frequency regime. However, the comb-form-FMA works well for the whole range of frequency. Note that, the accuracy of comb-form-FMA is slightly lower than the LF-FMA. This

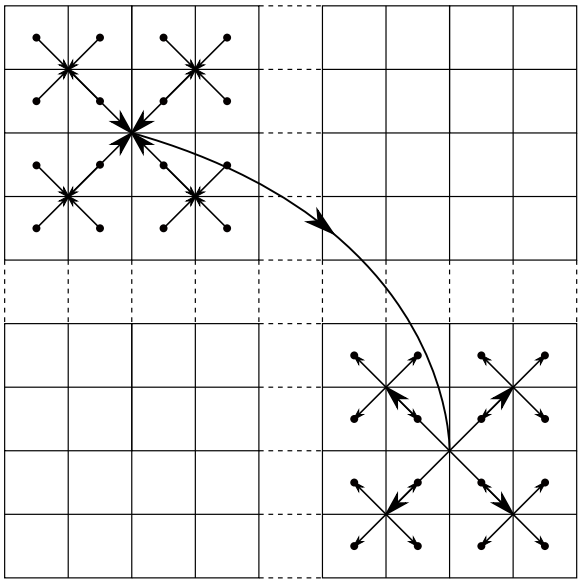

Figure 2.4: Multi-level structure for two-dimensional fast multipole algorithm. Partial points are shown here.

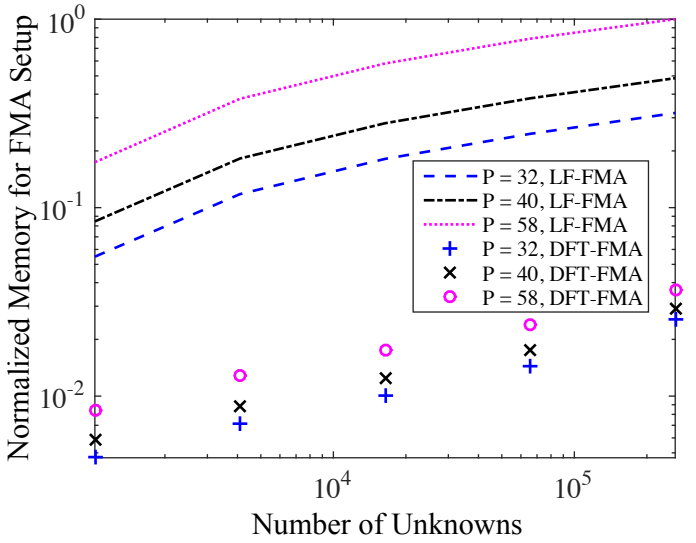

Figure 2.5: Normalized memory for FMA setup in the LF-FMA and the DFT-FMA.

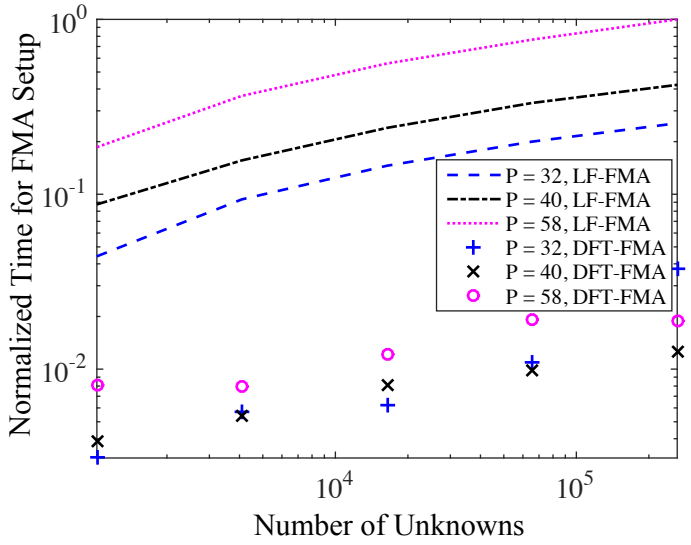

Figure 2.6: Normalized time cost for FMA setup in the LF-FMA and the DFT-FMA.

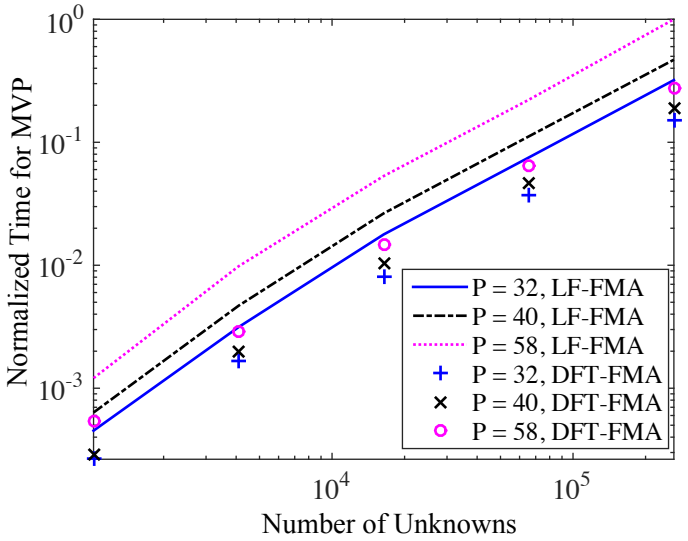

Figure 2.7: Normalized time cost for MVP in the LF-FMA and the DFT-FMA.

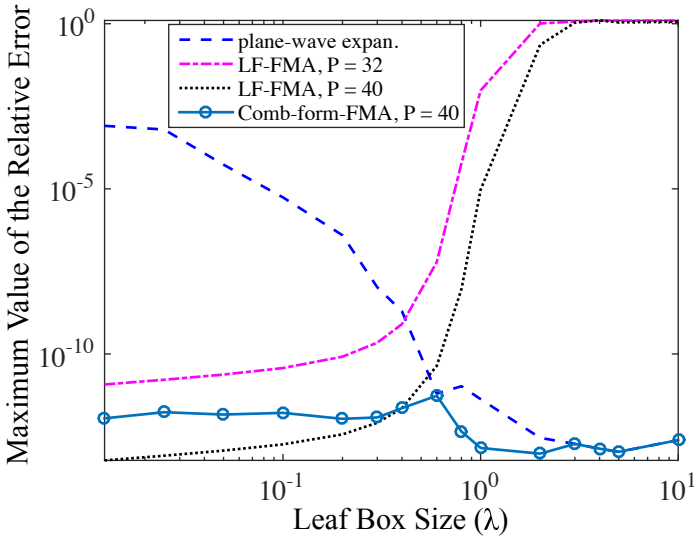

Figure 2.8: Maximum relative error for the plane-wave expansion, the LF-FMA and the comb-form-FMA. For the comb-form-FMA, the number of harmonics is 40.

is because the machine precision of the inverse FFT cannot recover those extremely small values in the radiation pattern (or the receiving pattern). Overall, the comb-form-FMA can achieve a wide-band algorithm with high accuracy and less computation cost.

2.3.2 Defect modes in photonic crystals

The defect modes are the localized states in the band gap that can be generated by a point defect. To verify that the proposed DFT-FMA works well in the low-frequency regime, we apply it to the VIE to identify the defect modes in 2D photonic crystals (on $x-y$ plane). Here the TM modes ($\{E_z, H_x, H_y\}$) are studied as an example. All the modes can be excited by an incident plane wave along a non-symmetric direction of the crystal [25]. We choose the incident angle of the plane wave to be 60° to excite all the modes. The 2D photonic crystals with a defect at the center can be found in Fig. 2.9 (a), containing GaAs rods with the permittivity of 11.56. The radii of the defect rod and the regular rod are $0.6a$ and $0.2a$, where the lattice length a is $1\mu m$. Note that, for our simulation, a supercell approach is adopted. In FMA, the ratio of the box size over the wavelength at the leaf level is set as 0.025 with the resolution of the grids as 0.0025. The number of levels is 7. By choosing

the normalized frequency $\omega a/2\pi c$ to be 0.2970, 0.3190, 0.3345 and 0.3916, we can excite quadrupole (odd-odd), quadrupole (even-even), monopole (second order) and hexapole (even-odd) (see Fig. 2.9 (b)-(e) where E_z is plotted). The "odd/even-odd/even" represents the properties of symmetry to axes x and y. The results match the data from [25] well.

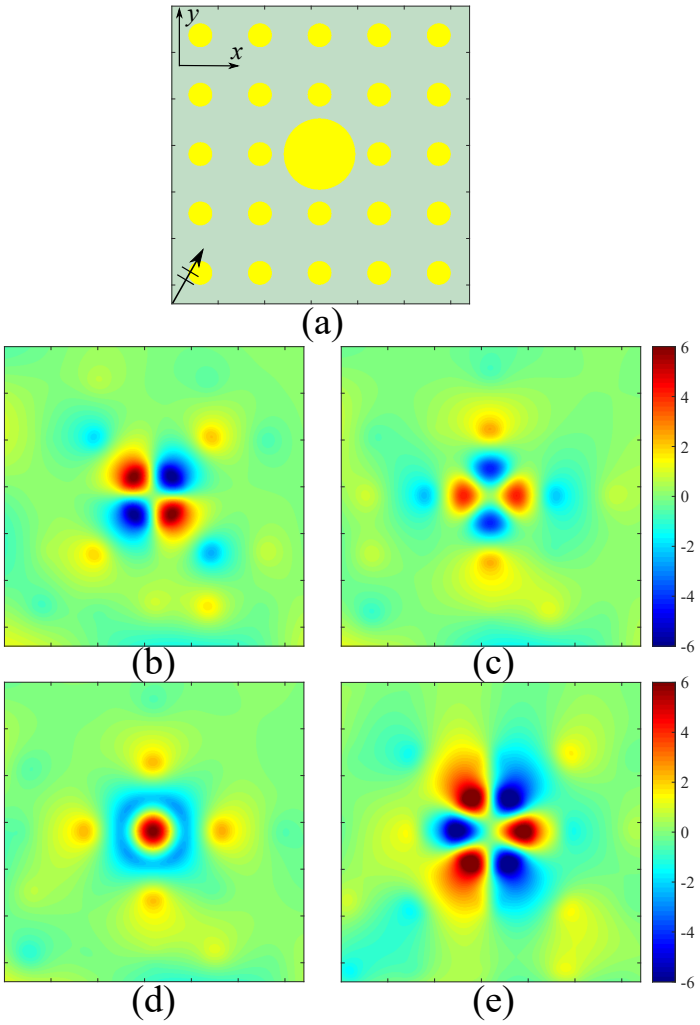

Figure 2.9: (a) Illustration of photonic crystals with a centered defect. (b) Mode 1: quadrupole (odd-odd). (c) Mode 2: quadrupole (even-even). (d) Mode 3: monopole (2^{nd} order). (e) Mode 4: hexapole (even-odd).

2.3.3 Photonic crystal waveguide

Now we study the application of this broadband algorithm in the long wavelength regime. The photonic crystal waveguide with a sharp bend proposed

in [26] is studied to observe the high transmission of light. Similarly, the TM modes are analyzed in this scenario. The configuration of the photonic band-gap waveguide is given in Fig. 2.10 (a). The radius of the GaAs rods is $0.18a$, where a is the lattice constant.

In the setup of FMA, the ratio of the box size to the wavelength (λ) is 0.04 at the leaf level. The number of levels is 8, therefore the whole computation domain is $5.12\lambda \times 5.12\lambda$. A point source is placed at the center of the input port. Highly efficient transmission can be achieved when the normalized frequency $\omega a/2\pi c$ is set as 0.353. It is consistent with the results in [26]. Figures 2.10 (b)-(d) show the energy of the field, the incident field and the total field in the waveguide, respectively. Combined with previous

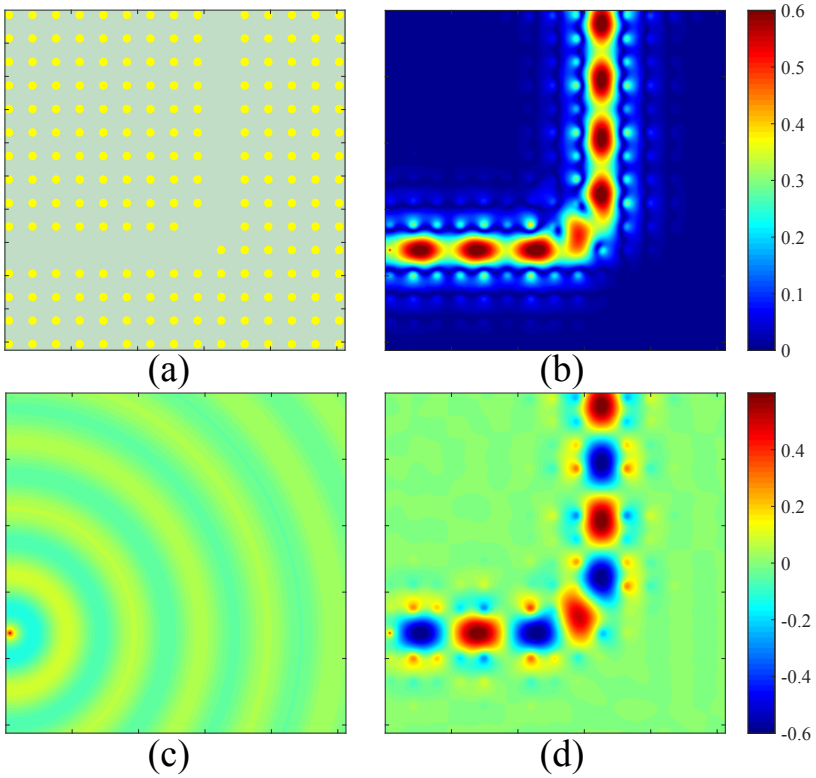

Figure 2.10: (a) Illustration of photonic waveguide structure. (b) Energy plot. (c) Incident wave by a point source. (d) Total field.

simulations, we can see that the broadband FMA can work well in both sub-wavelength and long wavelength problems.

2.4 Conclusion

In this chapter, a novel diagonalization for 2D FMA is proposed to achieve a highly efficient and accurate broadband FMA. Numerical analyses of the proposed FMA with the applications in photonic crystals demonstrates its performance completely. The derivation, based on Parseval's theorem, provides insights for 3D FMA, in which the spherical harmonic transform can be taken as the counterpart of Fourier transform.

CHAPTER 3

SECOND-HARMONIC GENERATION OF STRUCTURED LIGHT BY TRANSITION-METAL DICHALCOGENIDE METASURFACES

3.1 Introduction

It is well known that plane waves have independent degrees of freedom including frequency, amplitude, polarization, and phase. Fundamentally different from plane waves, structured light has inhomogeneous and correlated amplitude, polarization and phase. As additional degrees of freedom, the spatially inhomogeneous fields occur at the subwavelength scales of nano-optics due to the strong spin-orbital coupling, when polarized photons interact with inhomogeneous media [27]. Structured light including Hermite-Gaussian and Bessel beams [28, 29], Laguerre-Gaussian beams [29, 30] with helical phasefront carrying orbital angular momentum (OAM), and radially and azimuthally polarized vector beams [31, 32] brings novel functions to optical nano-devices and advances important applications in optical and quantum manipulation, microscopy, imaging, sensing, and communications [33]. For example, the radially polarized beam has been applied to high-resolution imaging attributed to its tighter focusing spot [34]. It can also be used in trapping nanoparticles since the beam exerts a larger longitudinal force on the particles [35]. Moreover, single-molecule localization microscopy [36] and a particle exchanger [37] employ the azimuthally polarized beam. Additionally, recent studies show potential applications of structured light in optical communications to gain communication channels through 'mode-division multiplexing' [38, 39].

One of the tools to generate structured light is based on bulk materials and volumetric structures [40, 41, 42, 43, 44]. However, the diffraction effect often makes on-chip integration of these bulk devices impossible. Alternatively, a metasurface [45, 46, 47] that is a planar structure locally modifying the spatial pattern of light in reflection or transmission offers inspiring solutions to tackle

the problem. It not only opens new paradigms for generating structured light at fundamental and high harmonics [48, 49, 50], but also deepens the physical understanding of linear and nonlinear spin-orbit interaction of light at subwavelength scales [51, 52, 53, 54, 55, 56, 57, 58, 59, 60]. Metasurfaces based on van der Waals materials have been reported for controlling light in linear optics [61, 62]. Most previous work on nonlinear generation of structured light is based on geometric configuration of the meta-atoms (like split resonant rings, U-shaped resonators, etc). Very recently, the nonlinear generation of structured light by hybridized metasurfaces of two-dimensional (2D) materials and plasmonic nanostructures is reported in [63, 64].

In this chapter, we propose a 2D material based metasurface platform to generate structured light at second harmonics. The meta-atoms of the metasurface are the transition-metal dichalcogenide (TMDC) flakes exhibiting the anisotropic second-order susceptibility and three-fold rotation symmetrical crystalline structure. The TMDC monolayer has strong second-harmonic generation (SHG) due to absence of inversion symmetry. The WS_2 adopted in this work has effective bulk quadratic nonlinear susceptibility comparable to that of GaAs (a medium with strong bulk SHG) in visible regime [10]. Using identical meta-atoms with tailored translations and orientations, the metasurfaces could generate radially and azimuthally polarized beams and vortex beams carrying OAM at second-harmonic frequencies. Different from [63, 64], we make use of all-TMDC flakes to generate a variety of structured light, which allows for ultra-thin metasurface designs. This characteristic can satisfy the requirements for ultra-compact sources of structured light in many evolving applications [39]. Furthermore, the TMDC based metasurface is compatible with a CMOS fabrication process [65, 66]. Therefore, the metasurface composed of TMDC flakes may become a competitive platform for generation of structured light at second harmonics.

This chapter is organized as follows: Section 3.2 gives the derivation of the three-fold rotational symmetry of the second-harmonic generation for TMDC monolayer. The electric field integral equation (EFIE) is introduced to calculate the surface currents at fundamental frequency, which will be used to obtain the scattered electric field at second harmonics. In Section 3.3, the design procedure for the metasurface platform is provided. Structured light (radial polarization, azimuthal polarization, orbital angular momentum) at second harmonics is achieved. Section 3.4 concludes the design of metasurface

and discusses the potential applications.

3.2 Theory and Methods

In this section, we provide the derivation of the three-fold rotational symmetry of the second-harmonic generation for TMDC monolayer. The electric field integral equation is applied to demonstrate this property numerically.

3.2.1 Second-harmonic generation of TMDC monolayer

The 2D TMDCs are semiconducting materials which render themselves particularly suitable for use in nanoscale light management in optical and optoelectronic devices. They have noncentrosymmetric atomic lattices, and thus allow even-order nonlinear optical processes. The crystalline structures of the TMDC with odd number of layers belong to the D_{3h} space group showing the three-fold rotational symmetry and quadratically nonlinear susceptibility tensor with a single nonzero element [10, 67, 68]:

$$\chi^{(2)} \equiv \chi^{(2)}_{xxx} = -\chi^{(2)}_{xyy} = -\chi^{(2)}_{yyx} = -\chi^{(2)}_{yxy}, \tag{3.1}$$

where x is the armchair direction and y is the zigzag direction (see the inset in Fig. 3.1 (b) 'Top view'). It is experimentally reported that the TMDC monolayer has the maximum strength of SHG at normal incidence [68]; therefore, the design in this work will focus only on monolayer structures.

Figure 3.1 (a) presents the configuration of the TMDC monolayer flattened on a transparent and thin substrate (aluminum oxide or silicon oxide film), illuminated by normal incident-wave propagating along the $-z$ direction. If the wave has a linear polarization vector $\hat{e}_\omega$, then the generated second-harmonic wave $\mathbf{E}(2\omega)$ polarized at a given direction $\hat{e}_{2\omega}$ can be expressed as:

$$\mathbf{E}(2\omega) \cdot \hat{e}_{2\omega} = C\hat{e}_{2\omega} \cdot \chi^{(2)} : \hat{e}_\omega \hat{e}_\omega, \tag{3.2}$$

where ω is the fundamental frequency, 2ω is the second-harmonic frequency, and C is a certain constant related to the local-field factors determined by the local medium. The $\hat{e}_\omega$ can be decomposed to $E_{x,\omega} = \cos(\phi)$ and $E_{y,\omega} = \sin(\phi)$,

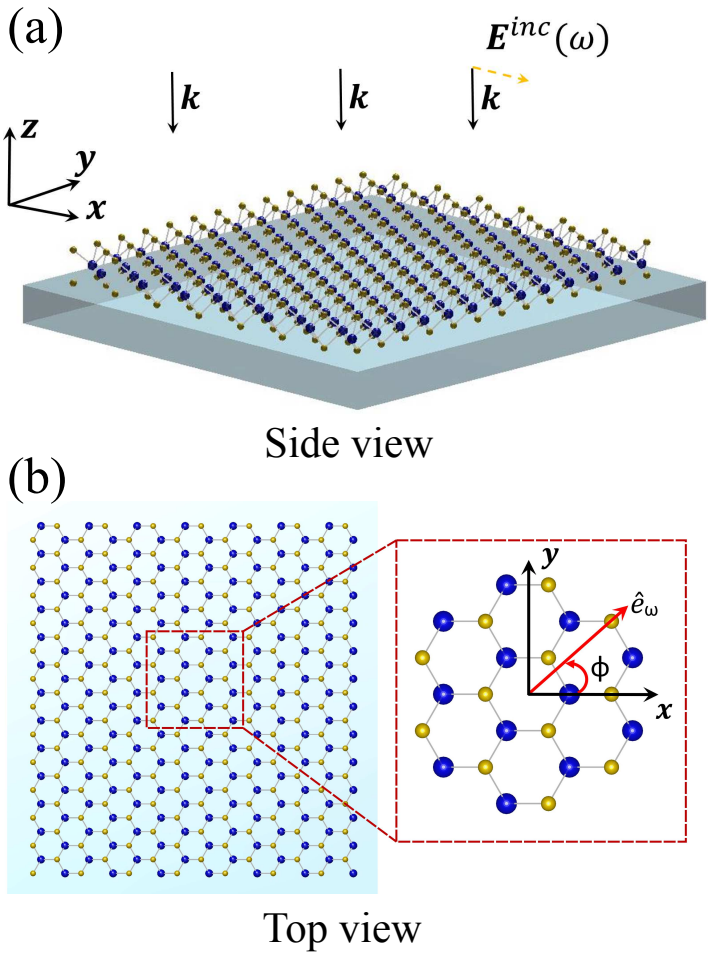

Figure 3.1: (a) Side view of the TMDC monolayer at the xoy plane. The incident plane wave propagates along the $-z$ direction. (b) Top view. The polarization angle with respect to the armchair direction (i.e. x axis) is denoted as ϕ.

where ϕ is the angle between the incident wave polarization and the x axis (the armchair direction is aligned with the x axis). According to Eq. (3.1) and Eq. (3.2), the components along x and y can be expressed as:

$$\begin{aligned} E_{x,2\omega} &= C\chi^{(2)}_{xxx}\cos(\phi)\cos(\phi) + C\chi^{(2)}_{xyy}\sin(\phi)\sin(\phi) \\ &= C\chi^{(2)}[\cos^2(\phi) - \sin^2(\phi)] \end{aligned} \tag{3.3}$$

and

$$\begin{aligned} E_{y,2\omega} &= C\chi^{(2)}_{yyx}\sin(\phi)\cos(\phi) + C\chi^{(2)}_{yxy}\cos(\phi)\sin(\phi) \\ &= -2C\chi^{(2)}\sin(\phi)\cos(\phi). \end{aligned} \tag{3.4}$$

If we choose the analyzer ($\hat{e}_{2\omega}$) pointing to the fundamental polarization vector, then the component parallel to the analyzer at second-harmonic frequency is:

$$\begin{aligned} E_{\parallel}(2\omega) &= E_{x,2\omega}\cos(\phi) + E_{y,2\omega}\sin(\phi) \\ &= C\chi^{(2)}[\cos^3(\phi) - \sin^2(\phi)\cos(\phi) - 2\sin(\phi)\cos(\phi)\sin(\phi)] \\ &= C\chi^{(2)}\cos(3\phi). \end{aligned} \tag{3.5}$$

The number 3 is a critical characterizer for the anisotropic nonlinear susceptibility with the three-fold rotational symmetry. In the same fashion, the perpendicular component can be derived as:

$$\begin{aligned} E_{\perp}(2\omega) &= -E_{x,2\omega}\sin(\phi) + E_{y,2\omega}\cos(\phi) \\ &= C\chi^{(2)}[-\cos^2(\phi)\sin(\phi) + \sin^3(\phi) - 2\sin(\phi)\cos(\phi)\cos(\phi)] \\ &= -C\chi^{(2)}\sin(3\phi). \end{aligned} \tag{3.6}$$

Note that, in all discussions, the right-hand rule is applied. The above perpendicular component satisfies $\hat{E}_{\parallel} \times \hat{E}_{\perp} = \hat{z}$.

3.2.2 Electric field integral equation for TMDC monolayers

We use the electric field integral equation (EFIE) with the impedance boundary condition to calculate the surface current on the TMDC monolayer at the fundamental frequency [5, 7]. In our theoretical model, it is reasonable to ignore substrate effects because its relative permittivity is small enough that it does not affect the polarization of the induced surface current at the fundamental frequency, and the nonlinear response from the substrate is sufficiently weak compared to the TMDC monolayer in visible regime [69] (e.g., h-BN, which is usually used as the substrate in experiments). The integral equation can be expressed as:

$$\mathcal{L}_{\omega}(\mathbf{r}, \mathbf{r}') \cdot \mathbf{J}_{s,\omega}(\mathbf{r}') - \frac{1}{\sigma_s}\{\mathbf{J}_{s,\omega}(\mathbf{r})\} = -\mathbf{E}^{inc}(\mathbf{r}), \tag{3.7}$$

where integration is implied over repeated variables. Here $\mathbf{J}_{s,\omega}$ is the surface electric current, σ_s is the surface conductivity at the fundamental frequency and $\mathbf{E}^{inc}$ is the incident electric field. More explicitly, the operator $\mathcal{L}$ repre-

sents

$$\mathcal{L}_\omega(\mathbf{r},\mathbf{r}') = i\omega\mu \int_S \big(\bar{\mathbf{I}} + \frac{\nabla\nabla}{k^2}\big)\frac{e^{ik|\mathbf{r}-\mathbf{r}'|}}{4\pi|\mathbf{r}-\mathbf{r}'|}, \tag{3.8}$$

where $\bar{\mathbf{I}}$ is identity matrix, μ is the permeability of air, k is the wavenumber in air at the fundamental frequency, and S is the surface of the monolayer.

After a geometrical discretization of the TMDC flake with triangular patches, the surface current can be expanded with Rao-Wilton-Glisson (RWG) basis functions (two adjacent triangles straddled as one edge basis function). Let $\{\mathbf{\Lambda}_n(\mathbf{r})\}$ be a RWG basis function, so that the surface current $\mathbf{J}_{s,\omega}(\mathbf{r})$ can be written as $\mathbf{J}_{s,\omega}(\mathbf{r}) = \sum_n J_{\omega,n}\mathbf{\Lambda}_n(\mathbf{r})$ for N coefficients $\{J_{\omega,n}\}$. Testing the integral equation with the same basis functions (Galerkin's method), Eq. (3.7) can be converted into a representation of matrix-vector product:

$$\left[\overline{\mathbf{L}}_\omega - \frac{1}{\sigma_s}\overline{\mathbf{G}}\right]\cdot\mathbf{J}_\omega = \mathbf{g}, \tag{3.9}$$

where

$$[\overline{\mathbf{L}}_\omega]_{mn} = \langle\Lambda_m(\mathbf{r}), \mathcal{L}_\omega(\mathbf{r},\mathbf{r}')\Lambda_n(\mathbf{r}')\rangle, \tag{3.10}$$

$$[\overline{\mathbf{G}}]_{mn} = \langle\Lambda_m(\mathbf{r}), \Lambda_n(\mathbf{r}')\rangle, \tag{3.11}$$

$$[\mathbf{J}_\omega]_n = J_{\omega,n}, \quad [\mathbf{g}]_n = \langle\Lambda_m(\mathbf{r}), -\mathbf{E}^{inc}(\mathbf{r})\rangle. \tag{3.12}$$

Here, $\langle\cdot,\cdot\rangle$ denotes the unconjugated inner product $\langle f,g\rangle = \int f(\mathbf{r})g(\mathbf{r})d\mathbf{r}$, and $\overline{\mathbf{G}}$ is also called Gram matrix for RWG basis.

For the convenience of numerical computation, the E-field at fundamental frequency $\mathbf{E}(\omega)$ is calculated at the center of each triangular patch. Once the current coefficients on RWG edges are obtained, the E-field at fundamental frequency $\mathbf{E}(\omega)$ on each triangular patch can be calculated. Then the surface current at the second-harmonic frequency is calculated by:

$$\mathbf{J}_{s,2\omega}\cdot\hat{e}_{2\omega} = \hat{e}_{2\omega}\cdot\sigma_s^{(2)} : \mathbf{E}(\omega)\mathbf{E}(\omega). \tag{3.13}$$

The $\sigma_s^{(2)}$ is the component of second-harmonic surface conductivity tensor:

$$\sigma_s^{(2)} = -i\epsilon_0(2\omega)\chi^{(2)}, \tag{3.14}$$

where $\chi^{(2)}$ is the second-harmonic susceptibility in Eq. (3.1). The scattered electric field at second harmonics is calculated by:

$$\mathbf{E}^{sca}(2\omega) = \mathcal{L}_{2\omega}\{\mathbf{J}_{s,2\omega}\}. \tag{3.15}$$

Note that $\mathbf{J}_{s,2\omega}$ is discretized on each triangular patch numerically, while the $\mathcal{L}_{2\omega}$ is established on edge basis of RWG. Therefore, the Gram matrix $\overline{\mathbf{G}}$ in (3.11) is applied to convert the $\mathbf{J}_{s,2\omega}$ to edge basis expansion before the calculation of Eq. (3.15).

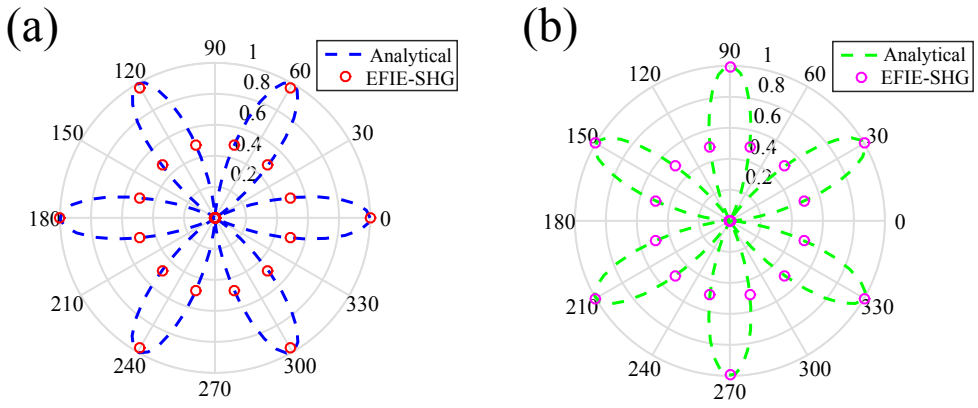

Figure 3.2: (a) Polar plot for the second-harmonic intensity of the parallel component. (b) Polar plot for the second-harmonic intensity of the perpendicular component. The "EFIE-SHG" results (second-harmonic generation by electric field integral equation) agree well with the "Analytical" solutions: $I_{\parallel,2\omega} \propto \cos^2(3\phi)$ and $I_{\perp,2\omega} \propto \sin^2(3\phi)$. The three-fold rotation symmetrical crystalline structure generates a characteristic six-fold polar pattern for the second-harmonic intensities.

The surface conductivity and the second-order surface susceptibility $\chi^{(2)}$ of the TMDC monolayer can be found in [10], where WS_2 material is adopted in our calculation. The dimension of the TMDC monolayer is 2 μm $\times$ 2 μm under the plane wave illumination with the wavelength of 800 nm. Then we apply Eq. (3.2) to obtain the E-field at the second-harmonic frequency. By rotating the monolayer and keeping the incident wave polarized along the x direction, the far-field second-harmonic intensities as a function of ϕ are calculated for both parallel component and perpendicular component

(here we choose the analyzer $\hat{e}_{2\omega}$ to be the same as $\hat{e}_{\omega}$, i.e., the x direction). Equations (3.5) and (3.6) result in the intensities of parallel part $I_{\parallel,2\omega} \propto \cos^2(3\phi)$ and the perpendicular part $I_{\perp,2\omega} \propto \sin^2(3\phi)$. Figures 3.2 (a) and (b) show the results calculated by the EFIE solver, which are consistent with the analytical expressions, and the experimental data as well [67], validating the accuracy of the model.

3.3 Metasurfaces for Structured Light Generation at Second Harmonics

In this section, the design procedure for the metasurfraces platform is discussed for the generation of radial polarization, azimuthal polarization and orbital angular momentum.

3.3.1 Generation of radially and azimuthally polarized beams

Figure 3.3 sets the global coordinate system as (x, y) and the local coordinate system of the TMDC flake as (x', y'), where x' is the armchair direction. The center of the square flake is placed at the position where the polar angle is α, and the polarization angle between x' and x is ϕ.

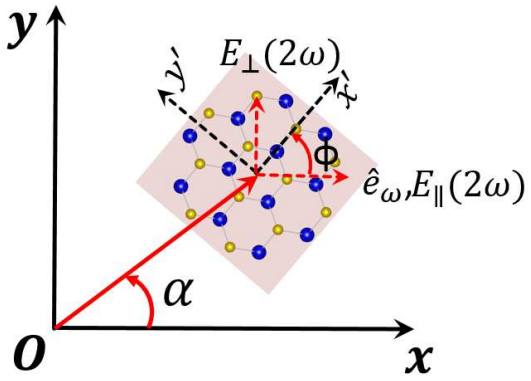

Figure 3.3: Rotated single TMDC flake with the local coordinates of (x', y'), where x' is the armchair direction. The incident plane wave has a fixed polarization along the x axis.

Assuming $E_{x,\omega}$ and $E_{y,\omega}$ are the two components of the incident wave at the fundamental frequency, then the $E_{x',\omega} = E_{x,\omega}\cos(\phi) + E_{y,\omega}\sin(\phi)$ and

$E_{y',\omega} = -E_{x,\omega}\sin(\phi) + E_{y,\omega}\cos(\phi)$. According to Eq. (3.1) and Eq. (3.2), $E_{x',2\omega}$ and $E_{y',2\omega}$ can be expressed as:

$$\begin{aligned} E_{x',2\omega} &= C\chi^{(2)}\big\{[\cos^2(\phi) - \sin^2(\phi)]E_{x,\omega}E_{x,\omega} + \\ &\quad 4\sin(\phi)\cos(\phi)E_{x,\omega}E_{y,\omega} + [\sin^2(\phi) - \cos^2(\phi)]E_{y,\omega}E_{y,\omega}\big\} \end{aligned} \tag{3.16}$$

and

$$\begin{aligned} E_{y',2\omega} &= C\chi^2\big\{2\sin(\phi)\cos(\phi)E_{x,\omega}E_{x,\omega} + \\ &\quad 2[\sin^2(\phi) - \cos^2(\phi)]E_{x,\omega}E_{y,\omega} - 2\sin(\phi)\cos(\phi)E_{y,\omega}E_{y,\omega}\big\}. \end{aligned} \tag{3.17}$$

By vector decomposition, the $E_{x,2\omega}$ and $E_{y,2\omega}$ in the global system can be derived as:

$$\begin{aligned} E_{x,2\omega} &= E_{x',2\omega}\cos(\phi) - E_{y',2\omega}\sin(\phi) \\ &= C\chi^2[\cos(3\phi)E_{x,\omega}E_{x,\omega} + 2\sin(3\phi)E_{x,\omega}E_{y,\omega} \\ &\qquad - \cos(3\phi)E_{y,\omega}E_{y,\omega}] \end{aligned} \tag{3.18}$$

and

$$\begin{aligned} E_{y,2\omega} &= E_{x',2\omega}\sin(\phi) + E_{y',2\omega}\cos(\phi) \\ &= C\chi^2[\sin(3\phi)E_{x,\omega}E_{x,\omega} - 2\cos(3\phi)E_{x,\omega}E_{y,\omega} \\ &\qquad - \sin(3\phi)E_{y,\omega}E_{y,\omega}]. \end{aligned} \tag{3.19}$$

Therefore, the nonlinear conversion between the second-harmonic electric field (E-field) and the incident fundamental E-field can be linked by a Jones matrix, i.e.:

$$\begin{bmatrix} E_{x,2\omega} \\ E_{y,2\omega} \end{bmatrix} = C\chi^{(2)} \cdot \overline{\mathbf{R}} \cdot \begin{bmatrix} E_{x,\omega}E_{x,\omega} \\ E_{x,\omega}E_{y,\omega} \\ E_{y,\omega}E_{y,\omega} \end{bmatrix}, \tag{3.20}$$

with

$$\overline{\mathbf{R}} = \begin{bmatrix} \cos(3\phi) & 2\sin(3\phi) & -\cos(3\phi) \\ \sin(3\phi) & -2\cos(3\phi) & -\sin(3\phi) \end{bmatrix}, \tag{3.21}$$

where 3ϕ is a geometric phase-like or Pancharatnam-Berry phase-like factor [70, 71] due to the anisotropic nonlinearity of the TMDC material showing three-fold rotational symmetry for its crystalline structure. Assuming the incident wave is polarized along the x direction, i.e. $E_{y,\omega} = 0$, and letting $E_{x,\omega} = 1$, then the parallel component of the second-harmonic generation (SHG) is $E_{\parallel}(2\omega) = E_{x,2\omega} = \cos(3\phi)$, and the perpendicular component is $E_{\perp}(2\omega) = E_{y,2\omega} = \sin(3\phi)$. Therefore, the resultant polarization will be pointed at the radial direction in the global system if:

$$\tan(\alpha) = \frac{E_{y,2\omega}}{E_{x,2\omega}} = \tan(3\phi). \tag{3.22}$$

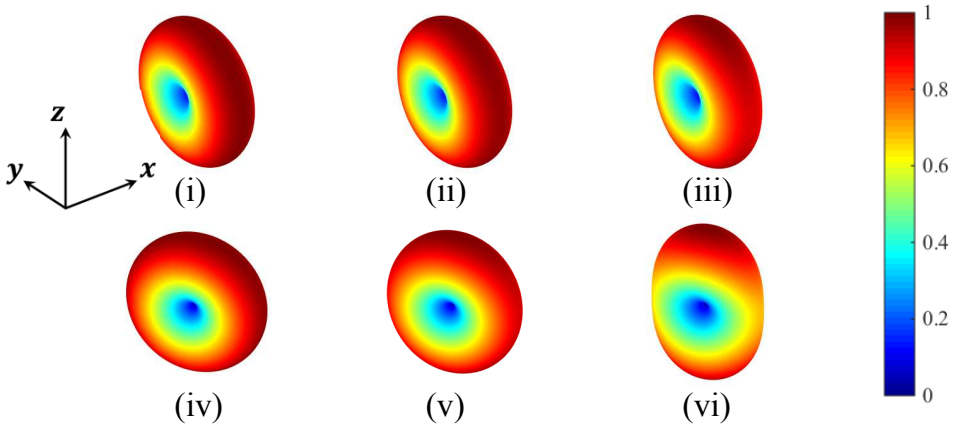

Figure 3.4: Normalized radiation pattern of a single TMDC flake rotated 10° to achieve polarization pointing to the direction of 30° at second harmonics. The incident fundamental pump is an x polarized plane wave propagating along the $-z$ direction. (i)-(iii) correspond to the side lengths of 35 nm (0.044λ), 70 nm (0.088λ), 140 nm (0.175λ) at the fundamental frequency with wavelength λ of 800 nm; (iv)-(vi) correspond to the side lengths of 35, 70, 140 nm at second-harmonic frequency. Color bar indicates the intensity of the normalized radiation pattern.

Figure 3.4 shows the normalized radiation pattern of a single TMDC flake rotated 10° to achieve the polarization pointing to 30° at second-harmonic

frequency for three side lengths of the flake, under the normal incident plane wave polarized along the x axis at the fundamental frequency. It can be found that in the sub-wavelength regime, the flake can be regarded as a dipole both at the fundamental frequency and the second-harmonic frequency, with polarization pointing to x axis and 30°, respectively. Increasing the size of the flake will be advantageous since it will increase the intensity of generated fields. However, if the dimension of the flake is too large, the radiation pattern at second harmonics will no longer be a dipole [Fig. 3.4 (vi)]. In the following discussion, the side length of the flake as a meta-atom is set as 35 nm to demonstrate the design approach.

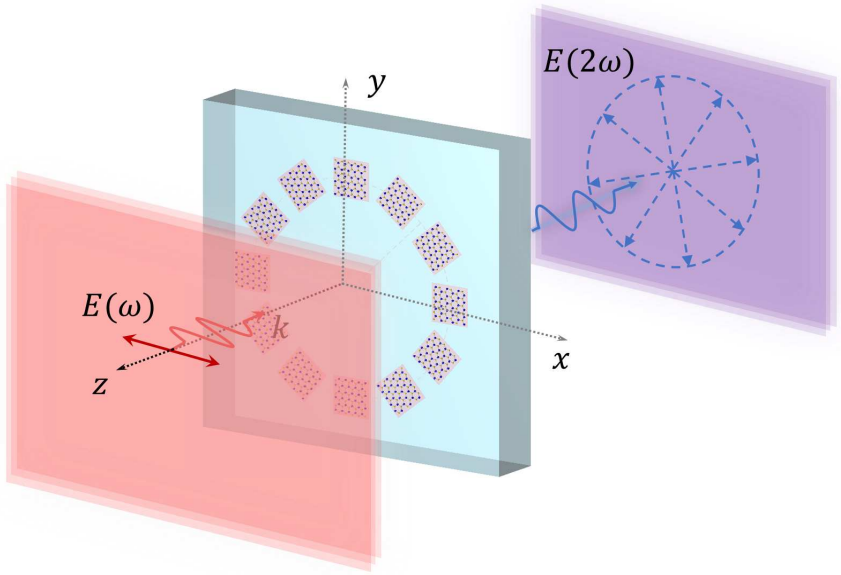

Figure 3.5: Schematic illustration of a TMDC metasurface for generating the radially polarized beam.

In order to achieve the radial polarization, which is cylindrically symmetric, each square flake is centered on a circle's circumference. Figure 3.5 illustrates a schematic pattern of the proposed metasurface for generating the radially polarized beams. The wavelength of incident E-field is 800 nm and the radius R of the circle is 100 nm. The meta-atoms are placed at the cylindrical coordinates of $(R,\ 2\pi n/N)$, where $n = 0, 1, ..., N-1$ and $N = 12$. The corresponding angles of rotation for each flake should be $2\pi n/(3N)$ by Eq. (3.22). However, this orientation configuration results in an asymmetric

metasurface structure on the whole and thus lowers the performance of the radially polarized beam generated (see Fig. 3.6).

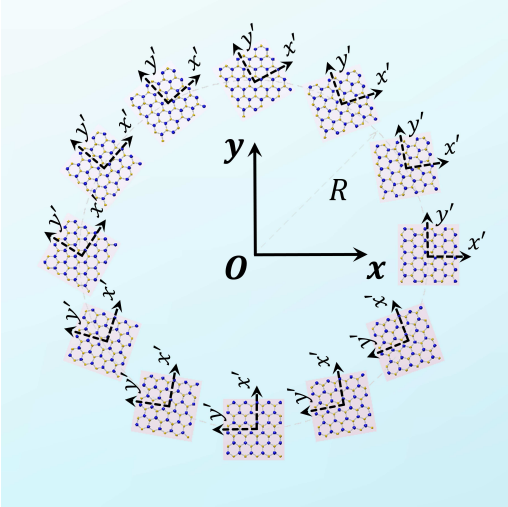

Figure 3.6: Schematic illustration of the metasurface with original rotating angles.

Exploring the three-fold rotational symmetry of the nonlinear response, for instance, instead of rotating 10° centered at (R, 30°), the flake is rotated by 130°. The 120° incremental rotation does not change the polarization state of SHG. Similarly, for those flakes that break the symmetry, the rotating angle is added by $2\pi/3$ or $4\pi/3$ (see Fig. 3.7). Figure 3.8 shows the transverse

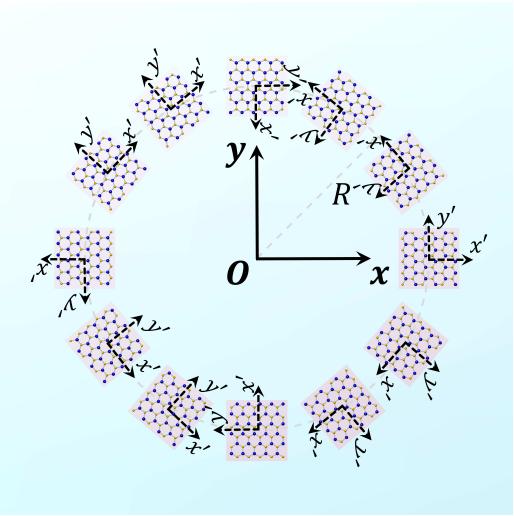

Figure 3.7: Schematic illustration of metasurface with modified rotating angles.

E-field distribution at the plane of $z = -400$ nm with x and y ranging from

-0.8 μm to 0.8 μm. A radially polarized beam with a polarization singularity can be clearly seen at the second-harmonic frequency.

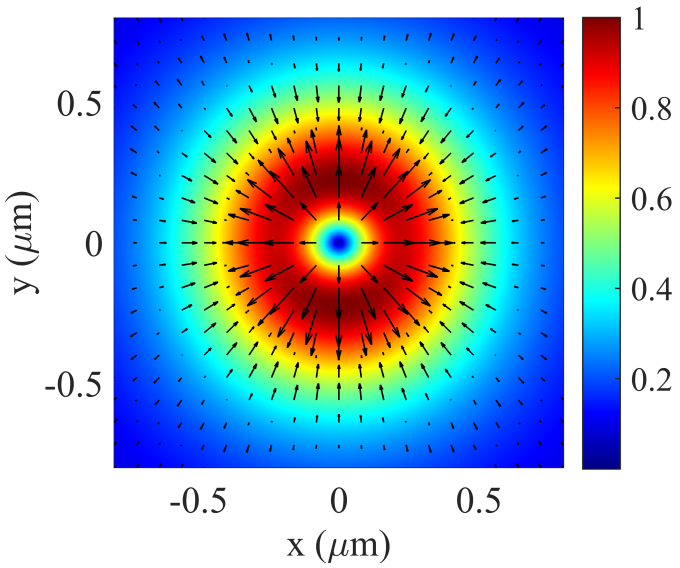

Figure 3.8: Second-harmonic E-field of the radially polarized beam at the plane of $z = -400$ nm. Color bar and arrows indicate the normalized intensity and the direction of polarization for electric field on the plane, respectively.

Figure 3.9 shows the azimuthally polarized beam generated at second harmonics through rotating each flake by $(2\pi n/N + \pi/2)/3$. In the same fashion, the rotating angle is adjusted by adding $2\pi/3$ or $4\pi/3$ when needed. One can see the vortex-like polarization structure with a singularity at the beam center (the E-field is plotted on the plane of $z = -200$ nm with x and y ranging from -1.0 μm to 1.0 μm).

The polar angle α, rotating angle ϕ and modified rotating angle ϕ' for radial polarization and azimuthal polarization are given in Tables 3.1 and 3.2, respectively.

Table 3.1: Rotating angles for radial polarization

α	0°	30°	60°	90°	120°	150°	180°	210°	240°	270°	300°	330°
ϕ	0°	10°	20°	30°	40°	50°	60°	70°	80°	90°	100°	110°
ϕ'	0°	130°	140°	270°	40°	50°	180°	310°	320°	90°	220°	230°

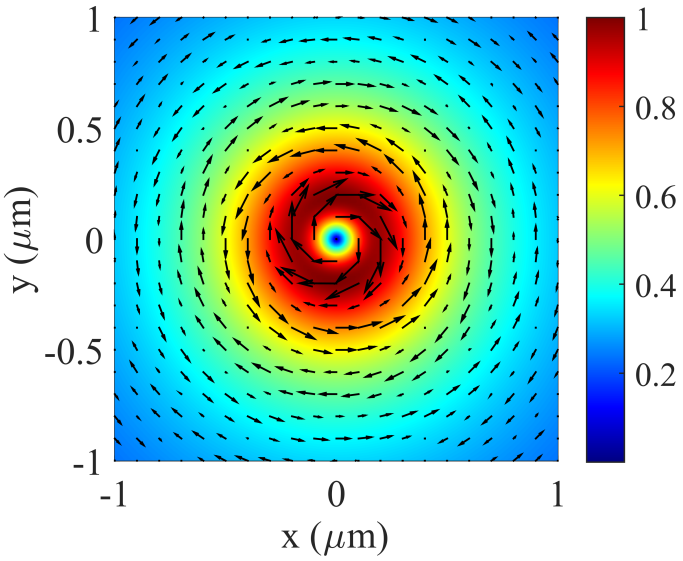

Figure 3.9: Second-harmonic E-field of the azimuthally polarized beam at the plane of $z = -200$ nm. Color bar and arrows indicate the normalized intensity and the direction of polarization for electric field on the plane, respectively.

Table 3.2: Rotating angles for azimuthal polarization

α	0°	30°	60°	90°	120°	150°	180°	210°	240°	270°	300°	330°
ϕ	30°	40°	50°	60°	70°	80°	90°	100°	110°	120°	130°	140°
ϕ'	150°	40°	50°	180°	310°	320°	90°	220°	230°	0°	130°	140°

3.3.2 Generation of orbital angular momentum

In this section, we provide the derivation in generation of orbital angular momentum (OAM) when the vertically incident plane wave with the left-circular polarization (LCP) illuminates the flake, shown in Fig. 3.10. The LCP plane wave is normalized as:

$$|\mathbf{L}\rangle = \frac{1}{\sqrt{2}}\begin{pmatrix}1\\ i\end{pmatrix}. \tag{3.23}$$

With the LCP illumination, the electric field along the x' and y' at the fundamental frequency can be expressed as:

$$E_{x',\omega} = \frac{1}{\sqrt{2}}[\cos(\phi) + i\sin(\phi)] = \frac{1}{\sqrt{2}}e^{i\phi} \tag{3.24}$$

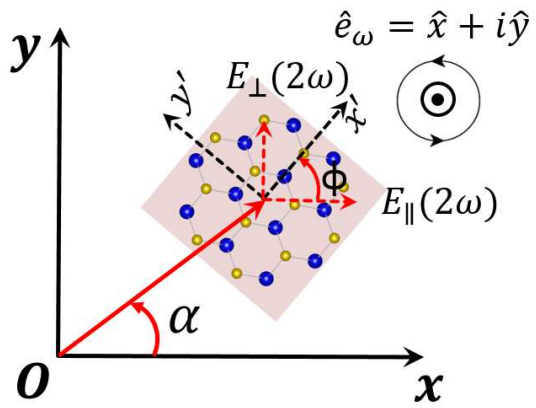

Figure 3.10: Rotated single TMDC flake with the local coordinates of (x', y'), where x' is the armchair direction. The incident plane wave is left-circularly polarized.

and

$$E_{y',\omega} = \frac{1}{\sqrt{2}}[-\sin(\phi) + i\cos(\phi)] = \frac{i}{\sqrt{2}}e^{i\phi}. \tag{3.25}$$

Then the second-harmonic components along the x' and y' are obtained by Eq. (3.1) and Eq. (3.2) (here the parameters $C\chi^{(2)}$ are omitted):

$$E_{x',2\omega} = \frac{1}{2}e^{i2\phi} - \frac{-1}{2}e^{i2\phi} = e^{i2\phi} \tag{3.26}$$

and

$$E_{y',2\omega} = -\frac{i}{2}e^{i2\phi} + \frac{-i}{2}e^{i2\phi} = -ie^{i2\phi}. \tag{3.27}$$

Back to the global system, the $E_{x,2\omega}$ and $E_{y,2\omega}$ have the following expressions:

$$\begin{aligned} E_{x,2\omega} &= E_{x',2\omega}\cos(\phi) - E_{y',2\omega}\sin(\phi) \\ &= e^{i2\phi}\cos(\phi) + ie^{i2\phi}\sin(\phi) = e^{i3\phi} \end{aligned} \tag{3.28}$$

and

$$\begin{aligned} E_{y,2\omega} &= E_{x',2\omega}\sin(\phi) + E_{y',2\omega}\cos(\phi) \\ &= e^{i2\phi}\sin(\phi) - ie^{i2\phi}\cos(\phi) = -ie^{i3\phi}. \end{aligned} \tag{3.29}$$

The radial component E_ρ is chosen to demonstrate the generation of orbital angular momentum since $e^{il\alpha}$ is the set of eigenstates for the Helmholtz equation in the cylindrical coordinates. For a flake centered with polar angle α,

$E_{\rho,2\omega}$ is expressed as:

$$\begin{aligned} E_{\rho,2\omega} &= E_{x,2\omega}\cos(\alpha) + E_{y,2\omega}\sin(\alpha) \\ &= e^{i3\phi}\cos(\alpha) - ie^{i3\phi}\sin(\alpha) = e^{i3\phi - i\alpha}. \end{aligned} \tag{3.30}$$

By choosing proper ϕ, the expression to generate OAM can be established as:

$$E_{\rho,2\omega} = C\chi^{(2)}e^{i3\phi - i\alpha} = C\chi^{(2)}e^{il\alpha}, \tag{3.31}$$

where l is the topological charge of the OAM beam to be generated. The nonlinear spin-orbital interaction can be seen from the supposition of the geometric phase factors, originating from the relation between the circular polarization and rotations of two coordinate frames of (x', y') and (x, y), which are equivalent to the translations and orientations of the anisotropically nonlinear meta-atoms. We choose to focus on E_ρ is because $\{e^{il\alpha}\}$ is the set of eigenstates for the Helmholtz equation in the cylindrical coordinates.

From Eq. (3.31), the rotating angle of each flake is $\phi = (l+1)\alpha/3$, where $\alpha = 2\pi n/N$, $n = 0, 1, ...N-1$ and $N = 12$. To achieve $l = 1$ mode, $\phi = 2\alpha/3$; $l = 2$, $\phi = \alpha$; and $l = 3$, $\phi = 4\alpha/3$. The three-fold rotational symmetry is also explored here to modify the design. Figure 3.11 (a)-(c) show the phase distributions for the OAM modes of $l = 1, 2, 3$ on a plane of $z = -200$ nm (x and y ranging from -1.25 μm to 1.25 μm), with the corresponding Fourier decompositions depicted at (d)-(f), respectively. When the topological charge $l = 1, 2$, the desired vortex mode is dominant and the purity of the vortex beam is high. However, regarding the case of $l = 3$, the amplitude of $l = 1$ mode is comparable to that of the $l = 3$ mode. The emerging of $l = 1$ mode is due the mutual coupling between each flake with the rotating angle $2\pi n/9$, which is double of $\pi n/9$, the rotating angle for $l = 1$. For higher-order OAM modes with $l > 3$, the mutual coupling and the three-fold rotational symmetry of the TMDC crystals give rise to more quasi-degenerate modes.

The wavefronts of $E_{z,2\omega}$ for OAM $l = 1$ and $l = 2$ modes are plotted in Fig. 3.12 (a)-(b) and are helical. Since $l = 3$ mode includes $l = 1$, it is not shown here. For comparison, the wavefronts of $E_{z,2\omega}$ for radial polarization is given in Fig. 3.12 (c), which is similar to that of azimuthal polarization.

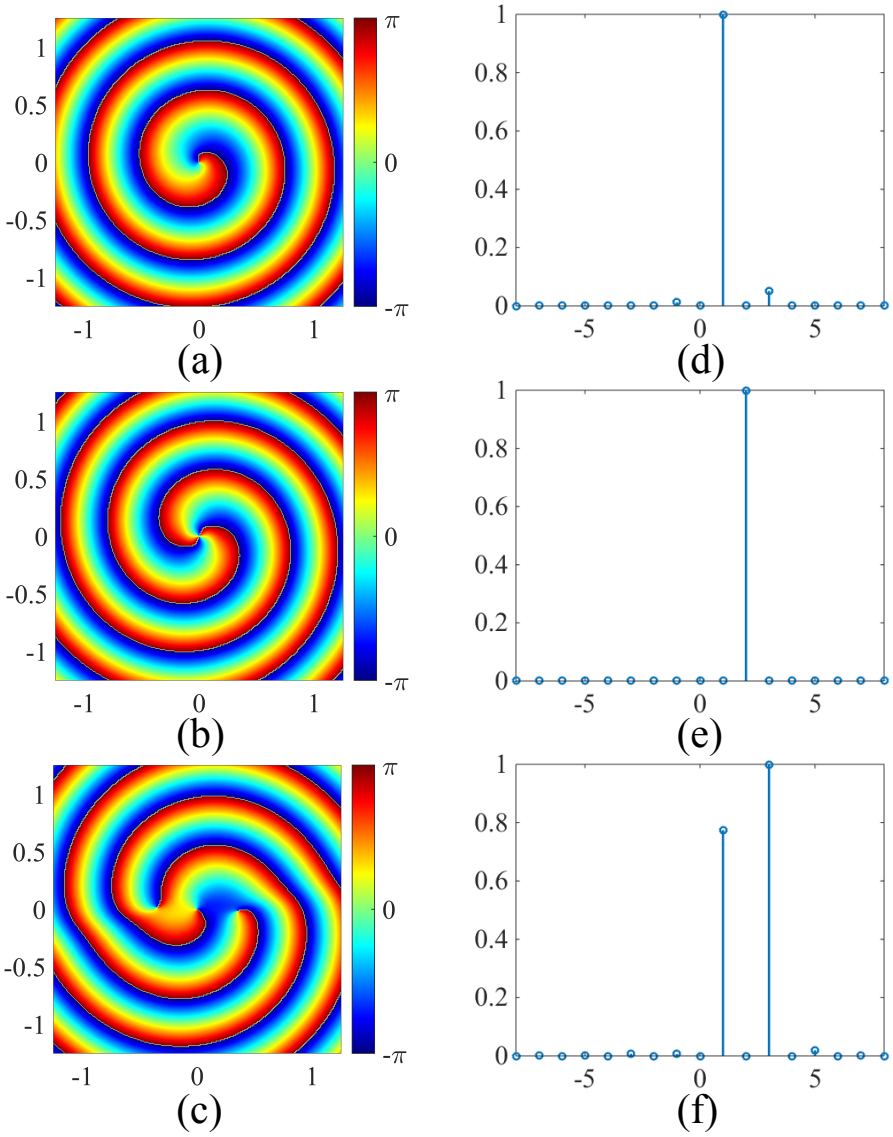

Figure 3.11: (a,b,c) Phase distributions of the second-harmonic E_ρ component for the OAM modes of (a) $l = 1$; (b) $l = 2$; (c) $l = 3$. (d,e,f) Fourier decomposition of the second-harmonic E_ρ component for the OAM modes of (d) $l = 1$; (e) $l = 2$; (f) $l = 3$.

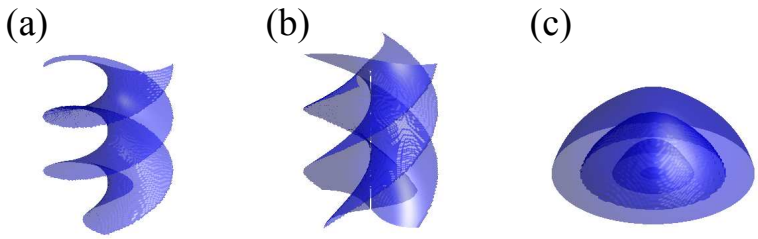

Figure 3.12: Wavefront plot. (a) OAM mode of $l = 1$; (b) OAM mode of $l = 2$; (c) Radial polarization.

3.4 Conclusion

In conclusion, the proposed TMDC metasurface converts fundamental plane waves to versatile structured light at second-harmonic frequencies. The generated structured light includes radially and azimuthally polarized beams (by linear-polarized plane waves) and vortex beams carrying different orders of OAM modes (by circular-polarized plane waves). The anisotropically nonlinear susceptibility with three-fold rotation symmetrical crystalline structure makes the TMDC meta-atoms more flexible in the control of spatial structures of light at short wavelengths, which extends the spectral bandwidth of operations in optical communication or other light manipulation. The translations and orientations of each anisotropically nonlinear meta-atom produce geometric phase at second harmonics, which can be understood as a characteristic of nonlinear spin-orbital interaction. Moreover, both the monolayer and multilayered TMDCs can be patterned on flat and curved substrates and integrated on-chip with other plasmonic and photonic nanostructures, presenting a bright outlook for the applications to next-generation optical and optoelectronic devices.

CHAPTER 4

FLUCTUATING-SURFACE-CURRENT FORMULATION OF RADIATIVE HEAT TRANSFER FOR GRAPHENE-WRAPPED OBJECTS

4.1 Introduction

Radiative heat transfer between two bodies separated by a subwavelength gap is called near-field radiation. The heat transfer rates in this regime can be enhanced beyond the constraint of the Planck law (which governs far-field heat transfer) due to the tunneling of evanescent electromagnetic waves. These enhancements have been observed in a number of recent experiments [72, 73], which can be potentially applied in areas including thermal imaging, thermal circuit elements, energy conversion and non-contact cooling. The development in experiments has sparked the theoretical studies of the radiative heat transfer in the aspects of mathematical and computational techniques. The fluctuating-surface-current formulation of radiative heat transfer based on surface integral equations (SIE) was first proposed in [74] to calculate the heat flux between objects with arbitrary shapes. Before that, the modeling was focused on the simple parallel-plate structures. A good overview of computational electromagnetics methods to study near-field heat transfer is given in [75], which covers the partial-wave scattering method, SIE and the finite-difference time domain method.

The enhancement mentioned above can be several orders of magnitude in materials that support surface electromagnetic modes. Graphene plasmonics has been proven to be an alternative platform for strong near-field radiation enhancement [76, 77, 78, 79]. Among these works, most configurations are still two parallel planar structures which have explicit expressions for the heat flux spectrum [80, 81, 82]. Or the graphene nanodisk dimers are studied by semianalytical model under electrostatic approximation [83]. The potential applications include thermal plasmonic interconnects [84], heat flux splitting [85] and ultrafast radiative cooling [86]. Graphene is a monolayer of carbon

atoms arranged in a hexagonal lattice with remarkable optical and electrical properties [87]. Several numerical methods have been proposed to study the electromagnetic phenomena of graphene-based structures [10, 88]. Compared to modeling the graphene layer as a thin volume, it is more accurate to treat it as a conducting surface. The surface integral equation (SIE) formulation has the inherent advantage of capturing the layer feature of graphene. Therefore, the fluctuating-surface-current formulation of radiative heat transfer based on SIE can be extended to the configurations of graphene-wrapped objects with arbitrary shapes. This will provide a possibility to study the heat transfer for combinations of different bulk materials with graphene layer.

This chapter is organized as follows: Section 4.2 gives the derivation of the surface integral equations (SIE) with impedance boundary condition for a graphene-wrapped object. In Section 4.3, the fluctuating-surface-current formulation of radiative heat transfer between two graphene-wrapped objects is derived. Section 4.4 concludes this formulation for different scenarios and discusses the potential applications.

4.2 Surface Integral Equations for a Graphene-wrapped Object

In this section, the surface integral equations (SIE) are established for a graphene-wrapped object. The scattering problem of a graphene-wrapped sphere is solved to validate the SIE derived.

4.2.1 Basic equations for electric and magnetic fields

The graphene coating is modeled as a conducting surface due to its atomic thickness. As illustrated in Fig. 4.1, the domain of the electromagnetic field is divided into the interior of the dielectric domain V_2, the external domain V_1 and the interface S. Surfaces S^+ and S^- are imaginary surfaces that are just large enough to contain S and small enough to be enclosed in S, respectively. The surface conductivity σ_s is introduced by graphene coating.

By invoking the Love's equivalence principle [89] for the exterior medium, the region V_2 is filled up with the same material of the region V_1. The equivalent electric and magnetic currents $(\mathbf{J}_1, \mathbf{M}_1)$ defined on the external surface

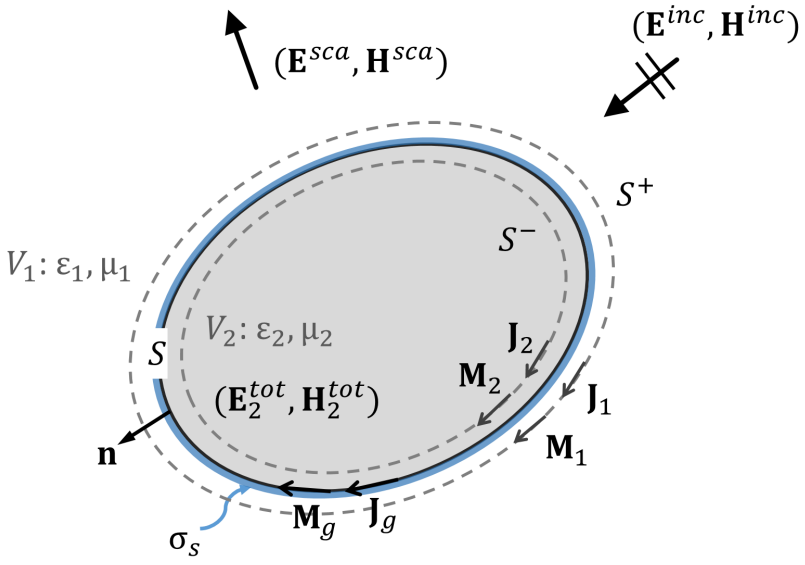

Figure 4.1: Illustration of the Love's equivalent principle for a scattering problem of a graphene-wrapped object with homogeneous dielectric material.

S^+ produce the total electromagnetic field $(\mathbf{E}_1^{tot}, \mathbf{H}_1^{tot})$ in the region V_1, and null field in the region V_2. The equivalent surface currents are the discontinuities of the fields on the boundary S^+, and according to the boundary condition they can be written as:

$$\begin{cases} \mathbf{J}_1 = \mathbf{n} \times \mathbf{H}_1^{tot} \\ \mathbf{M}_1 = -\mathbf{n} \times \mathbf{E}_1^{tot} \end{cases}, \tag{4.1}$$

where $\mathbf{n}$ is the outer normal of the surface. Similarly, by invoking the Love's equivalence principle for the interior medium, the region V_1 is filled up with the same material of the region V_2. The equivalent surface currents $(\mathbf{J}_2, \mathbf{M}_2)$ positioned on the interior surface S^- generate the total electromagnetic field $(\mathbf{E}_2^{tot}, \mathbf{H}_2^{tot})$ in the region V_2 and null field in the region V_1. According to the boundary condition, they can be defined as:

$$\begin{cases} \mathbf{J}_2 = -\mathbf{n} \times \mathbf{H}_2^{tot} \\ \mathbf{M}_2 = \mathbf{n} \times \mathbf{E}_2^{tot} \end{cases}. \tag{4.2}$$

Consequently, the surface integral equations for electric field become:

$$\left.\begin{array}{ll} \mathbf{r} \in V_\ell, & \mathbf{E}_\ell^{tot}(\mathbf{r}) \\ \mathbf{r} \notin V_\ell, & 0 \end{array}\right\} = \mathbf{E}_\ell^i(\mathbf{r}) \quad + \quad i\omega\mu \int_{S^+} dS' \overline{\mathbf{G}}(\mathbf{r}, \mathbf{r}') \cdot \mathbf{J}_\ell(\mathbf{r}') \\ - \quad \nabla \times \int_{S^+} dS' \overline{\mathbf{G}}(\mathbf{r}, \mathbf{r}') \cdot \mathbf{M}_\ell(\mathbf{r}'), \quad (4.3)$$

where the subscript $\ell = 1, 2$ denotes the exterior or interior region, and $\mathbf{E}_\ell^i$ represents the source field in region V_ℓ. For scattering problems, $\mathbf{E}_\ell^i$ is the incident electric field, i.e. $\mathbf{E}^{inc}$, and $\mathbf{E}_2^i = 0$. In this section, only scattering problems are discussed.

Using operator notations, Eq. (4.3) can be expressed more compactly as:

$$\left.\begin{array}{ll} \mathbf{r} \in V_\ell, & \mathbf{E}_\ell^{tot}(\mathbf{r}) \\ \mathbf{r} \notin V_\ell, & 0 \end{array}\right\} = \mathbf{E}_\ell^i(\mathbf{r}) + \mathcal{L}_{\ell E}(\mathbf{r}, \mathbf{r}') \cdot \mathbf{J}_\ell(\mathbf{r}') + \mathcal{K}_{\ell E}(\mathbf{r}, \mathbf{r}') \cdot \mathbf{M}_\ell(\mathbf{r}'), \quad (4.4)$$

where integral over repeated variables is implied. More explicitly, the operators are:

$$\mathcal{L}_{\ell E}(\mathbf{r}, \mathbf{r}') = i\omega\mu_\ell \overline{\mathbf{G}}(\mathbf{r}, \mathbf{r}') = i\omega\mu_\ell \left(\overline{\mathbf{I}} + \frac{\nabla\nabla}{k_\ell^2} \right) g_\ell(\mathbf{r}, \mathbf{r}') \quad (4.5)$$

$$\mathcal{K}_{\ell E}(\mathbf{r}, \mathbf{r}') = -\nabla \times \overline{\mathbf{G}}(\mathbf{r}, \mathbf{r}') = -\nabla g_\ell(\mathbf{r}, \mathbf{r}') \times \overline{\mathbf{I}}, \quad (4.6)$$

where

$$g_\ell(\mathbf{r}, \mathbf{r}') = \frac{e^{ik_\ell|\mathbf{r}-\mathbf{r}'|}}{4\pi|\mathbf{r}-\mathbf{r}'|}, \quad \ell = 1, 2. \quad (4.7)$$

The subscripts E of the above operators indicate that they are generating electric field from either electric current or the magnetic current respectively.

Similarly, the integral equations for magnetic field can be written as:

$$\left.\begin{array}{ll} \mathbf{r} \in V_\ell, & \mathbf{H}_\ell^{tot}(\mathbf{r}) \\ \mathbf{r} \notin V_\ell, & 0 \end{array}\right\} = \mathbf{H}_\ell^i(\mathbf{r}) + \mathcal{L}_{\ell H}(\mathbf{r}, \mathbf{r}') \cdot \mathbf{M}_\ell(\mathbf{r}') + \mathcal{K}_{\ell H}(\mathbf{r}, \mathbf{r}') \cdot \mathbf{J}_\ell(\mathbf{r}'), \quad (4.8)$$

where the integral over repeated variables is implied. The $\mathbf{H}_\ell^i$ is the incident magnetic field , i.e. $\mathbf{H}^{inc}$, and $\mathbf{H}_2^i = 0$. The operators relevant to magnetic

field are

$$\mathcal{L}_{\ell H}(\mathbf{r},\mathbf{r}') = i\omega\epsilon_\ell \overline{\mathbf{G}}(\mathbf{r},\mathbf{r}') = \frac{1}{\eta_\ell^2}\mathcal{L}_{\ell E}(\mathbf{r},\mathbf{r}') \tag{4.9}$$

$$\mathcal{K}_{\ell H}(\mathbf{r},\mathbf{r}') = \nabla \times \overline{\mathbf{G}}(\mathbf{r},\mathbf{r}') = -\mathcal{K}_{\ell E}(\mathbf{r},\mathbf{r}'), \tag{4.10}$$

where $\eta_\ell = \sqrt{\mu_\ell/\epsilon_\ell}$ and $\ell = 1, 2$.

Due to the surface conductivity of graphene, denoted as σ_s, the tangential component of the electric field is continuous while the tangential component of the magnetic field is discontinuous. According to Eq. (4.1) and Eq. (4.2), the exterior and interior equivalent surface currents have the following relation:

$$\begin{cases} \mathbf{J}_1 + \mathbf{J}_2 = \mathbf{n} \times (\mathbf{H}_1^{tot} - \mathbf{H}_2^{tot}) = \mathbf{J}_\sigma \\ \mathbf{M}_1 + \mathbf{M}_2 = -\mathbf{n} \times (\mathbf{E}_1^{tot} - \mathbf{E}_2^{tot}) = 0 \end{cases}, \tag{4.11}$$

where $\mathbf{J}_\sigma = \sigma_s \mathbf{E}_{1t} = \sigma_s \mathbf{n} \times \mathbf{M}_1$ and $\mathbf{E}_{1t}$ denotes the tangential component $\mathbf{E}_1^{tot}$ on the boundary.

By applying the exterior and interior integral equations given in Eq. (4.4) and Eq. (4.8) to the boundary conditions in Eq. (4.11) for both electric field and magnetic field, a PMCHWT (Poggio-Miller-Chang-Harrington-Wu-Tsai) formulation with impedance boundary is obtained:

$$\begin{aligned} \mathbf{n} \times [&\mathcal{L}_{1E}(\mathbf{r},\mathbf{r}') \cdot \mathbf{J}_1(\mathbf{r}') + \mathcal{K}_{1E}(\mathbf{r},\mathbf{r}') \cdot \mathbf{M}_1(\mathbf{r}') - \mathcal{L}_{2E}(\mathbf{r},\mathbf{r}') \cdot \mathbf{J}_2(\mathbf{r}') \\ &-\mathcal{K}_{2E}(\mathbf{r},\mathbf{r}') \cdot \mathbf{M}_2(\mathbf{r}')] = -\mathbf{n} \times \mathbf{E}^{inc}(\mathbf{r}) \end{aligned} \tag{4.12}$$

$$\begin{aligned} \mathbf{n} \times [&\mathcal{K}_{1H}(\mathbf{r},\mathbf{r}') \cdot \mathbf{J}_1(\mathbf{r}') + \mathcal{L}_{1H}(\mathbf{r},\mathbf{r}') \cdot \mathbf{M}_1(\mathbf{r}') - \mathcal{K}_{2H}(\mathbf{r},\mathbf{r}') \cdot \mathbf{J}_2(\mathbf{r}') \\ &-\mathcal{L}_{2H}(\mathbf{r},\mathbf{r}') \cdot \mathbf{M}_2(\mathbf{r}')] - \sigma_s \mathbf{n} \times \mathbf{M}_1(\mathbf{r}) = -\mathbf{n} \times \mathbf{H}^{inc}(\mathbf{r}), \end{aligned} \tag{4.13}$$

where the incident field $\mathbf{E}^{inc}$ and $\mathbf{H}^{inc}$ have been moved to the other side.

4.2.2 Principal value integrals and system matrix representation

In last section, the surface integral equations for electric field and magnetic field have been established. In addition, the boundary condition for graphene coating (a conducting surface) indicates that $\mathbf{J}_1+\mathbf{J}_2=\mathbf{J}_\sigma$ and $\mathbf{M}_1+\mathbf{M}_2=0$. The gradient on the Green's function in operator $\mathcal{K}$ makes the integral more singular, and the principal value integral method can be used to evaluate this singular integral [5]. The operator $\mathcal{K}'$ denotes the principal value integral in the following discussion.

On surface S^+, the singular integral can be expressed as:

$$\mathbf{n}\times\mathcal{K}_{1H}(\mathbf{r},\mathbf{r}')\cdot\mathbf{J}_1(\mathbf{r}')=\mathbf{n}\times\mathcal{K}'_{1H}(\mathbf{r},\mathbf{r}')\cdot\mathbf{J}_1(\mathbf{r}')+\frac{1}{2}\mathbf{J}_1(\mathbf{r}), \tag{4.14}$$

and

$$\mathbf{n}\times\mathcal{K}_{1E}(\mathbf{r},\mathbf{r}')\cdot\mathbf{M}_1(\mathbf{r}')=\mathbf{n}\times\mathcal{K}'_{1E}(\mathbf{r},\mathbf{r}')\cdot\mathbf{M}_1(\mathbf{r}')-\frac{1}{2}\mathbf{M}_1(\mathbf{r}). \tag{4.15}$$

On surface S^-, the sign in front of the currents changes due to the integral path in the principal value integral:

$$\mathbf{n}\times\mathcal{K}_{2H}(\mathbf{r},\mathbf{r}')\cdot\mathbf{J}_2(\mathbf{r}')=\mathbf{n}\times\mathcal{K}'_{2H}(\mathbf{r},\mathbf{r}')\cdot\mathbf{J}_2(\mathbf{r}')-\frac{1}{2}\mathbf{J}_2(\mathbf{r}), \tag{4.16}$$

and

$$\mathbf{n}\times\mathcal{K}_{2E}(\mathbf{r},\mathbf{r}')\cdot\mathbf{M}_2(\mathbf{r}')=\mathbf{n}\times\mathcal{K}'_{2E}(\mathbf{r},\mathbf{r}')\cdot\mathbf{M}_2(\mathbf{r}')+\frac{1}{2}\mathbf{M}_2(\mathbf{r}). \tag{4.17}$$

Taking the principal value integral considered in Eq. (4.12), the integral equation can be rewritten as:

$$\begin{aligned}\mathbf{n}\times[&\mathcal{L}_{1E}(\mathbf{r},\mathbf{r}')\cdot\mathbf{J}_1(\mathbf{r}')+\mathcal{K}'_{1E}(\mathbf{r},\mathbf{r}')\cdot\mathbf{M}_1(\mathbf{r}')-\mathcal{L}_{2E}(\mathbf{r},\mathbf{r}')\cdot\mathbf{J}_2(\mathbf{r}')\\&-\mathcal{K}'_{2E}(\mathbf{r},\mathbf{r}')\cdot\mathbf{M}_2(\mathbf{r}')]-\frac{1}{2}[\mathbf{M}_1(\mathbf{r})+\mathbf{M}_2(\mathbf{r})]=-\mathbf{n}\times\mathbf{E}^{inc}(\mathbf{r}).\end{aligned} \tag{4.18}$$

By applying $-\mathbf{n}\times$ on both sides of Eq. (4.18), and due to the properties of

Rao-Wilton-Glisson (RWG) basis functions, it can be further simplified as:

$$\mathcal{L}_{1E}(\mathbf{r},\mathbf{r}')\cdot\mathbf{J}_1(\mathbf{r}')+[\mathcal{K}'_{1E}(\mathbf{r},\mathbf{r}')+\mathcal{K}'_{2E}(\mathbf{r},\mathbf{r}')]\cdot\mathbf{M}_1(\mathbf{r}')-\mathcal{L}_{2E}(\mathbf{r},\mathbf{r}')\cdot\mathbf{J}_2(\mathbf{r}') = \mathbf{n}\times\mathbf{n}\times\mathbf{E}^{inc}(\mathbf{r})=-\mathbf{E}_t^{inc}(\mathbf{r}), \quad (4.19)$$

where $\mathbf{E}_t^{inc}$ is the tangential component of $\mathbf{E}^{inc}$ on the boundary.

Similarly, for Eq. (4.13), after employing principal value integral it can be expressed as:

$$\mathbf{n}\times[\mathcal{K}'_{1H}(\mathbf{r},\mathbf{r}')\cdot\mathbf{J}_1(\mathbf{r}')+\mathcal{L}_{1H}(\mathbf{r},\mathbf{r}')\cdot\mathbf{M}_1(\mathbf{r}')-\mathcal{K}'_{2H}(\mathbf{r},\mathbf{r}')\cdot\mathbf{J}_2(\mathbf{r}') -\mathcal{L}_{2H}(\mathbf{r},\mathbf{r}')\cdot\mathbf{M}_2(\mathbf{r}')]+\frac{1}{2}[\mathbf{J}_1(\mathbf{r})+\mathbf{J}_2(\mathbf{r})]-\sigma_s\mathbf{n}\times\mathbf{M}_1(\mathbf{r}) = -\mathbf{n}\times\mathbf{H}^{inc}(\mathbf{r}). \quad (4.20)$$

Since $\mathbf{J}_1+\mathbf{J}_2=\mathbf{J}_\sigma=\sigma_s\mathbf{n}\times\mathbf{M}_1$ and $\mathbf{M}_2=-\mathbf{M}_1$, the Eq. (4.20) can be simplified as the following equation after applying $-\mathbf{n}\times$ on its both sides:

$$\mathcal{K}'_{1H}(\mathbf{r},\mathbf{r}')\cdot\mathbf{J}_1(\mathbf{r}')+[\mathcal{L}_{1H}(\mathbf{r},\mathbf{r}')+\mathcal{L}_{2H}(\mathbf{r},\mathbf{r}')]\cdot\mathbf{M}_1(\mathbf{r}')-\frac{1}{2}\sigma_s\mathbf{M}_1(\mathbf{r}) -\mathcal{K}'_{2H}(\mathbf{r},\mathbf{r}')\cdot\mathbf{J}_2(\mathbf{r}')=\mathbf{n}\times\mathbf{n}\times\mathbf{H}^{inc}(\mathbf{r})=-\mathbf{H}_t^{inc}(\mathbf{r}), \quad (4.21)$$

where $\mathbf{H}_t^{inc}$ is the tangential component of $\mathbf{H}^{inc}$ on the boundary.

Combing Eq. (4.19), Eq. (4.21) and the relation between currents, the integral equations to be solved for the whole system can be expressed as a matrix-vector form $\mathbf{Cx}=\mathbf{b}$:

$$\mathbf{C}=\begin{pmatrix}\mathcal{L}_{1E} & \mathcal{K}'_{1E}+\mathcal{K}'_{2E} & -\mathcal{L}_{2E}\\ \mathcal{K}'_{1H} & \mathcal{L}_{1H}+\mathcal{L}_{2H}-\frac{1}{2}\sigma_s & -\mathcal{K}'_{2H}\\ \bar{\mathbf{I}} & -\sigma_s\mathbf{n}\times\bar{\mathbf{I}} & \bar{\mathbf{I}}\end{pmatrix} \quad (4.22)$$

$$\mathbf{x}=\begin{pmatrix}\mathbf{J}_1\\ \mathbf{M}_1\\ \mathbf{J}_2\end{pmatrix},\qquad \mathbf{b}=\begin{pmatrix}-\mathbf{E}_t^{inc}\\ -\mathbf{H}_t^{inc}\\ 0\end{pmatrix}, \quad (4.23)$$

where $\mathbf{x}$ is the vector of unknowns and $\mathbf{b}$ is the vector of excitation (here $(\mathbf{r},\mathbf{r}')$, $(\mathbf{r})$ and $(\mathbf{r}')$ are omitted for brevity).

In the discussion of radiative heat transfer later, the unknown currents should be reduced to the interior equivalent surface currents, i.e., $\mathbf{J}_2$ and $\mathbf{M}_2$, when the fluctuating-current sources are considered inside the object. In

addition, the signs of $\mathbf{J}_2$ and $\mathbf{M}_2$ are flipped for the convenience of derivation. Therefore the system equation becomes:

$$\mathbf{C} = \begin{pmatrix} \mathcal{L}_{2E} & \mathcal{K}'_{2E} + \mathcal{K}'_{1E} & \mathcal{L}_{1E} \\ \mathcal{K}'_{2H} & \mathcal{L}_{2H} + \mathcal{L}_{1H} - \frac{1}{2}\sigma_s & \mathcal{K}'_{1H} \\ -\overline{\mathbf{I}} & -\sigma_s \mathbf{n} \times \overline{\mathbf{I}} & \overline{\mathbf{I}} \end{pmatrix} \tag{4.24}$$

$$\mathbf{x} = \begin{pmatrix} \mathbf{J}_2 \\ \mathbf{M}_2 \\ \mathbf{J}_1 \end{pmatrix}, \qquad \mathbf{b} = \begin{pmatrix} -\mathbf{E}_t^{inc} \\ -\mathbf{H}_t^{inc} \\ 0 \end{pmatrix}, \tag{4.25}$$

where

$$\mathbf{J}_1 = \mathbf{J}_2 + \sigma_s \mathbf{n} \times \mathbf{M}_2. \tag{4.26}$$

With the aid of basis functions and the Galerkin's method, $\mathbf{J}_1$ can be represented by $\mathbf{J}_2$ and $\mathbf{M}_2$ numerically.

Assume

$$\mathbf{J}_2(\mathbf{r}) = \sum_{n=1}^{N} J_{2n} \mathbf{f}_n(\mathbf{r}), \qquad \mathbf{M}_2(\mathbf{r}) = \sum_{n=1}^{N} M_{2n} \mathbf{f}_n(\mathbf{r}), \tag{4.27}$$

where $\mathbf{f}_n(\mathbf{r})$ is a known as basis function (RWG is used in the whole discussion), while J_{2n}'s and M_{2n}'s are the unknown expansion coefficients to be sought in scattering problems. The above equations can be written compactly:

$$\mathbf{J}_2(\mathbf{r}) = \overline{\mathbf{F}}^T(\mathbf{r}) \cdot \mathbf{I}_{2J}, \qquad \mathbf{M}_2(\mathbf{r}) = \overline{\mathbf{F}}^T(\mathbf{r}) \cdot \mathbf{I}_{2M}, \tag{4.28}$$

where

$$[\overline{\mathbf{F}}(\mathbf{r})]_n = \mathbf{f}_n(\mathbf{r}), \quad [\mathbf{I}_{2J}]_n = J_{2n}, \quad [\mathbf{I}_{2M}]_n = M_{2n}. \tag{4.29}$$

The superscript T denotes the transpose of a matrix (actually $\overline{\mathbf{F}}$ is a vector here).

Similarly, $\mathbf{J}_1$ can be expressed as

$$\begin{aligned} \mathbf{J}_1(\mathbf{r}) &= \sum_{n=1}^{N} J_{1n} \mathbf{f}_n(\mathbf{r}) = \overline{\mathbf{F}}^T(\mathbf{r}) \cdot \mathbf{I}_{1J} \\ &= \sum_{n=1}^{N} J_{2n} \mathbf{f}_n(\mathbf{r}) + \sigma_s \mathbf{n} \times \sum_{n=1}^{N} M_{2n} \mathbf{f}_n(\mathbf{r}) \\ &= \overline{\mathbf{F}}^T(\mathbf{r}) \cdot \mathbf{I}_{2J} + \sigma_s \mathbf{n} \times \overline{\mathbf{F}}^T(\mathbf{r}) \cdot \mathbf{I}_{2M}. \end{aligned} \tag{4.30}$$

By testing Eq. (4.30) with the same set of functions as in Galerkin's method, a matrix-vector product form to find J_{1n} can be written as:

$$\overline{\mathbf{G}}_M \cdot \mathbf{I}_{1J} = \overline{\mathbf{G}}_M \cdot \mathbf{I}_{2J} + \sigma_s \overline{\mathbf{O}}_X \cdot \mathbf{I}_{2M}, \tag{4.31}$$

where

$$[\overline{\mathbf{G}}_M]_{mn} = \langle \mathbf{f}_m, \mathbf{f}_n \rangle \tag{4.32}$$

$$[\overline{\mathbf{O}}_X]_{mn} = \langle \mathbf{f}_m, \mathbf{n} \times \mathbf{f}_n \rangle. \tag{4.33}$$

$$\langle \mathbf{f}, \mathbf{g} \rangle = \int \mathbf{f}(\mathbf{r}) \cdot \mathbf{g}(\mathbf{r}) d\mathbf{r}. \tag{4.34}$$

The matrix $\overline{\mathbf{G}}_M$ is the Gram matrix of RWG basis functions. Therefore,

$$\mathbf{I}_{1J} = \mathbf{I}_{2J} + \sigma_s \overline{\mathbf{G}}_M^{-1} \cdot \overline{\mathbf{O}}_X \cdot \mathbf{I}_{2M}. \tag{4.35}$$

Taking Eq. (4.35) back to Eq. (4.24) and Eq. (4.25), the system matrix-vector form with testing and basis functions becomes:

$$\overline{\mathbf{C}} = \begin{pmatrix} \mathcal{L}_{2E} + \mathcal{L}_{1E} & \mathcal{K}'_{2E} + \mathcal{K}'_{1E} + \sigma_s \mathcal{L}_{1E} \cdot \overline{\mathbf{G}}_M^{-1} \cdot \overline{\mathbf{O}}_X \\ \mathcal{K}'_{2H} + \mathcal{K}'_{1H} & \mathcal{L}_{2H} + \mathcal{L}_{1H} - \frac{1}{2}\sigma_s \overline{\mathbf{G}}_M + \sigma_s \mathcal{K}'_{1H} \cdot \overline{\mathbf{G}}_M^{-1} \cdot \overline{\mathbf{O}}_X \end{pmatrix} \tag{4.36}$$

$$\overline{\mathbf{x}} = \begin{pmatrix} \mathbf{I}_{2J} \\ \mathbf{I}_{2M} \end{pmatrix}, \qquad \overline{\mathbf{b}} = \begin{pmatrix} \mathbf{V}_E \\ \mathbf{V}_H \end{pmatrix}, \tag{4.37}$$

where

$$\mathbf{V}_E = -\langle \mathbf{f}, \mathbf{E}_t^{inc} \rangle, \qquad \mathbf{V}_H = -\langle \mathbf{f}, \mathbf{H}_t^{inc} \rangle. \tag{4.38}$$

Note that in Eq. (4.36), we keep using the same notations of $\mathcal{L}$ and $\mathcal{K}'$ for brevity, which include both testing and basis functions.

4.2.3 Numerical results

In this section, the radar cross section (RCS) and scattering cross section (SCS) efficiency of a graphene-wrapped dielectric sphere are provided as benchmarks for the surface integral equations derived in the previous section.

The surface conductivity of graphene is frequency dependent, which can be derived by random-phase approximation [83], consisting of intra-band and

inter-band conductivities, expressed as:

$$\sigma_s = \sigma_{intra} + \sigma_{inter}, \tag{4.39}$$

where

$$\sigma_{intra} = \frac{i}{\omega + i/\tau} \frac{q_0^2 2k_B T}{\pi\hbar^2} \ln\left[2\cosh\frac{E_F}{2k_B T}\right] \tag{4.40}$$

$$\sigma_{inter} = \frac{q_0^2}{4\pi\hbar}\left[H\left(\frac{\hbar\omega}{2}\right) + i\frac{4\hbar\omega}{\pi}\int_0^\infty \frac{H(\xi) - H(\hbar\omega/2)}{(\hbar\omega)^2 - 4\xi^2} d\xi\right], \tag{4.41}$$

with

$$H(\xi) = \sinh\frac{\xi}{k_B T}\left[\cosh\frac{E_F}{k_B T} + \cosh\frac{\xi}{k_B T}\right]^{-1}. \tag{4.42}$$

In the above expressions, q_0, $\hbar$, k_B, E_F, τ, and T are electron charge, reduced Plank constant, Boltzmann constant, Fermi energy, electron-phonon relaxation time, and temperature, respectively.

Figure 4.2 shows the surface conductivity of graphene with $T = 300$ K, $\tau = 0.1$ ps for different Fermi energies ($E_F = 0.3, 0.35, 0.4$ eV). The imaginary part of the surface conductivity of the graphene is positive in the terahertz regime, which indicates a "metallic" type nature that can support local surface plasmons. We will show the resonant peaks in the scattering cross section efficiency.

To compare the results of RCS calculated with Mie series for a multi-layer sphere, an effective permittivity is introduced:

$$\epsilon(\omega) = \epsilon_0\left(1 + \frac{i\sigma_s}{\epsilon_0\omega h_{eff}}\right), \tag{4.43}$$

where ϵ_0 is the permittivity in vacuum and h_{eff} is the effective thickness of the graphene layer (here $h_{eff} = 0.33$ nm). Figure 4.3 shows the effective permittivity corresponding to the surface conductivity shown in Figure 4.2.

Figure 4.4 shows the RCS of a graphene-wrapped sphere with radius of 500 nm and wavelength of 5 μm. The dielectric constants of the sphere and the background are both 2.25. Obviously, the simulation from SIE has good accuracy compared to analytical solutions.

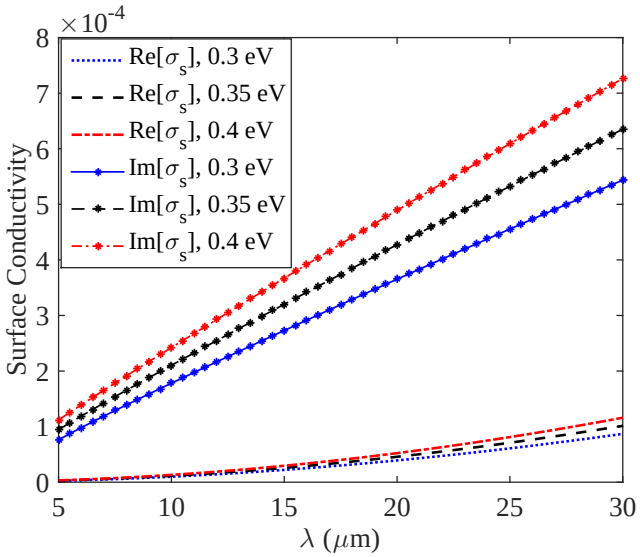

Figure 4.2: Surface conductivity of graphene at $T = 300$ K and $\tau = 0.1$ ps. The "Re[σ_s]" and "Im[σ_s]" denote the real and imaginary parts of σ_s.

The scattering cross section efficiency is also calculated for different radii of the sphere and various Fermi energies. The results in Figs. 4.5 and 4.6 are consistent with the data from [90] which are calculated by Mie series. The surface plasmon resonances are red-shifted with enhanced peaks as the radius goes large, and blue-shifted with enhanced peaks as the Fermi energy is increased.

In summary, the proposed SIE with impedance boundary condition for a graphene-wrapped dielectric object has been validated by simulations of RCS and SCS. The relation between interior and exterior equivalent surface currents will be introduced in the discussion of the radiative heat transfer when graphene is involved.

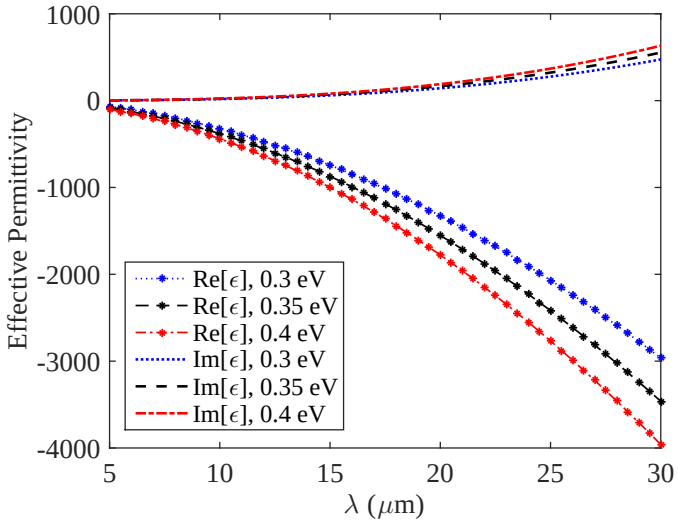

Figure 4.3: Surface conductivity of graphene with $T = 300$ K and $\tau = 0.1$ ps. The "Re[ϵ]" and "Im[ϵ]" denote the real and imaginary parts of ϵ.

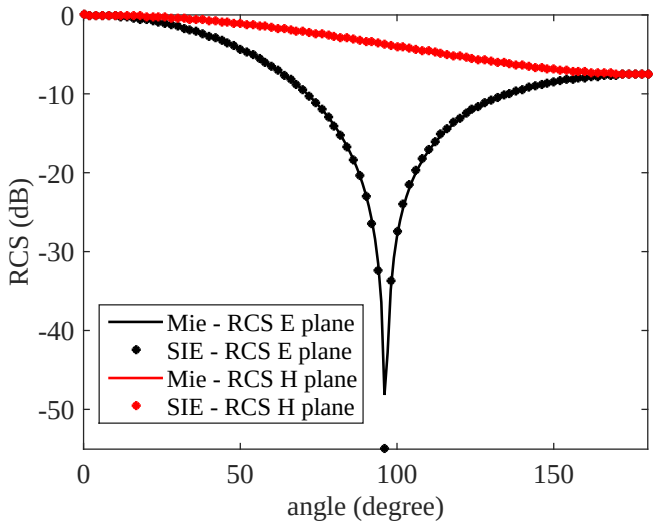

Figure 4.4: A comparison of the simulated RCS and Mie series results on the electric field plane (E plane) and the magnetic field plane (H plane). Parameters used for graphene conductivity are $T = 300$ K, $\tau = 0.1$ ps, and $E_F = 0.4$ eV.

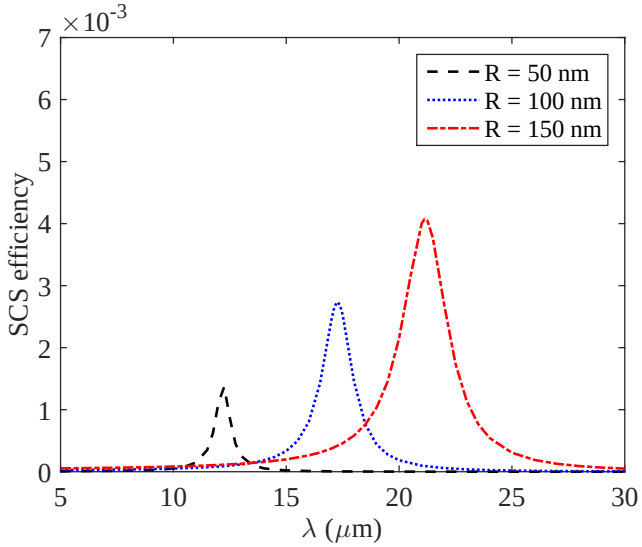

Figure 4.5: Scattering cross section efficiency of the graphene-wrapped dielectric sphere as a function of the incident wavelength for different radii of the sphere at Fermi energy $E_F = 0.3$ eV. The relative permittivity of the background and the dielectric sphere is 2.25. $T = 300$ K, $\tau = 0.1$ ps.

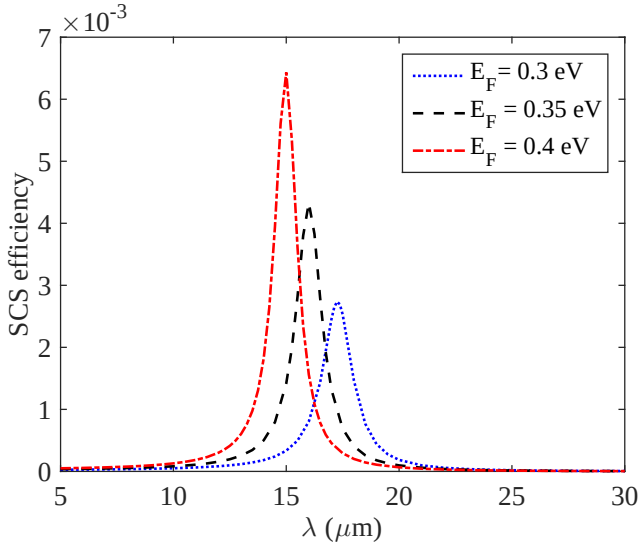

Figure 4.6: Scattering cross section efficiency of the graphene-wrapped dielectric sphere as a function of the incident wavelength for different Fermi energies at a fixed sphere radius $R = 100$ nm. The relative permittivity of the background and the dielectric sphere is 2.25. $T = 300$ K, $\tau = 0.1$ ps.

4.3 Radiative Heat Transfer between Graphene-wrapped Objects

In this section, the flux of radiative heat transfer (RHT) is derived based on surface integral equations. The fluctuating-currents form for the flux of RHT between two dielectric objects is revisited. Afterwards, this methodology is extended to the scenarios of the objects with graphene coating.

4.3.1 Fluctuating-currents form for radiative heat transfer between dielectric objects

The radiative heat transfer between two objects 1 and 2 at local temperatures T_1 and T_2 can be written as [91, 92]

$$\mathcal{H} = \int_0^\infty d\omega[\Theta(\omega, T_1) - \Theta(\omega, T_2)]\Phi(\omega), \tag{4.44}$$

where

$$\Theta(\omega, T) = \frac{\hbar\omega}{e^{\hbar\omega/(k_B T)-1}} \tag{4.45}$$

is the Planck energy per oscillator at temperature T, and Φ is an ensemble-averaged flux spectrum into object 2 due to random currents in object 1. Physically object 2 has random currents inside too; however, the reciprocity explains that the same Φ for flux flows into object 1 due to sources in object 2 [93, 94]. This reciprocity can be interpreted as the symmetry of heat transfer, which has been proved by trace formulas in terms of the scattering operators of the individual object [95]. The problem remaining is to compute Φ. The fluctuating surface current formulation of radiative heat transfer proposed in [74] is the first work to apply surface integral equations to compute Φ for homogeneous dielectric objects with arbitrary shape. The derivation is revisited here, and a supplementary form is provided.

In the previous section, the surface integral equations Eq. (4.4) and Eq. (4.8) have been established for general-purpose which can be extended to two objects here. Different from scattering problems, the source fields come from the interior instead of exterior in the discussion of radiative heat transfer. Consider the system illustrated in Fig. 4.7, consisting of two dielectric objects 1, 2 with homogeneous mediums (V_1 and V_2 with temperatures T_1

and T_2), separated by a lossless medium V_0 by two interfaces S_1 and S_2, respectively. For a dielectric object with homogeneous medium, the tangential fields on the boundary are continuous. Therefore, we can reduce the equivalent surface currents on interior and exterior surfaces of one object to only one set: $(\mathbf{J}_1, \mathbf{M}_1)$ on S_1 and $(\mathbf{J}_2, \mathbf{M}_2)$ on S_2.

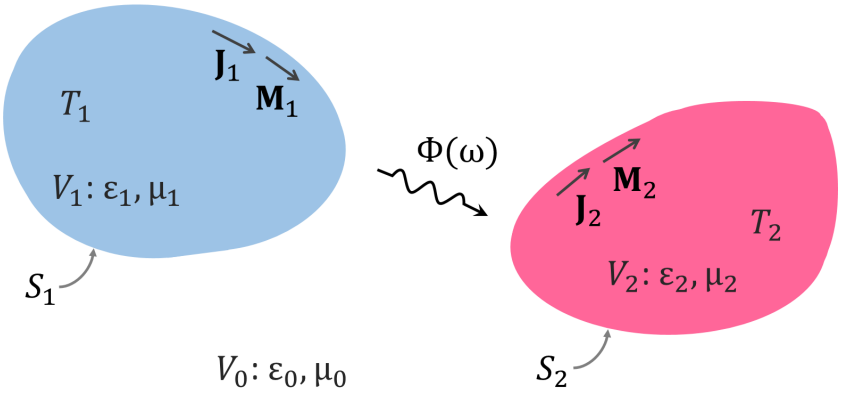

Figure 4.7: Schematic depicting two disconnected dielectric objects 1 and 2, described by surfaces S_1 and S_2, and held at temperatures T_1 and T_2, respectively. Equivalent surface currents $(\mathbf{J}_1, \mathbf{M}_1)$ and $(\mathbf{J}_2, \mathbf{M}_2)$ are defined on S_1 and S_2, respectively. The background medium V_0 is lossless.

Similar to Eq. (4.4) and Eq. (4.8), by applying equivalence principle, the surface integral equations inside objects 1 and 2 can be written as:

$$\frac{1}{2}\mathbf{E}_\ell^{\mathrm{t}}(\mathbf{r}) = \mathbf{E}_\ell^{\mathrm{i}}(\mathbf{r}) - \mathcal{L}_{\ell E}(\mathbf{r}, \mathbf{r}') \cdot \mathbf{J}_\ell(\mathbf{r}') - \mathcal{K}'_{\ell E}(\mathbf{r}, \mathbf{r}') \cdot \mathbf{M}_\ell(\mathbf{r}'), \quad \mathbf{r} \in S_\ell^- \tag{4.46}$$

$$\frac{1}{2}\mathbf{H}_\ell^{\mathrm{t}}(\mathbf{r}) = \mathbf{H}_\ell^{\mathrm{i}}(\mathbf{r}) - \mathcal{L}_{\ell H}(\mathbf{r}, \mathbf{r}') \cdot \mathbf{M}_\ell(\mathbf{r}') - \mathcal{K}'_{\ell H}(\mathbf{r}, \mathbf{r}') \cdot \mathbf{J}_\ell(\mathbf{r}') \quad \mathbf{r} \in S_\ell^-, \tag{4.47}$$

where the subscript $\ell = 1, 2$ indicates which object the equations refer to; and the superscripts t and i represent total and source fields, respectively. Notice that the principal value integrals are applied here. Therefore only half the total field is remaining on the left-hand side for both Eq. (4.46) and Eq (4.47). A more compact form can be written as:

$$\frac{1}{2}\begin{pmatrix}\mathbf{E}_\ell^{\mathrm{t}} \\ \mathbf{H}_\ell^{\mathrm{t}}\end{pmatrix} = \begin{pmatrix}\mathbf{E}_\ell^{\mathrm{i}} \\ \mathbf{H}_\ell^{\mathrm{i}}\end{pmatrix} - \mathbf{Z}_\ell \cdot \begin{pmatrix}\mathbf{J}_\ell \\ \mathbf{M}_\ell\end{pmatrix}, \tag{4.48}$$

where

$$\mathbf{Z}_\ell = \begin{pmatrix} \mathcal{L}_{\ell E} & \mathcal{K}'_{\ell E} \\ \mathcal{K}'_{\ell H} & \mathcal{L}_{\ell H} \end{pmatrix}, \quad \ell = 1, 2. \tag{4.49}$$

Between objects 1 and 2, both $(\mathbf{J}_1, \mathbf{M}_1)$ and $(\mathbf{J}_2, \mathbf{M}_2)$ contribute to the total fields in the background region V_0. Therefore, the surface integral equations on S_1 and S_2 for exterior V_0 can be expressed as:

$$\frac{1}{2}\begin{pmatrix} \mathbf{E}_0^{\mathrm{t}} \\ \mathbf{H}_0^{\mathrm{t}} \end{pmatrix} = \begin{pmatrix} \mathbf{E}_0^{\mathrm{i}} \\ \mathbf{H}_0^{\mathrm{i}} \end{pmatrix} + \mathbf{Z}_0 \cdot \begin{pmatrix} \mathbf{J}_1 \\ \mathbf{M}_1 \end{pmatrix} + \mathbf{Z}_0 \cdot \begin{pmatrix} \mathbf{J}_2 \\ \mathbf{M}_2 \end{pmatrix}, \tag{4.50}$$

where

$$\mathbf{Z}_0 = \begin{pmatrix} \mathcal{L}_{0E} & \mathcal{K}'_{0E} \\ \mathcal{K}'_{0H} & \mathcal{L}_{0H} \end{pmatrix}. \tag{4.51}$$

Note that the detailed elements in $\mathbf{Z}_0$ are dependent on which surface the testing functions are applied to. The tangential fields are continuous at the surface of each object; therefore, combining Eq. (4.48) and Eq. (4.50) results in two sets of integral equations on S_1 and S_2:

$$(\mathbf{Z}_{0,11} + \mathbf{Z}_{1,11}) \cdot \begin{pmatrix} \mathbf{J}_1 \\ \mathbf{M}_1 \end{pmatrix} + \mathbf{Z}_{0,12} \cdot \begin{pmatrix} \mathbf{J}_2 \\ \mathbf{M}_2 \end{pmatrix} = \begin{pmatrix} \mathbf{E}_{1t}^{\mathrm{i}} - \mathbf{E}_{0t}^{\mathrm{i}} \\ \mathbf{H}_{1t}^{\mathrm{i}} - \mathbf{H}_{0t}^{\mathrm{i}} \end{pmatrix} \tag{4.52}$$

$$\mathbf{Z}_{0,21} \cdot \begin{pmatrix} \mathbf{J}_1 \\ \mathbf{M}_1 \end{pmatrix} + (\mathbf{Z}_{0,22} + \mathbf{Z}_{2,22}) \cdot \begin{pmatrix} \mathbf{J}_2 \\ \mathbf{M}_2 \end{pmatrix} = \begin{pmatrix} \mathbf{E}_{2t}^{\mathrm{i}} - \mathbf{E}_{0t}^{\mathrm{i}} \\ \mathbf{H}_{2t}^{\mathrm{i}} - \mathbf{H}_{0t}^{\mathrm{i}} \end{pmatrix}, \tag{4.53}$$

where $\mathbf{E}_{\ell t}^{\mathrm{i}}$ and $\mathbf{H}_{\ell t}^{\mathrm{i}}$ denote the tangential components of $\mathbf{E}_\ell^{\mathrm{i}}$ and $\mathbf{H}_\ell^{\mathrm{i}}$ with $\ell = 0, 1, 2$. The subscripts i, j in $\mathbf{Z}_{0,ij}$, $\mathbf{Z}_{1,ij}$ and $\mathbf{Z}_{2,ij}$ indicate that the testing functions are from surface S_i and the basis functions are from surface S_j when the problem is numerically solved.

For the convenience of derivation, the above integral equations are converted to matrix-vector product form with testing and basis functions applied. Similar to Eq. (4.27) - (4.29), the surface currents can be expanded as:

$$\mathbf{J}_\ell(\mathbf{r}) = \sum_{n=1}^{N} J_{\ell n} \mathbf{f}_{\ell n}(\mathbf{r}), \quad \mathbf{M}_\ell(\mathbf{r}) = \sum_{n=1}^{N} M_{\ell n} \mathbf{f}_{\ell n}(\mathbf{r}), \quad \ell = 1, 2, \tag{4.54}$$

where $\mathbf{f}_{\ell n}(\mathbf{r})$ is known as the basis function (RWG is used in the whole discussion) on surface S_ℓ, and $J_{\ell n}$'s and $M_{\ell n}$'s are the unknown expansion coefficients. After testing the system equations, Eq. (4.52) and Eq. (4.53) can be converted as

$$(\overline{\mathbf{Z}}_0 + \overline{\mathbf{Z}}_1 + \overline{\mathbf{Z}}_2) \cdot \begin{pmatrix} \mathbf{I}_{1J} \\ \mathbf{I}_{1M} \\ \mathbf{I}_{2J} \\ \mathbf{I}_{2M} \end{pmatrix} = \begin{pmatrix} \mathbf{V}_{1E} - \mathbf{V}_{0E,1} \\ \mathbf{V}_{1H} - \mathbf{V}_{0H,1} \\ \mathbf{V}_{2E} - \mathbf{V}_{0E,2} \\ \mathbf{V}_{2H} - \mathbf{V}_{0H,2} \end{pmatrix}, \tag{4.55}$$

where

$$\overline{\mathbf{Z}}_0 = \begin{pmatrix} \overline{\mathbf{Z}}_{0,11} & \overline{\mathbf{Z}}_{0,12} \\ \overline{\mathbf{Z}}_{0,21} & \overline{\mathbf{Z}}_{0,22} \end{pmatrix}, \quad \overline{\mathbf{Z}}_1 = \begin{pmatrix} \overline{\mathbf{Z}}_{1,11} & \mathbf{0} \\ \mathbf{0} & \mathbf{0} \end{pmatrix}, \quad \overline{\mathbf{Z}}_2 = \begin{pmatrix} \mathbf{0} & \mathbf{0} \\ \mathbf{0} & \overline{\mathbf{Z}}_{2,22} \end{pmatrix}, \tag{4.56}$$

with

$$[\overline{\mathbf{Z}}_{\ell,ij}]_{mn} = \langle \mathbf{f}_{im}, \mathbf{Z}_{\ell,ij}, \mathbf{f}_{jn} \rangle, \quad \ell = 0, 1, 2 \tag{4.57}$$

$$[\mathbf{I}_{\ell J}]_n = J_{\ell n}, \quad [\mathbf{I}_{\ell M}]_n = M_{\ell n} \quad \ell = 1, 2 \tag{4.58}$$

$$[\mathbf{V}_{\ell E}]_m = \langle \mathbf{f}_{\ell m}, \mathbf{E}^{\mathrm{i}}_{\ell t} \rangle, \quad [\mathbf{V}_{0E,\ell}]_m = \langle \mathbf{f}_{\ell m}, \mathbf{E}^{\mathrm{i}}_{0t} \rangle, \quad \ell = 1, 2. \tag{4.59}$$

The subscripts ij in $\overline{\mathbf{Z}}$ indicate that the testing functions are from surface S_i and the basis functions are from S_j. The $\langle \cdot, \cdot \rangle$ is defined as (exactly same as Eq. (4.34))

$$\langle \mathbf{f}, \mathbf{g} \rangle = \int \mathbf{f}(\mathbf{r}) \cdot \mathbf{g}(\mathbf{r}) d\mathbf{r}, \tag{4.60}$$

and we will not repeat its definition. The right-hand side of Eq. (4.56) is not calculated explicitly which will be discussed later. To compute the heat flux between the two objects, first we assume the fluctuating currents only exist in the dielectric body of object 1, which means that only $\mathbf{V}_{1E}$ and $\mathbf{V}_{1H}$ are non-zero on the right-hand side of Eq. (4.56). We rewrite Eq. (4.56) as

$$\overline{\mathbf{W}}^{-1} \cdot \mathbf{x} = \mathbf{s}, \tag{4.61}$$

where

$$\overline{\mathbf{W}}^{-1} = \begin{pmatrix} \overline{\mathbf{W}}_{11} & \overline{\mathbf{W}}_{12} \\ \overline{\mathbf{W}}_{21} & \overline{\mathbf{W}}_{22} \end{pmatrix}^{-1} = \overline{\mathbf{Z}}_0 + \overline{\mathbf{Z}}_1 + \overline{\mathbf{Z}}_2 \tag{4.62}$$

$$\mathbf{x} = [\mathbf{I}_{1J}\ \ \mathbf{I}_{1M}\ \ \mathbf{I}_{2J}\ \ \mathbf{I}_{2M}]^T, \quad \mathbf{s} = [\mathbf{V}_{1E}\ \ \mathbf{V}_{1H}\ \ \mathbf{0}\ \ \mathbf{0}]^T. \tag{4.63}$$

The flux spectrum from a single dipole source $\mathbf{s}_i$ (six-component volume electric and magnetic currents) in object 1 into object 2 can be expressed as

$$\begin{aligned}
\Phi_{\mathbf{s}_i} &= -\frac{1}{2}\oiint dS_2\, \mathrm{Re}\,(\mathbf{E}_2 \times \mathbf{H}_2^*)\cdot\mathbf{n} \\
&= -\frac{1}{4}\oiint dS_2\, \mathrm{Re}\,[\mathbf{E}_2\cdot(\mathbf{H}_2^*\times\mathbf{n}) + (\mathbf{n}\times\mathbf{E}_2)\cdot\mathbf{H}_2^*] \\
&= \frac{1}{4}\oiint dS_2\, \mathrm{Re}\,[\mathbf{E}_2\cdot\mathbf{J}_2^* + \mathbf{H}_2^*\cdot\mathbf{M}_2] \\
&= \frac{1}{4}\oiint dS_2\, \mathrm{Re}\,[\mathbf{J}_2^*\cdot\mathbf{E}_2 + \mathbf{M}_2^*\cdot\mathbf{H}_2]\,,
\end{aligned} \tag{4.64}$$

where the superscript $*$ denotes the complex conjugate, and $\mathbf{J}_2 = \mathbf{n}\times\mathbf{H}_2$, $\mathbf{M}_2 = -\mathbf{n}\times\mathbf{E}_2$ on surface S_2. The "Re" means the real part of the variable. Meanwhile, $\mathbf{E}_2$ and $\mathbf{H}_2$ can be expressed by $\mathbf{J}_2$ and $\mathbf{M}_2$ from the interior integral equation for object 2 (described in Eq. (4.48)). Notice that there is a $\frac{1}{2}$ factor on the total fields in Eq. (4.48). Therefore, a 2 factor is included below when converting Eq. (4.64) to a matrix form numerically:

$$\begin{aligned}
\Phi_{\mathbf{s}_i} &= -\frac{1}{2}\mathrm{Re}\big(\mathbf{x}_2^\dagger\cdot\overline{\mathbf{Z}}_{2,22}\cdot\mathbf{x}_2\big) = -\frac{1}{2}\mathrm{Re}\big(\mathbf{x}^\dagger\cdot\overline{\mathbf{Z}}_2\cdot\mathbf{x}\big) \\
&= -\frac{1}{2}\big[\mathbf{x}^\dagger\cdot(\mathrm{sym}\overline{\mathbf{Z}}_2)\cdot\mathbf{x}\big] = -\frac{1}{2}\big[\mathbf{s}^\dagger\cdot\overline{\mathbf{W}}^\dagger\cdot(\mathrm{sym}\overline{\mathbf{Z}}_2)\cdot\overline{\mathbf{W}}\cdot\mathbf{s}\big] \\
&= -\frac{1}{2}\mathrm{Tr}\big[\mathbf{s}^\dagger\cdot\overline{\mathbf{W}}^\dagger\cdot(\mathrm{sym}\overline{\mathbf{Z}}_2)\cdot\overline{\mathbf{W}}\cdot\mathbf{s}\big] \\
&= -\frac{1}{2}\mathrm{Tr}\big[\mathbf{s}\cdot\mathbf{s}^\dagger\cdot\overline{\mathbf{W}}^\dagger\cdot(\mathrm{sym}\overline{\mathbf{Z}}_2)\cdot\overline{\mathbf{W}}\big],
\end{aligned} \tag{4.65}$$

where

$$\mathbf{x}_2 = [\mathbf{I}_{2J}\ \ \mathbf{I}_{2M}]^T, \quad \mathrm{sym}\overline{\mathbf{Z}} = \frac{1}{2}\big(\overline{\mathbf{Z}} + \overline{\mathbf{Z}}^\dagger\big). \tag{4.66}$$

The superscript $\dagger$ denotes the conjugate transpose of a matrix, and the "Tr" means the trace of a matrix. The total flux spectrum is

$$\Phi = \langle\Phi_{\mathbf{s}_i}\rangle = -\frac{1}{2}\mathrm{Tr}\big[\langle\mathbf{s}\cdot\mathbf{s}^\dagger\rangle\cdot\overline{\mathbf{W}}^\dagger\cdot(\mathrm{sym}\overline{\mathbf{Z}}_2)\cdot\overline{\mathbf{W}}\big], \tag{4.67}$$

where an ensemble-average $\langle\cdots\rangle$ over all sources s_i and polarizations in V_1 is involved. The fluctuation-dissipation theorem for the current-current

correlation function is given as

$$\langle \mathbf{s}_i(\mathbf{r}) \cdot \mathbf{s}_i^*(\mathbf{r}') \rangle = \frac{4}{\pi} \omega \mathrm{Im} \overline{\boldsymbol{\chi}}(\mathbf{r}, \omega) \delta(\mathbf{r}, \mathbf{r}'), \tag{4.68}$$

where the dependence on the Planck energy distribution $\Theta(\omega, T)$ has been omitted, which has been factored out into Eq. (4.44). The $\mathrm{Im}\overline{\boldsymbol{\chi}}$ denotes the imaginary part of the material susceptibility tensor (6×6)

$$\mathrm{Im}\overline{\boldsymbol{\chi}} = \begin{pmatrix} \mathrm{Im}\overline{\boldsymbol{\epsilon}} & \mathbf{0} \\ \mathbf{0} & \mathrm{Im}\overline{\boldsymbol{\mu}} \end{pmatrix}, \tag{4.69}$$

which is related to material absorption. By employing the above current-current correlation, a detailed derivation in [74] shows that the ensemble-average $\langle \mathbf{s} \cdot \mathbf{s}^\dagger \rangle$ in Eq. (4.67) can be expressed as

$$\langle \mathbf{s} \cdot \mathbf{s}^\dagger \rangle = -\frac{4}{\pi} \mathrm{sym}\overline{\mathbf{Z}}_1. \tag{4.70}$$

Therefore, the total flux spectrum can be expressed as a compact form:

$$\begin{aligned} \Phi &= \frac{2}{\pi} \mathrm{Tr}\big[\mathrm{sym}\overline{\mathbf{Z}}_1 \cdot \overline{\mathbf{W}}^\dagger \cdot (\mathrm{sym}\overline{\mathbf{Z}}_2) \cdot \overline{\mathbf{W}}\big] \\ &= \frac{2}{\pi} \mathrm{Tr}\big[\mathrm{sym}\overline{\mathbf{Z}}_{1,11} \cdot \overline{\mathbf{W}}_{21}^\dagger \cdot (\mathrm{sym}\overline{\mathbf{Z}}_{2,22}) \cdot \overline{\mathbf{W}}_{21}\big], \end{aligned} \tag{4.71}$$

where $\overline{\mathbf{W}}_{21}$ is given in Eq. (4.62), which relates the incident fields on the surface of object 2 to the equivalent currents on the surface of object 1.

Alternatively, we can derive a new formula of the flux based on the expansion coefficients of the surface currents (defined in Eq. (4.54)), which are the unknowns in the system matrix equation (Eq. (4.62)). More explicitly, the

expansion coefficients are expressed as

$$\mathbf{I}_{2J} = \left[\overline{\mathbf{W}} \cdot \begin{pmatrix} \mathbf{V}_{1E} \\ \mathbf{V}_{1H} \\ \mathbf{0} \\ \mathbf{0} \end{pmatrix}\right]_3 = \overline{\mathbf{W}}_{E,21} \cdot \mathbf{s}_1 \tag{4.72}$$

$$\mathbf{I}_{2M} = \left[\overline{\mathbf{W}} \cdot \begin{pmatrix} \mathbf{V}_{1E} \\ \mathbf{V}_{1H} \\ \mathbf{0} \\ \mathbf{0} \end{pmatrix}\right]_4 = \overline{\mathbf{W}}_{H,21} \cdot \mathbf{s}_1, \tag{4.73}$$

where $\mathbf{s}_1 = [\mathbf{V}_{1E} \ \ \mathbf{V}_{1H}]^T$, and $\overline{\mathbf{W}}_{E,21}$, $\overline{\mathbf{W}}_{H,21}$ are the corresponding matrix blocks in $\overline{\mathbf{W}}$. Then, the flux spectrum $\Phi_{\mathbf{s}_i}$ can be expressed as:

$$\Phi_{\mathbf{s}_i} = -\frac{1}{2}\oiint dS_2 \,\mathrm{Re}(\mathbf{E}_2 \times \mathbf{H}_2^*) \cdot \mathbf{n} \tag{4.74}$$

$$= -\frac{1}{2}\oiint dS_2 \,\mathrm{Re}\left[(\mathbf{n} \times \mathbf{E}_2) \cdot \mathbf{H}_2^*\right] = -\frac{1}{2}\oiint dS_2 \,\mathrm{Re}\left[\mathbf{M}_2 \cdot (\mathbf{n} \times \mathbf{J}_2^*)\right] \tag{4.75}$$

$$= -\frac{1}{2}\sum_{m,n} \mathrm{Re}(M_{2m}^* J_{2n}) \langle \mathbf{f}_m, \mathbf{n} \times \mathbf{f}_n \rangle \tag{4.76}$$

$$= -\frac{1}{2}\mathrm{Re}\big(\mathbf{s}_1^\dagger \cdot \overline{\mathbf{W}}_{H,21}^\dagger \cdot \overline{\mathbf{O}}_{X2} \cdot \overline{\mathbf{W}}_{E,21} \cdot \mathbf{s}_1\big) \tag{4.77}$$

$$= -\frac{1}{2}\mathrm{Re}\big\{\mathrm{Tr}\big[\mathbf{s}_1 \cdot \mathbf{s}_1^\dagger \cdot \overline{\mathbf{W}}_{H,21}^\dagger \cdot \overline{\mathbf{O}}_{X2} \cdot \overline{\mathbf{W}}_{E,21}\big]\big\}, \tag{4.78}$$

where $\overline{\mathbf{O}}_X$ (defined in Eq. (4.33)) is a matrix composed of the inner product of basis function and $\mathbf{n}$ cross basis function. The subscript 2 in $\overline{\mathbf{O}}_X$ means the basis functions are on the surface of object 2. Similarly, the total flux spectrum can be derived as

$$\begin{aligned} \Phi = \langle \Phi_{\mathbf{s}_i} \rangle &= -\frac{1}{2}\mathrm{Re}\big\{\mathrm{Tr}\big[\langle \mathbf{s}_1 \cdot \mathbf{s}_1^\dagger \rangle \cdot \overline{\mathbf{W}}_{H,21}^\dagger \cdot \overline{\mathbf{O}}_{X2} \cdot \overline{\mathbf{W}}_{E,21}\big]\big\} \\ &= \frac{2}{\pi}\mathrm{Re}\big\{\mathrm{Tr}\big[\mathrm{sym}\overline{\mathbf{Z}}_{1,11} \cdot \overline{\mathbf{W}}_{H,21}^\dagger \cdot \overline{\mathbf{O}}_{X2} \cdot \overline{\mathbf{W}}_{E,21}\big]\big\}. \end{aligned} \tag{4.79}$$

The above expression for the total flux spectrum is not as elegant as that in Eq. (4.71), but it is a more straightforward derivation which will be adopted in the cases involving graphene coating. In addition, the step of derivation from a single source to the ensemble-average formula will be omitted in the next sections.

The flux spectrum of two silicon spheres with radius of 800 nm, separated by a 200 nm vacuum gap, is calculated as a benchmark of our solver. The dielectric functions of the silicon spheres are shown in Fig. 4.8 for $T_1 = 400$ K and $T_2 = 300$ K (data obtained from [75]). Numerical results in Fig. 4.9 show the equivalence of these two expressions, i.e., Eq. (4.71) and Eq. (4.79), which are consistent with the results in [75].

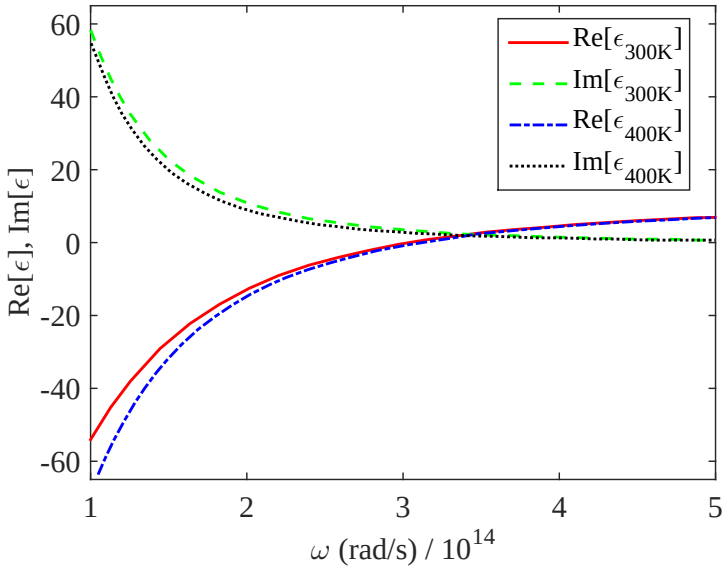

Figure 4.8: The dielectric function of two 10^{20} cm^{-3} n-doped silicon spheres ($T_1 = 400$ K and $T_2 = 300$ K).

4.3.2 Discussion for system with graphene coating

In this section, the radiative heat transfer between two graphene-wrapped objects is discussed. Different from the previous case, the magnetic field becomes discontinuous on the surface due to the surface conductivity of graphene. Consider the system illustrated in Fig. 4.10, consisting of two dielectric objects 1, 2 with graphene coatings (σ_{s1} and σ_{s2}) and homogeneous media (V_1 and V_2 with temperatures T_1 and T_2), separated by a lossless medium V_0 by two interfaces S_1 and S_2, respectively.

Between objects 1 and 2, the surface integral equations on S_1 and S_2 for

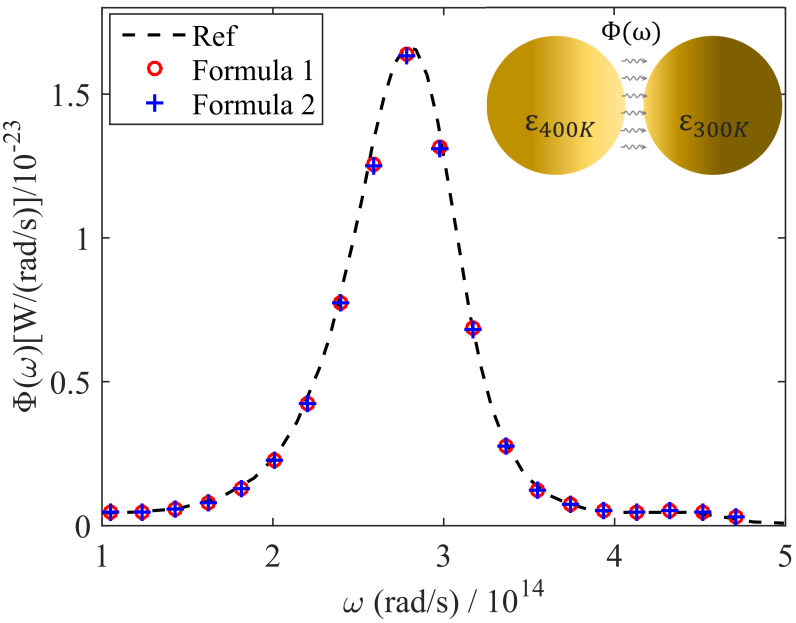

Figure 4.9: The flux spectrum of two silicon spheres with radius of 800 nm, separated by a 200 nm gap. One is held at $T_1 = 400$ K and the other is at $T_2 = 300$ K. 'Formula 1' and 'Formula 2' refer to Eq. (4.71) and Eq. (4.79) with the factor of Plank energy per oscillator $\Theta(\omega, T_1) - \Theta(\omega, T_2)$ included. 'Ref' is obtained from [75], which is also calculated based on surface integral equation.

exterior V_0 are expressed as:

$$\frac{1}{2}\begin{pmatrix}\mathbf{E}_0^{\mathrm{t}}\\ \mathbf{H}_0^{\mathrm{t}}\end{pmatrix} = \begin{pmatrix}\mathbf{E}_0^{\mathrm{i}}\\ \mathbf{H}_0^{\mathrm{i}}\end{pmatrix} + \mathbf{Z}^0 \cdot \begin{pmatrix}\mathbf{J}_1^{+}\\ \mathbf{M}_1^{+}\end{pmatrix} + \mathbf{Z}^0 \cdot \begin{pmatrix}\mathbf{J}_2^{+}\\ \mathbf{M}_2^{+}\end{pmatrix}, \tag{4.80}$$

where $\mathbf{Z}^0$ is defined in Eq. (4.51). The discontinuities of the tangential magnetic field on the surfaces can be expressed as:

$$\mathbf{H}_{0t}^{\mathrm{t}} - \mathbf{H}_{1t}^{\mathrm{t}} = \mathbf{J}_{\sigma 1} \times \mathbf{n} = \sigma_{s1}\mathbf{E}_{1t}^{\mathrm{t}} \times \mathbf{n} = \sigma_{s1}\mathbf{M}_1 \tag{4.81}$$

$$\mathbf{H}_{0t}^{\mathrm{t}} - \mathbf{H}_{2t}^{\mathrm{t}} = \mathbf{J}_{\sigma 2} \times \mathbf{n} = \sigma_{s2}\mathbf{E}_{2t}^{\mathrm{t}} \times \mathbf{n} = \sigma_{s2}\mathbf{M}_2. \tag{4.82}$$

To build the system matrix with the discontinuities of magnetic field, some mathematical manipulations are applied here. First, we expand $\mathbf{E}_{1t}^{\mathrm{t}}$ with RWG functions, and denote E_{1n}^{t}'s as the expansion coefficients. By testing

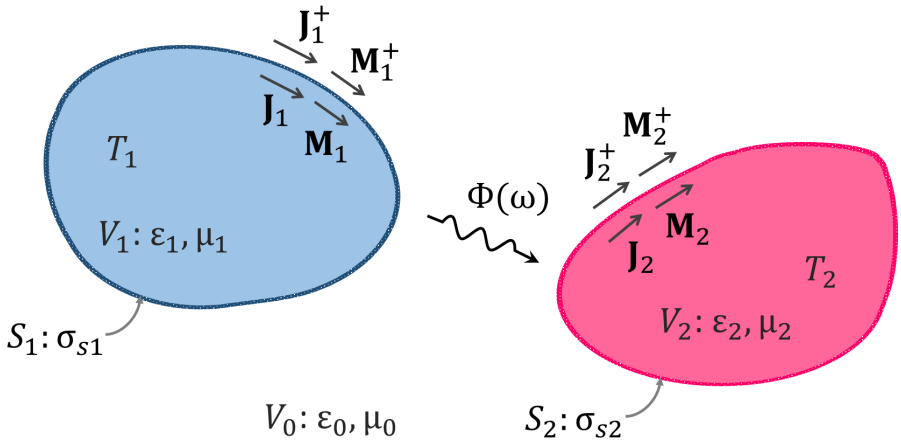

Figure 4.10: Schematic depicting two disconnected dielectric objects 1 and 2, described by surfaces S_1 and S_2, and held at temperatures T_1 and T_2, respectively. The graphene coating for each object is denoted by the surface conductivity, i.e., σ_{s1} and σ_{s2}. Here $(\mathbf{J}_1^+, \mathbf{M}_1^+)$ and $(\mathbf{J}_2^+, \mathbf{M}_2^+)$ are the exterior equivalent surface currents, while $(\mathbf{J}_1, \mathbf{M}_1)$ and $(\mathbf{J}_2, \mathbf{M}_2)$ are the interior equivalent surface currents for each object. The background medium V_0 is lossless.

the left-hand side of Eq. (4.81) and $\mathbf{E}_{1t}^{\mathrm{t}}$ with RWG function $\mathbf{f}_m$, we have

$$\langle \mathbf{f}_m, \mathbf{H}_{0t}^{\mathrm{t}} - \mathbf{H}_{1t}^{\mathrm{t}} \rangle = \sigma_{s1} \langle \mathbf{f}_m, \mathbf{E}_{1t}^{\mathrm{t}} \times \mathbf{n} \rangle = -\sigma_{s1} \sum_n \langle \mathbf{f}_m, \mathbf{n} \times \mathbf{f}_n \rangle E_{1n}^{\mathrm{t}} \tag{4.83}$$

$$\langle \mathbf{f}_m, \mathbf{E}_{1t}^{\mathrm{t}} \rangle = \sum_n \langle \mathbf{f}_m, \mathbf{f}_n \rangle E_{1n}^{\mathrm{t}}. \tag{4.84}$$

Rewriting the above two equations in matrix representation, we have

$$\mathbf{V}_{0H}^{\mathrm{t}} - \mathbf{V}_{1H}^{\mathrm{t}} = -\sigma_{s1} \overline{\mathbf{O}}_X \cdot \mathbf{I}_{1E}^{\mathrm{t}} \tag{4.85}$$

$$\mathbf{V}_{1E}^{\mathrm{t}} = \overline{\mathbf{G}}_{1M} \cdot \mathbf{I}_{1E}^{\mathrm{t}}, \tag{4.86}$$

where

$$[\mathbf{V}_{0H}^{\mathrm{t}}]_m = \langle \mathbf{f}_m, \mathbf{H}_{0t}^{\mathrm{t}} \rangle, \quad [\mathbf{V}_{1H}^{\mathrm{t}}]_m = \langle \mathbf{f}_m, \mathbf{H}_{1t}^{\mathrm{t}} \rangle \tag{4.87}$$

$$[\mathbf{V}_{1E}^{\mathrm{t}}]_m = \langle \mathbf{f}_m, \mathbf{E}_{1t}^{\mathrm{t}} \rangle, \quad [\mathbf{I}_{1E}^{\mathrm{t}}]_n = E_{1n}^{\mathrm{t}}. \tag{4.88}$$

Just as a reminder, here $\overline{\mathbf{G}}_M$ is the Gram matrix of RWG basis functions (defined in Eq. (4.32)), and $\overline{\mathbf{O}}_X$ is a matrix composed of the inner product of basis function and $\mathbf{n}$ cross basis function, given in Eq. (4.33). Furthermore,

we have

$$\mathbf{V}_{0H}^{\mathrm{t}} - \mathbf{V}_{1H}^{\mathrm{t}} = -\sigma_{s1}\overline{\mathbf{O}}_{X1} \cdot \overline{\mathbf{G}}_{M1}^{-1} \cdot \mathbf{V}_{1E}^{\mathrm{t}}. \tag{4.89}$$

Therefore, on the surface of object 1, the tangential components of the total fields from exterior and interior can be linked as

$$\begin{pmatrix} \bar{\mathbf{I}} & \mathbf{0} \\ \sigma_{s1}\overline{\mathbf{O}}_{X1} \cdot \overline{\mathbf{G}}_{M1}^{-1} & \bar{\mathbf{I}} \end{pmatrix} \cdot \begin{pmatrix} \mathbf{V}_{0E}^{\mathrm{t}} \\ \mathbf{V}_{0H}^{\mathrm{t}} \end{pmatrix} = \overline{\mathbf{T}}_{L1} \cdot \begin{pmatrix} \mathbf{V}_{0E}^{\mathrm{t}} \\ \mathbf{V}_{0H}^{\mathrm{t}} \end{pmatrix} = \begin{pmatrix} \mathbf{V}_{1E}^{\mathrm{t}} \\ \mathbf{V}_{1H}^{\mathrm{t}} \end{pmatrix}, \tag{4.90}$$

where

$$\overline{\mathbf{T}}_{L\ell} = \begin{pmatrix} \bar{\mathbf{I}} & \mathbf{0} \\ \sigma_{s\ell}\overline{\mathbf{O}}_{X\ell} \cdot \overline{\mathbf{G}}_{M\ell}^{-1} & \bar{\mathbf{I}} \end{pmatrix}, \quad \ell = 1, 2. \tag{4.91}$$

The same scenario applies to the relation of the fields on the surface of object 2.

Second, we reduce the equivalent surface currents to the interior sets, i.e., $(\mathbf{J}_1, \mathbf{M}_1)$ and $(\mathbf{J}_2, \mathbf{M}_2)$. In Section 4.2, the relations between exterior and interior equivalent surface currents have been derived (Eq. (4.26)):

$$\begin{aligned} \mathbf{J}_1^+ &= \mathbf{J}_1 + \sigma_{s1}\mathbf{n} \times \mathbf{M}_1, \quad \mathbf{M}_1^+ = \mathbf{M}_1 \\ \mathbf{J}_2^+ &= \mathbf{J}_2 + \sigma_{s2}\mathbf{n} \times \mathbf{M}_2, \quad \mathbf{M}_2^+ = \mathbf{M}_2. \end{aligned} \tag{4.92}$$

Similar to Eq. (4.35), the relations between the corresponding expansion coefficients can be numerically written as

$$\begin{pmatrix} \mathbf{I}_{1J}^+ \\ \mathbf{I}_{1M}^+ \end{pmatrix} = \overline{\mathbf{T}}_{R1} \cdot \begin{pmatrix} \mathbf{I}_{1J} \\ \mathbf{I}_{1M} \end{pmatrix} \tag{4.93}$$

$$\begin{pmatrix} \mathbf{I}_{2J}^+ \\ \mathbf{I}_{2M}^+ \end{pmatrix} = \overline{\mathbf{T}}_{R2} \cdot \begin{pmatrix} \mathbf{I}_{2J} \\ \mathbf{I}_{2M} \end{pmatrix}, \tag{4.94}$$

where

$$\overline{\mathbf{T}}_{R\ell} = \begin{pmatrix} \bar{\mathbf{I}} & \sigma_{s\ell}\overline{\mathbf{G}}_{M\ell}^{-1} \cdot \overline{\mathbf{O}}_{X\ell} \\ \mathbf{0} & \bar{\mathbf{I}} \end{pmatrix}, \quad \ell = 1, 2. \tag{4.95}$$

Notice that $\overline{\mathbf{T}}_L$ is not the transpose of $\overline{\mathbf{T}}_R$, because $\overline{\mathbf{O}}_X^T = -\overline{\mathbf{O}}_X$ and $\overline{\mathbf{G}}_M^T = \overline{\mathbf{G}}_M$. This is important which we will discuss later.

Combining the exterior integral equation with interior integral equations for each object, the matrix formula of the system equation can be written as:

$$\left(\overline{\mathbf{T}}_{L1}\cdot\overline{\mathbf{Z}}_{0,11}\cdot\overline{\mathbf{T}}_{R1}+\overline{\mathbf{Z}}_{1,11}\right)\cdot\begin{pmatrix}\mathbf{I}_{1J}\\ \mathbf{I}_{1M}\end{pmatrix}+\overline{\mathbf{T}}_{L1}\cdot\overline{\mathbf{Z}}_{0,12}\cdot\overline{\mathbf{T}}_{R2}\cdot\begin{pmatrix}\mathbf{I}_{2J}\\ \mathbf{I}_{2M}\end{pmatrix} = \begin{pmatrix}\mathbf{V}_{1E}\\ \mathbf{V}_{1H}\end{pmatrix}-\overline{\mathbf{T}}_{L1}\cdot\begin{pmatrix}\mathbf{V}_{0E,1}\\ \mathbf{V}_{0H,1}\end{pmatrix} \tag{4.96}$$

$$\overline{\mathbf{T}}_{L2}\cdot\overline{\mathbf{Z}}_{0,21}\cdot\overline{\mathbf{T}}_{R1}\cdot\begin{pmatrix}\mathbf{I}_{1J}\\ \mathbf{I}_{1M}\end{pmatrix}+\left(\overline{\mathbf{T}}_{L2}\cdot\overline{\mathbf{Z}}_{0,22}\cdot\overline{\mathbf{T}}_{R2}+\overline{\mathbf{Z}}_{2,22}\right)\cdot\begin{pmatrix}\mathbf{I}_{2J}\\ \mathbf{I}_{2M}\end{pmatrix} = \begin{pmatrix}\mathbf{V}_{2E}\\ \mathbf{V}_{2H}\end{pmatrix}-\overline{\mathbf{T}}_{L2}\cdot\begin{pmatrix}\mathbf{V}_{0E,2}\\ \mathbf{V}_{0H,2}\end{pmatrix}, \tag{4.97}$$

where $\mathbf{I}_{\ell J}$, $\mathbf{I}_{\ell M}$, $\mathbf{V}_{\ell E}$, $\mathbf{V}_{\ell H}$, $\mathbf{V}_{0E,\ell}$ and $\mathbf{V}_{0H,\ell}$ with $\ell = 1, 2$ have been defined before (Eq. (4.58) and Eq. (4.59)).

To adopt the expression of the ensemble-average source for electric body in [74], i.e., Eq. (4.70), we need to formulate the equations maintaining symmetry in the original electromagnetics problem. This is a key to guarantee the symmetry of heat transfer between the two objects for reciprocal material. In fact, we can make the problem complex symmetric by transforming $\mathbf{M}$, $\mathbf{H}$ to $i\mathbf{M}$, $i\mathbf{H}$. Then the operator composed with dyadic Green's functions and the transformer matrices $(\overline{\mathbf{T}}_R, \overline{\mathbf{T}}_L)$ are formulated as

$$\mathbf{Z} = \begin{pmatrix}\mathcal{L}_E & i\mathcal{K}'_E\\ i\mathcal{K}'_E & \mathcal{L}_H\end{pmatrix} \tag{4.98}$$

$$\overline{\mathbf{T}}_R = \overline{\mathbf{T}} = \begin{pmatrix}\bar{\mathbf{I}} & -i\sigma_s\overline{\mathbf{G}}_M^{-1}\cdot\overline{\mathbf{O}}_X\\ \mathbf{0} & \bar{\mathbf{I}}\end{pmatrix} \tag{4.99}$$

$$\overline{\mathbf{T}}_L = \overline{\mathbf{T}}^T = \begin{pmatrix}\bar{\mathbf{I}} & \mathbf{0}\\ i\sigma_s\overline{\mathbf{O}}_X\cdot\overline{\mathbf{G}}_M^{-1} & \bar{\mathbf{I}}\end{pmatrix}. \tag{4.100}$$

The system matrix-vector product formula (Eq. (4.96) and Eq. (4.97)) can be expressed as:

$$\overline{\mathbf{Z}} \cdot \begin{pmatrix} \mathbf{I}_{1J} \\ i\mathbf{I}_{1M} \\ \mathbf{I}_{2J} \\ i\mathbf{I}_{2M} \end{pmatrix} = \begin{pmatrix} \mathbf{V}_{1E} - \mathbf{V}_{0E,1} \\ i\mathbf{V}_{1H} - i\mathbf{V}_{0H,1} - i\sigma_{s1}\overline{\mathbf{O}}_{X1} \cdot \overline{\mathbf{G}}_{M1}^{-1} \cdot \mathbf{V}_{0E,1} \\ \mathbf{V}_{2E} - \mathbf{V}_{0E,2} \\ i\mathbf{V}_{2H} - i\mathbf{V}_{0H,2} - i\sigma_{s2}\overline{\mathbf{O}}_{X2} \cdot \overline{\mathbf{G}}_{M2}^{-1} \cdot \mathbf{V}_{0E,2} \end{pmatrix}, \tag{4.101}$$

where the impedance matrix $\overline{\mathbf{Z}}$ is

$$\overline{\mathbf{Z}} = \begin{pmatrix} \overline{\mathbf{T}}_1^T \cdot \overline{\mathbf{Z}}_{0,11} \cdot \overline{\mathbf{T}}_1 + \overline{\mathbf{Z}}_{11} & \overline{\mathbf{T}}_1^T \cdot \overline{\mathbf{Z}}_{0,12} \cdot \overline{\mathbf{T}}_2 \\ \overline{\mathbf{T}}_2^T \cdot \overline{\mathbf{Z}}_{0,21} \cdot \overline{\mathbf{T}}_1 & \overline{\mathbf{T}}_2^T \cdot \overline{\mathbf{Z}}_{0,22} \cdot \overline{\mathbf{T}}_2 + \overline{\mathbf{Z}}_{22} \end{pmatrix} = \overline{\mathbf{W}}^{-1}. \tag{4.102}$$

Therefore we can follow the procedure in previous section to compute the heat flux spectrum from dielectric body of object 1 to the dielectric body of object 2 with graphene coatings. Also if σ_{s1} and σ_{s2} are zeros, Eq. (4.101) is restored to Eq. (4.55) derived in last section without graphene coating. However, since the surface conductivity of the graphene is complex, the graphene layer is also radiating and absorbing energies. In the following section, we will first examine the fluctuation dissipation theorem in a two-dimensional material. Then we will apply this relation to calculate the radiative heat flux contributed from the graphene coating.

4.3.3 Fluctuating-currents form for radiative heat transfer between graphene-wrapped dielectric objects

To derive the current-current correlation function for two-dimensional (2D) material, first we write the current-current correlation function for volume currents explicitly as

$$\overline{J_\ell(\mathbf{r},\omega)J_m^*(\mathbf{r}',\omega)} = \frac{4}{\pi}\omega\Theta(\omega,T)\delta(\mathbf{r}-\mathbf{r}')\mathrm{Im}[\epsilon(\mathbf{r},\omega)]\epsilon_0\delta_{\ell m}, \tag{4.103}$$

where the overline denotes an ensemble average, and $\ell, m = 1, 2, 3$ denote the spatial directions. Here $\Theta(\omega, T)$ is the Planck energy per oscillator at temperature T given in Eq. (4.45).

To reduce the dimension to 2D, the following relations can be applied:

$$J_\ell(\mathbf{r},\omega) = J_{s,\ell}(\boldsymbol{\rho},\omega)\delta(z) \tag{4.104}$$

$$\delta(\mathbf{r}-\mathbf{r}') = \delta_s(\boldsymbol{\rho}-\boldsymbol{\rho}')\delta(z) \tag{4.105}$$

$$\mathrm{Im}[\epsilon(\mathbf{r},\omega)] = \mathrm{Im}\big[i\frac{\sigma_s(\boldsymbol{\rho},\omega)}{\epsilon_0\omega}\big] = \frac{\mathrm{Re}[\sigma_s(\boldsymbol{\rho},\omega)]}{\epsilon_0\omega}\delta(z). \tag{4.106}$$

Therefore, Eq. (4.103) is reduced to

$$\overline{J_{s,\ell}(\boldsymbol{\rho},\omega)J^*_{s,m}(\boldsymbol{\rho}',\omega)} = \frac{4}{\pi}\Theta(\omega,T)\delta_s(\boldsymbol{\rho}-\boldsymbol{\rho}')\mathrm{Re}[\sigma_s(\boldsymbol{\rho},\omega)]\delta_{\ell m}. \tag{4.107}$$

In Section 4.3.2, the "fluctuating" current sources inside graphene are not included in the system equation. To be consistent, $(\mathbf{J}_1,\mathbf{M}_1)$ and $(\mathbf{J}_2,\mathbf{M}_2)$ are used to denote the interior equivalent surface currents for objects 1 and 2. Accordingly, $(\mathbf{J}_1^+,\mathbf{M}_1^+)$ and $(\mathbf{J}_2^+,\mathbf{M}_2^+)$ are the exterior equivalent surface currents. Besides, $\mathbf{J}_{s1}$ and $\mathbf{J}_{s2}$ are the fluctuating surface currents in graphene layers of object 1 and 2, respectively. These surface currents can be related as:

$$\begin{aligned} \mathbf{J}_1^+ &= \mathbf{J}_1 + \sigma_{s1}\mathbf{n}\times\mathbf{M}_1 + \mathbf{J}_{s1}, \quad \mathbf{M}_1^+ = \mathbf{M}_1 \\ \mathbf{J}_2^+ &= \mathbf{J}_2 + \sigma_{s2}\mathbf{n}\times\mathbf{M}_2 + \mathbf{J}_{s2}, \quad \mathbf{M}_2^+ = \mathbf{M}_2. \end{aligned} \tag{4.108}$$

Similar to Eq. (4.93) and Eq. (4.94), the relations between the corresponding expansion coefficients can be numerically written as

$$\begin{pmatrix}\mathbf{I}_{1J}^+\\ \mathbf{I}_{1M}^+\end{pmatrix} = \overline{\mathbf{T}}_{R1}\cdot\begin{pmatrix}\mathbf{I}_{1J}\\ \mathbf{I}_{1M}\end{pmatrix} + \begin{pmatrix}\mathbf{I}_{s1}\\ \mathbf{0}\end{pmatrix} \tag{4.109}$$

$$\begin{pmatrix}\mathbf{I}_{2J}^+\\ \mathbf{I}_{2M}^+\end{pmatrix} = \overline{\mathbf{T}}_{R2}\cdot\begin{pmatrix}\mathbf{I}_{2J}\\ \mathbf{I}_{2M}\end{pmatrix} + \begin{pmatrix}\mathbf{I}_{s2}\\ \mathbf{0}\end{pmatrix}. \tag{4.110}$$

The discontinuity relations of tangential magnetic fields (Eq. (4.81) and Eq. (4.82)) on the surfaces of each object also need to be modified as:

$$\mathbf{H}_{0t}^{\mathrm{t}} - \mathbf{H}_{1t}^{\mathrm{t}} = (\mathbf{J}_{\sigma1}+\mathbf{J}_{s1})\times\mathbf{n} = \sigma_{s1}\mathbf{M}_1 + \mathbf{J}_{s1}\times\mathbf{n} \tag{4.111}$$

$$\mathbf{H}_{0t}^{\mathrm{t}} - \mathbf{H}_{2t}^{\mathrm{t}} = (\mathbf{J}_{\sigma2}+\mathbf{J}_{s2})\times\mathbf{n} = \sigma_{s2}\mathbf{M}_2 + \mathbf{J}_{s2}\times\mathbf{n}. \tag{4.112}$$

In the same fashion as Eq. (4.90), the tangential components of the total

fields from exterior and interior can be linked as

$$\begin{pmatrix} \bar{\mathbf{I}} & \mathbf{0} \\ \sigma_{s1}\overline{\mathbf{O}}_{X1}\cdot\overline{\mathbf{G}}_{M1}^{-1} & \bar{\mathbf{I}} \end{pmatrix}\cdot\begin{pmatrix} \mathbf{V}_{0E}^{\mathrm{t}} \\ \mathbf{V}_{0H}^{\mathrm{t}} \end{pmatrix} = \overline{\mathbf{T}}_{L1}\cdot\begin{pmatrix} \mathbf{V}_{0E}^{\mathrm{t}} \\ \mathbf{V}_{0H}^{\mathrm{t}} \end{pmatrix} = \begin{pmatrix} \mathbf{V}_{1E}^{\mathrm{t}} \\ \mathbf{V}_{1H}^{\mathrm{t}} - \overline{\mathbf{O}}_{X1}\cdot\mathbf{I}_{s1} \end{pmatrix}. \tag{4.113}$$

By introducing the terms of fluctuating surface currents in graphene into Eq. (4.96) and Eq. (4.97), the matrix formula of the system equation is updated as:

$$\begin{aligned} &\left(\overline{\mathbf{T}}_{L1}\cdot\overline{\mathbf{Z}}_{0,11}\cdot\overline{\mathbf{T}}_{R1}+\overline{\mathbf{Z}}_{1,11}\right)\cdot\begin{pmatrix}\mathbf{I}_{1J}\\ \mathbf{I}_{1M}\end{pmatrix}+\overline{\mathbf{T}}_{L1}\cdot\overline{\mathbf{Z}}_{0,11}\cdot\begin{pmatrix}\mathbf{I}_{s1}\\ \mathbf{0}\end{pmatrix} \\ &\qquad+\overline{\mathbf{T}}_{L1}\cdot\overline{\mathbf{Z}}_{0,12}\cdot\overline{\mathbf{T}}_{R2}\cdot\begin{pmatrix}\mathbf{I}_{2J}\\ \mathbf{I}_{2M}\end{pmatrix}+\overline{\mathbf{T}}_{L1}\cdot\overline{\mathbf{Z}}_{0,12}\cdot\begin{pmatrix}\mathbf{I}_{s2}\\ \mathbf{0}\end{pmatrix} \\ &\qquad=\begin{pmatrix}\mathbf{V}_{1E}\\ \mathbf{V}_{1H}\end{pmatrix}-\overline{\mathbf{T}}_{L1}\cdot\begin{pmatrix}\mathbf{V}_{0E,1}\\ \mathbf{V}_{0H,1}\end{pmatrix}-\begin{pmatrix}\mathbf{0}\\ \frac{1}{2}\overline{\mathbf{O}}_{X1}\cdot\mathbf{I}_{s1}\end{pmatrix} \end{aligned} \tag{4.114}$$

$$\begin{aligned} &\overline{\mathbf{T}}_{L2}\cdot\overline{\mathbf{Z}}_{0,21}\cdot\overline{\mathbf{T}}_{R1}\cdot\begin{pmatrix}\mathbf{I}_{1J}\\ \mathbf{I}_{1M}\end{pmatrix}+\overline{\mathbf{T}}_{L2}\cdot\overline{\mathbf{Z}}_{0,21}\cdot\begin{pmatrix}\mathbf{I}_{s1}\\ \mathbf{0}\end{pmatrix} \\ &\qquad+\left(\overline{\mathbf{T}}_{L2}\cdot\overline{\mathbf{Z}}_{0,22}\cdot\overline{\mathbf{T}}_{R2}+\overline{\mathbf{Z}}_{2,22}\right)\cdot\begin{pmatrix}\mathbf{I}_{2J}\\ \mathbf{I}_{2M}\end{pmatrix}+\overline{\mathbf{T}}_{L2}\cdot\overline{\mathbf{Z}}_{0,22}\begin{pmatrix}\mathbf{I}_{s2}\\ \mathbf{0}\end{pmatrix} \\ &\qquad=\begin{pmatrix}\mathbf{V}_{2E}\\ \mathbf{V}_{2H}\end{pmatrix}-\overline{\mathbf{T}}_{L2}\cdot\begin{pmatrix}\mathbf{V}_{0E,2}\\ \mathbf{V}_{0H,2}\end{pmatrix}-\begin{pmatrix}\mathbf{0}\\ \frac{1}{2}\overline{\mathbf{O}}_{X2}\cdot\mathbf{I}_{s2}\end{pmatrix}. \end{aligned} \tag{4.115}$$

Now we modify the system matrix to be symmetric by changing $\mathbf{M}$ to $i\mathbf{M}$ and $\mathbf{H}$ to $i\mathbf{H}$. The general version of Eq. (4.114) and Eq. (4.115) in complex symmetric fashion is written as (all the items containing sources have been moved to the right-hand side)

$$\overline{\mathbf{Z}}\cdot\begin{pmatrix}\mathbf{I}_{1J}\\ i\mathbf{I}_{1M}\\ \mathbf{I}_{2J}\\ i\mathbf{I}_{2M}\end{pmatrix}=\overline{\mathbf{V}}+\overline{\mathbf{R}}_1\cdot\mathbf{I}_{s1}+\overline{\mathbf{R}}_2\cdot\mathbf{I}_{s2}, \tag{4.116}$$

where

$$\overline{\mathbf{V}} = \begin{pmatrix} \mathbf{V}_{1E} - \mathbf{V}_{0E,1} \\ i\mathbf{V}_{1H} - i\mathbf{V}_{0H,1} - i\sigma_{s1}\overline{\mathbf{O}}_{X1} \cdot \overline{\mathbf{G}}_{M1}^{-1} \cdot \mathbf{V}_{0E,1} \\ \mathbf{V}_{2E} - \mathbf{V}_{0E,2} \\ i\mathbf{V}_{2H} - i\mathbf{V}_{0H,2} - i\sigma_{s2}\overline{\mathbf{O}}_{X2} \cdot \overline{\mathbf{G}}_{M2}^{-1} \cdot \mathbf{V}_{0E,2} \end{pmatrix} \tag{4.117}$$

$$\tag{4.118}$$

$$\overline{\mathbf{R}}_1 = \begin{pmatrix} \mathcal{L}_{0E,11} \\ i\mathcal{K}'_{0E,11} + i\frac{1}{2}\overline{\mathbf{O}}_{X1} + i\sigma_{s1}\overline{\mathbf{O}}_{X1} \cdot \overline{\mathbf{G}}_{M1}^{-1} \cdot \mathcal{L}_{0E,11} \\ \mathcal{L}_{0E,21} \\ i\mathcal{K}'_{0E,21} + i\sigma_{s2}\overline{\mathbf{O}}_{X2} \cdot \overline{\mathbf{G}}_{M2}^{-1} \cdot \mathcal{L}_{0E,21} \end{pmatrix} \tag{4.119}$$

$$\tag{4.120}$$

$$\overline{\mathbf{R}}_2 = \begin{pmatrix} \mathcal{L}_{0E,12} \\ i\mathcal{K}'_{0E,12} + i\sigma_{s1}\overline{\mathbf{O}}_{X1} \cdot \overline{\mathbf{G}}_{M1}^{-1} \cdot \mathcal{L}_{0E,12} \\ \mathcal{L}_{0E,22} \\ i\mathcal{K}'_{0E,22} + i\frac{1}{2}\overline{\mathbf{O}}_{X2} + i\sigma_{s2}\overline{\mathbf{O}}_{X2} \cdot \overline{\mathbf{G}}_{M2}^{-1} \cdot \mathcal{L}_{0E,22} \end{pmatrix}. \tag{4.121}$$

Therefore, if only the fluctuating sources inside the graphene coating of object 1 are considered, the expansion coefficients of the equivalent surface currents on the inner surface of object 2 can be expressed as

$$\mathbf{I}_{2J} = [\overline{\mathbf{Z}}^{-1} \cdot \overline{\mathbf{R}}_1]_3 \cdot \mathbf{I}_{s1} = \overline{\mathbf{W}}_{sE,21} \cdot \mathbf{I}_{s1} \tag{4.122}$$

$$i\mathbf{I}_{2M} = [\overline{\mathbf{Z}}^{-1} \cdot \overline{\mathbf{R}}_1]_4 \cdot \mathbf{I}_{s1} = \overline{\mathbf{W}}_{sH,21} \cdot \mathbf{I}_{s1}, \tag{4.123}$$

where the subscripts 3 and 4 denote the corresponding blocks of the matrix, and the subscript s in $\overline{\mathbf{W}}$ is used to distinguish from previous definitions (Eq. (4.72) and Eq. (4.73)) in which the sources are from dielectric body.

Similar to the derivations in Eq. (4.74), the flux absorbed by the dielectric

body of object 2 is calculated as follows:

$$\begin{aligned}
\Phi_{\mathbf{s}_i} &= -\frac{1}{2}\oiint dS_2\,\mathrm{Re}(\mathbf{E}_2\times\mathbf{H}_2^*)\cdot\mathbf{n}\\
&= -\frac{1}{2}\oiint dS_2\,\mathrm{Re}[(\mathbf{n}\times\mathbf{E}_2)\cdot\mathbf{H}_2^*] = -\frac{1}{2}\oiint dS_2\,\mathrm{Re}[\mathbf{M}_2\cdot(\mathbf{n}\times\mathbf{J}_2^*)]\\
&= -\frac{1}{2}\sum_{m,n}\mathrm{Re}(M_{2m}^*J_{2n})\langle\mathbf{f}_m,\mathbf{n}\times\mathbf{f}_n\rangle\\
&= -\frac{1}{2}\sum_{m,n}\mathrm{Im}[(-iM_{2m})^*J_{2n}]\langle\mathbf{f}_m,\mathbf{n}\times\mathbf{f}_n\rangle\\
&= -\frac{1}{2}\mathrm{Im}\big(-\mathbf{I}_{s1}^\dagger\cdot\overline{\mathbf{W}}_{sH,21}^\dagger\cdot\overline{\mathbf{O}}_{X2}\cdot\overline{\mathbf{W}}_{sE,21}\cdot\mathbf{I}_{s1}\big)\\
&= \frac{1}{2}\mathrm{Im}\big\{\mathrm{Tr}\big[\mathbf{I}_{s1}\cdot\mathbf{I}_{s1}^\dagger\cdot\overline{\mathbf{W}}_{sH,21}^\dagger\cdot\overline{\mathbf{O}}_{X2}\cdot\overline{\mathbf{W}}_{sE,21}\big]\big\}.
\end{aligned} \tag{4.124}$$

The total flux spectrum is an ensemble-average of $\Phi_{\mathbf{s}_i}$ over all sources $\mathbf{J}_{s1}$ and polarizations in surface S_1. Therefore, we need to find the ensemble-average of $\mathbf{I}_{s1}\cdot\mathbf{I}_{s1}^\dagger$ in Eq. (4.124), denoted as a matrix $\overline{\mathbf{C}}=\langle\mathbf{I}_{s1}\cdot\mathbf{I}_{s1}^\dagger\rangle$. And $\mathbf{I}_{s1}$ is the vector of the expansion coefficients of the surface fluctuating currents $\mathbf{J}_{s1}$ in the graphene layer. Therefore, we have

$$\mathbf{J}_{s1}(\mathbf{r}) = \sum_n J_{s1,n}\mathbf{f}_n(\mathbf{r}) \tag{4.125}$$

$$[\mathbf{I}_{s1}]_n = J_{s1,n} \tag{4.126}$$

$$[\overline{\mathbf{C}}]_{mn} = \langle J_{s1,m}J_{s1,n}^*\rangle. \tag{4.127}$$

By testing Eq. (4.125) with basis functions and employing the fluctuation-dissipation theorem derived in Eq. (4.107), we have

$$\overline{\mathbf{F}}\cdot\mathbf{J}_{s1} = \overline{\mathbf{G}}_{M1}\cdot\mathbf{I}_{s1},\quad [\overline{\mathbf{F}}]_m=\mathbf{f}_m \tag{4.128}$$

$$\begin{aligned}
\langle\overline{\mathbf{F}}\cdot\mathbf{J}_{s1}\cdot\mathbf{J}_{s1}^\dagger\cdot\overline{\mathbf{F}}^T\rangle &= \overline{\mathbf{F}}\cdot\langle\mathbf{J}_{s1}\cdot\mathbf{J}_{s1}^\dagger\rangle\cdot\overline{\mathbf{F}}^T = \frac{4}{\pi}\mathrm{Re}[\sigma_{s1}(\omega)]\overline{\mathbf{F}}\cdot\overline{\mathbf{F}}^T\\
&= \frac{4}{\pi}\mathrm{Re}[\sigma_{s1}(\omega)]\overline{\mathbf{G}}_{M1}\\
&= \langle\overline{\mathbf{G}}_{M1}\cdot\mathbf{I}_{s1}\cdot\mathbf{I}_{s1}^\dagger\cdot\overline{\mathbf{G}}_{M1}^T\rangle = \overline{\mathbf{G}}_{M1}\cdot\langle\mathbf{I}_{s1}\cdot\mathbf{I}_{s1}^\dagger\rangle\cdot\overline{\mathbf{G}}_{M1}^T\\
&= \overline{\mathbf{G}}_{M1}\cdot\overline{\mathbf{C}}\cdot\overline{\mathbf{G}}_{M1}^T,
\end{aligned} \tag{4.129}$$

where we assumed the surface conductivity as a constant over the surface and omitted the Planck energy $\Theta(\omega, T)$ which has been factored out into Eq. (4.44). The Gram matrix $\overline{\mathbf{G}}_{M1}$ is relevant to the basis functions on surface S_1 and $\overline{\mathbf{G}}_{M1} = \overline{\mathbf{G}}_{M1}^T$. Therefore

$$\overline{\mathbf{C}} = \frac{4}{\pi}\mathrm{Re}[\sigma_{s1}(\omega)]\overline{\mathbf{G}}_{M1}^{-1}. \tag{4.130}$$

The total flux spectrum then is expressed as

$$\begin{aligned}\Phi = \langle \Phi_{\mathbf{s}_i} \rangle &= \frac{1}{2}\mathrm{Im}\big\{\mathrm{Tr}\big[\langle \mathbf{I}_{s1} \cdot \mathbf{I}_{s1}^{\dagger} \rangle \cdot \overline{\mathbf{W}}_{sH,21}^{\dagger} \cdot \overline{\mathbf{O}}_{X2} \cdot \overline{\mathbf{W}}_{sE,21}\big]\big\} \\ &= \frac{2}{\pi}\mathrm{Im}\big\{\mathrm{Re}[\sigma_{s1}(\omega)]\mathrm{Tr}\big[\overline{\mathbf{G}}_{M1}^{-1} \cdot \overline{\mathbf{W}}_{sH,21}^{\dagger} \cdot \overline{\mathbf{O}}_{X2} \cdot \overline{\mathbf{W}}_{sE,21}\big]\big\}.\end{aligned} \tag{4.131}$$

Now we have established the expression of total flux spectrum due to fluctuating-current sources in graphene layer absorbed by the dielectric body of object 2 since only the interior surface currents in object 2 are considered. In the next section, different scenarios of the sources and the bodies to absorb the flux will be discussed in the next section.

4.3.4 Discussion

In previous sections, the expressions of total flux spectrum for fluctuating-current sources in both dielectric body and graphene layer have been established respectively. A general matrix equation of the system is given in Eq. (4.116) with an imaginary unit i multiplied to $\mathbf{M}$ and $\mathbf{H}$.

A. Sources from dielectric body

When the sources are from the dielectric body of object 1, $\mathbf{s}_1$ is non-zero while $\mathbf{J}_{s1}$ is zero. Both the dielectric body and the graphene layer of object 2 absorb the flux radiated from object 1. The expansion coefficients of the

interior surface currents in object 2 are expressed as:

$$\mathbf{I}_{2J} = \left[\overline{\mathbf{W}} \cdot \begin{pmatrix} \mathbf{V}_{1E} \\ i\mathbf{V}_{1H} \\ \mathbf{0} \\ \mathbf{0} \end{pmatrix}\right]_3 = \overline{\mathbf{W}}_{E,21} \cdot \mathbf{s}_1 \tag{4.132}$$

$$i\mathbf{I}_{2M} = \left[\overline{\mathbf{W}} \cdot \begin{pmatrix} \mathbf{V}_{1E} \\ i\mathbf{V}_{1H} \\ \mathbf{0} \\ \mathbf{0} \end{pmatrix}\right]_4 = \overline{\mathbf{W}}_{H,21} \cdot \mathbf{s}_1 \tag{4.133}$$

with $\mathbf{s}_1 = [\mathbf{V}_{1E} \quad i\mathbf{V}_{1H}]^T$. According to the relations between interior and exterior surface currents, the expansion coefficients of the exterior surface currents on object 2 are expressed as:

$$\begin{aligned} \mathbf{I}_{2J}^{+} &= \mathbf{I}_{2J} + \sigma_{s2}\overline{\mathbf{G}}_{M2}^{-1} \cdot \overline{\mathbf{O}}_{X2} \cdot \mathbf{I}_{2M} \\ &= \left[\overline{\mathbf{W}}_{E,21} + \sigma_{s2}\overline{\mathbf{G}}_{M2}^{-1} \cdot \overline{\mathbf{O}}_{X2} \cdot (-i)\overline{\mathbf{W}}_{H,21}\right] \cdot \mathbf{s}_1 \end{aligned} \tag{4.134}$$

$$\mathbf{I}_{2M}^{+} = \mathbf{I}_{2M} = \overline{\mathbf{W}}_{H,21} \cdot \mathbf{s}_1. \tag{4.135}$$

Then the total flux spectrum from object 1 to object 2 can be expressed as:

$$\begin{aligned} \Phi_{1\to 2} &= -\frac{1}{2}\oiint dS_2 \,\mathrm{Re}(\mathbf{E}_2 \times \mathbf{H}_2^*) \cdot \mathbf{n} \\ &= -\frac{1}{2}\oiint dS_2 \,\mathrm{Re}[\mathbf{M}_2^{+} \cdot (\mathbf{n} \times \mathbf{J}_2^{+*})] \\ &= -\frac{1}{2}\sum_{m,n} \mathrm{Re}(M_{2m}^{+*} J_{2n}^{+}) \langle \mathbf{f}_m, \mathbf{n} \times \mathbf{f}_n \rangle \\ &= -\frac{1}{2}\sum_{m,n} \mathrm{Im}[(-iM_{2m}^{+})^* J_{2n}^{+}] \langle \mathbf{f}_m, \mathbf{n} \times \mathbf{f}_n \rangle \\ &= -\frac{2}{\pi}\mathrm{Im}\big\{\mathrm{Tr}\big[\mathrm{sym}\overline{\mathbf{Z}}_{1,11} \cdot \overline{\mathbf{W}}_{H,21}^{\dagger} \cdot \overline{\mathbf{O}}_{X2} \cdot \overline{\mathbf{W}}_{E,21}\big]\big\} \\ &+ \frac{2}{\pi}\mathrm{Re}\big\{\sigma_{s2}(\omega)\mathrm{Tr}\big[\mathrm{sym}\overline{\mathbf{Z}}_{1,11} \cdot \overline{\mathbf{W}}_{H,21}^{\dagger} \cdot \overline{\mathbf{O}}_{X2} \cdot \overline{\mathbf{G}}_{M2}^{-1} \cdot \overline{\mathbf{O}}_{X2} \cdot \overline{\mathbf{W}}_{H,21}\big]\big\}. \end{aligned} \tag{4.136}$$

In the last line of the above equation, the first term corresponds to the flux absorbed by the dielectric body of object 2 while the second term represents

the flux absorbed by the graphene layer of object 2. A more compact form for the first term has been given in Sec. 4.3.1 with validation of equality to the above one. Therefore, the total flux spectrum due to the fluctuating currents in dielectric body of object 1 can also be expressed as:

$$\begin{aligned}\Phi_{1\to2} = &\frac{2}{\pi}\mathrm{Re}\big\{\mathrm{Tr}\big[\mathrm{sym}\overline{\mathbf{Z}}_{1,11}\cdot\overline{\mathbf{W}}_{21}^{\dagger}\cdot\mathrm{sym}\overline{\mathbf{Z}}_{2,22}\cdot\overline{\mathbf{W}}_{21}\big]\big\}\\ &+\frac{2}{\pi}\mathrm{Re}\big\{\sigma_{s2}(\omega)\mathrm{Tr}\big[\mathrm{sym}\overline{\mathbf{Z}}_{1,11}\cdot\overline{\mathbf{W}}_{H,21}^{\dagger}\cdot\overline{\mathbf{O}}_{X2}\cdot\overline{\mathbf{G}}_{M2}^{-1}\cdot\overline{\mathbf{O}}_{X2}\cdot\overline{\mathbf{W}}_{H,21}\big]\big\},\end{aligned} \tag{4.137}$$

where $\overline{\mathbf{W}}_{21} = [\overline{\mathbf{W}}_{E,21} \quad \overline{\mathbf{W}}_{H,21}]^T$.

B. Sources from graphene layer

Now we assume the fluctuating currents only exist in the graphene layer of object 1. Hence $\mathbf{J}_{s1}$ is non-zero while $\mathbf{s}_1$ is zero.

Similar to the process of deriving Eq. (4.136), the total flux spectrum can be derived as:

$$\begin{aligned}\Phi_{1\to2} = &-\frac{2}{\pi}\mathrm{Re}\big\{\mathrm{Re}[\sigma_{s1}(\omega)]\mathrm{Tr}\big[\overline{\mathbf{G}}_{M1}^{-1}\cdot\overline{\mathbf{W}}_{s,21}^{\dagger}\cdot\mathrm{sym}\overline{\mathbf{Z}}_{2,22}\cdot\overline{\mathbf{W}}_{s,21}\big]\big\}\\ &-\frac{2}{\pi}\mathrm{Re}\big\{\mathrm{Re}[\sigma_{s1}(\omega)]\sigma_{s2}(\omega)\mathrm{Tr}\big[\overline{\mathbf{G}}_{M1}^{-1}\cdot\overline{\mathbf{W}}_{sH,21}^{\dagger}\cdot\overline{\mathbf{O}}_{X2}\cdot\overline{\mathbf{G}}_{M2}^{-1}\cdot\overline{\mathbf{O}}_{X2}\cdot\overline{\mathbf{W}}_{sH,21}\big]\big\},\end{aligned} \tag{4.138}$$

where $\overline{\mathbf{W}}_{s,21} = [\overline{\mathbf{W}}_{sE,21} \quad \overline{\mathbf{W}}_{sH,21}]^T$; and $\overline{\mathbf{W}}_{sE,21}$, $\overline{\mathbf{W}}_{sH,21}$ are defined in Eq. (4.122) and Eq. (4.123). The first and second terms correspond to the flux absorbed by the dielectric body and graphene layer of object 2, respectively.

C. Summary for the formulation of flux spectrum

Here we list the flux spectrum separately for each pair. All fluctuating

currents are from object 1.

$$\Phi_{d1\to d2} = \frac{2}{\pi}\mathrm{Re}\big\{\mathrm{Tr}\big[\mathrm{sym}\overline{\mathbf{Z}}_{1,11}\cdot\overline{\mathbf{W}}_{21}^{\dagger}\cdot\mathrm{sym}\overline{\mathbf{Z}}_{2,22}\cdot\overline{\mathbf{W}}_{21}\big]\big\} \tag{4.139}$$

$$\Phi_{d1\to g2} = \frac{2}{\pi}\mathrm{Re}\big\{\sigma_{s2}\mathrm{Tr}\big[\mathrm{sym}\overline{\mathbf{Z}}_{1,11}\cdot\overline{\mathbf{W}}_{H,21}^{\dagger}\cdot\overline{\mathbf{O}}_{X2}\cdot\overline{\mathbf{G}}_{M2}^{-1}\cdot\overline{\mathbf{O}}_{X2}\cdot\overline{\mathbf{W}}_{H,21}\big]\big\} \tag{4.140}$$

$$\Phi_{g1\to d2} = -\frac{2}{\pi}\mathrm{Re}\big\{\mathrm{Re}[\sigma_{s1}]\mathrm{Tr}\big[\overline{\mathbf{G}}_{M1}^{-1}\cdot\overline{\mathbf{W}}_{s,21}^{\dagger}\cdot\mathrm{sym}\overline{\mathbf{Z}}_{2,22}\cdot\overline{\mathbf{W}}_{s,21}\big]\big\} \tag{4.141}$$

$$\Phi_{g1\to g2} = -\frac{2}{\pi}\mathrm{Re}\big\{\mathrm{Re}[\sigma_{s1}]\sigma_{s2}\mathrm{Tr}\big[\overline{\mathbf{G}}_{M1}^{-1}\cdot\overline{\mathbf{W}}_{sH,21}^{\dagger}\cdot\overline{\mathbf{O}}_{X2}\cdot\overline{\mathbf{G}}_{M2}^{-1}\cdot\overline{\mathbf{O}}_{X2}\cdot\overline{\mathbf{W}}_{sH,21}\big]\big\}, \tag{4.142}$$

where the subscripts "d" and "g" denote dielectric body and graphene layer, respectively. The (ω) in σ_{s1} and σ_{s2} is omitted for simplicity.

Now we check the reciprocity of the flux spectrum in our derivations. The flux absorbed by object 2 due to sources in object 1 should be equal to the flux absorbed by object 1 due to sources in object 2. It is easy to check the case of dielectric body to dielectric body due to the symmetry in Eq. (4.139). That is

$$\begin{aligned}\Phi_{d2\to d1} &= \frac{2}{\pi}\mathrm{Re}\big\{\mathrm{Tr}\big[\mathrm{sym}\overline{\mathbf{Z}}_{2,22}\cdot\overline{\mathbf{W}}_{12}^{\dagger}\cdot\mathrm{sym}\overline{\mathbf{Z}}_{1,11}\cdot\overline{\mathbf{W}}_{12}\big]\big\} \\ &= \frac{2}{\pi}\mathrm{Re}\big\{\mathrm{Tr}\big[\mathrm{sym}\overline{\mathbf{Z}}_{1,11}\cdot\overline{\mathbf{W}}_{21}^{\dagger}\cdot\mathrm{sym}\overline{\mathbf{Z}}_{2,22}\cdot\overline{\mathbf{W}}_{21}\big]\big\} = \Phi_{d1\to d2}.\end{aligned} \tag{4.143}$$

However it is not straightforward to prove the reciprocity of the flux between dielectric body and graphene layer mathematically. The flux spectrum from the dielectric body of object 2 to the graphene layer of object 1 can be expressed by interchanging the indices in Eq. (4.140):

$$\Phi_{d2\to g1} = \frac{2}{\pi}\mathrm{Re}\big\{\sigma_{s1}\mathrm{Tr}\big[\mathrm{sym}\overline{\mathbf{Z}}_{2,22}\cdot\overline{\mathbf{W}}_{H,12}^{\dagger}\cdot\overline{\mathbf{O}}_{X1}\cdot\overline{\mathbf{G}}_{M1}^{-1}\cdot\overline{\mathbf{O}}_{X1}\cdot\overline{\mathbf{W}}_{H,12}\big]\big\}. \tag{4.144}$$

Similarly, the flux spectra from the graphene layer of object 2 to the dielectric body and the graphene layer of object 1 can be expressed by interchanging

the indices in Eq. (4.141) and Eq. (4.142) respectively. They are:

$$\Phi_{g2\to d1} = -\frac{2}{\pi}\mathrm{Re}\big\{\mathrm{Re}[\sigma_{s2}]\mathrm{Tr}\big[\overline{\mathbf{G}}_{M2}^{-1}\cdot\overline{\mathbf{W}}_{s,12}^{\dagger}\cdot\mathrm{sym}\overline{\mathbf{Z}}_{1,11}\cdot\overline{\mathbf{W}}_{s,12}\big]\big\} \tag{4.145}$$

$$\Phi_{g2\to g1} = -\frac{2}{\pi}\mathrm{Re}\big\{\mathrm{Re}[\sigma_{s2}]\sigma_{s1}\mathrm{Tr}\big[\overline{\mathbf{G}}_{M2}^{-1}\cdot\overline{\mathbf{W}}_{sH,12}^{\dagger}\cdot\overline{\mathbf{O}}_{X1}\cdot\overline{\mathbf{G}}_{M1}^{-1}\cdot\overline{\mathbf{O}}_{X1}\cdot\overline{\mathbf{W}}_{sH,12}\big]\big\}. \tag{4.146}$$

We will demonstrate $\Phi_{d1\to g2} = \Phi_{g2\to d1}$, $\Phi_{g1\to d2} = \Phi_{d2\to g1}$ and $\Phi_{g1\to g2} = \Phi_{g2\to g1}$ numerically.

Figure 4.11 (a)-(d) are the flux spectra for the above expressions between a graphene-wrapped sphere and a graphene-wrapped cylinder with $\Theta(\omega, T_1) - \Theta(\omega, T_2)$ included. The sphere with radius of 400 nm is held at $T_1 = 400$ K, while the cylinder is held at $T_2 = 300$ K. The dielectric properties are the same as the case for two silicon spheres in Fig. 4.8. The surface conductivity of the graphene is calculated by (4.39) with $E_F = 0.6$ eV and $\tau = 0.6$ ps. The total flux spectrum between the two objects is given in Fig. 4.12, compared with the case without graphene. The peak is slightly blue shifted with graphene layer.

Figure 4.13 shows the flux of two graphene-wrapped dielectric spheres with $\epsilon = 2.25$ as a function of their separation d, in which the wavelength is 11 μm. Large enhancement in the near field region is observed. Parameters for graphene surface conductivity are $E_F = 0.5$ eV, $\tau = 0.01$ ps, $T = 300$ K. The flux spectrum with $d = 50$ nm is given in the inset. The resonant peak is due to graphene plasmonics.

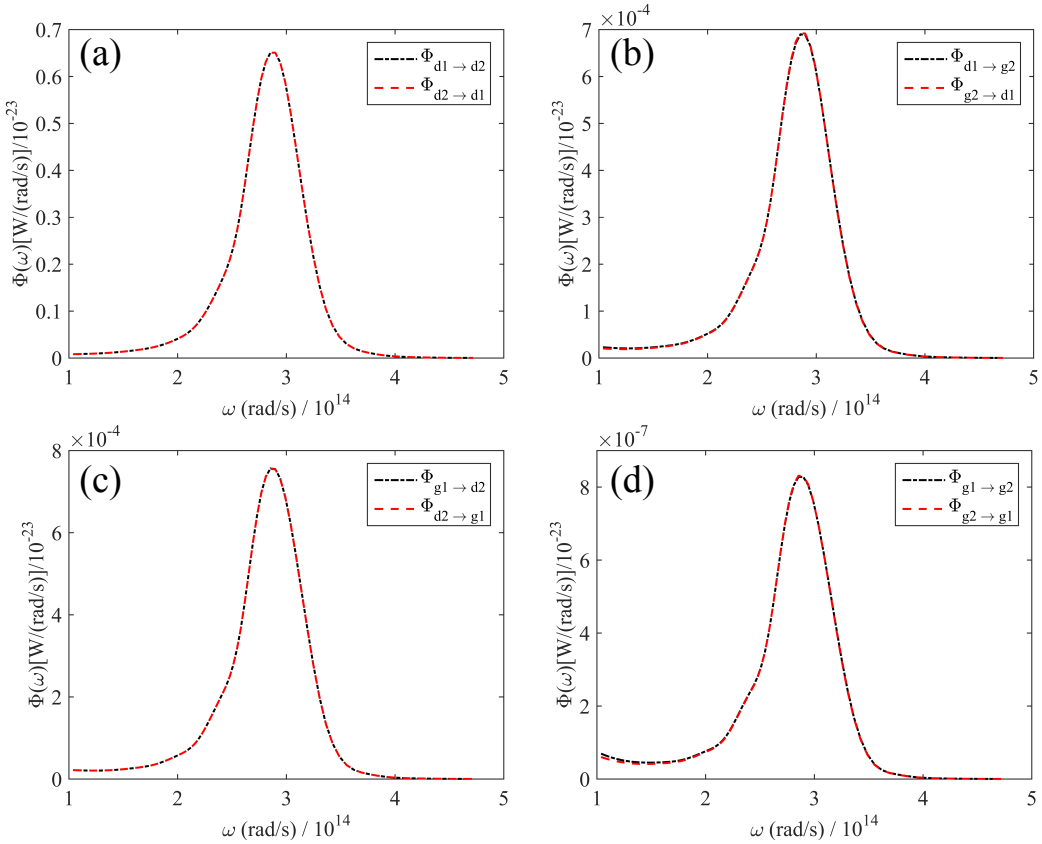

Figure 4.11: Reciprocity check for the expressions of the flux spectrum between two graphene-wrapped silicon objects with different shapes: a sphere and a cylinder separated by 200 nm.

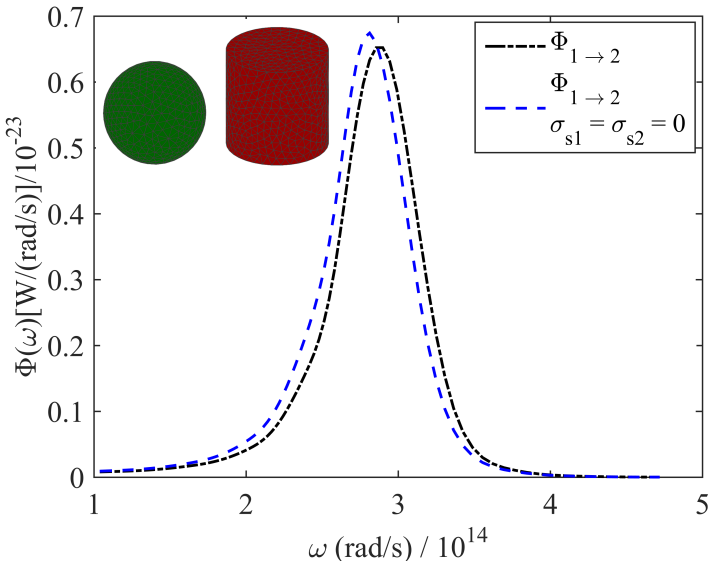

Figure 4.12: Total flux spectrum between the two graphene-wrapped silicon objects: sphere and cylinder. The blue-dashed line corresponds to the case without graphene coatings for comparison.

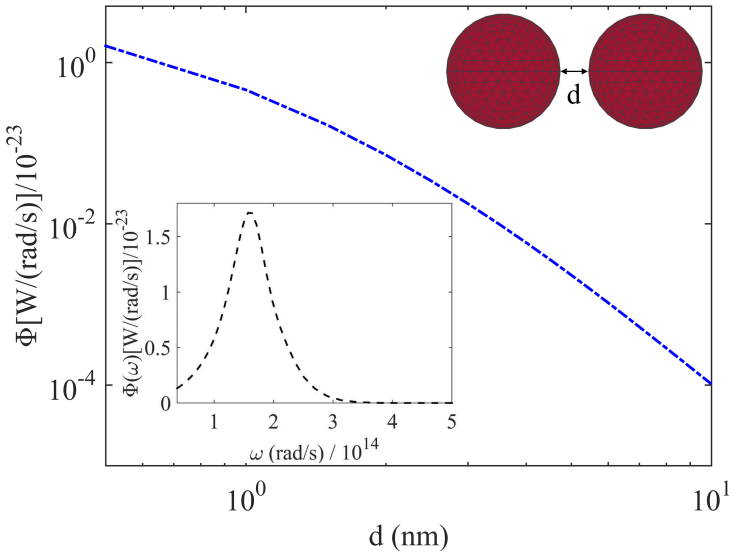

Figure 4.13: Flux spectrum between the two graphene-wrapped dielectric spheres as a function of their separation d at wavelength $\lambda = 11$ μm. The radius of the sphere is 100 nm. Inset: flux spectrum with $d = 50$ nm.

4.4 Conclusion

In this chapter, the fluctuating-surface-current formulation of radiative heat transfer has been extended to study the scenarios with graphene-wrapped objects. It can be restored to the case of pure dielectric objects by setting the surface conductivity as zero. Actually, this expression is not restricted to graphene only. For a thin object coating with complex surface conductivity, for example, the monolayer of transition-metal dichalcogenide discussed in Chapter 3, the expression is still valid. Therefore, more combinations of different materials with different shapes can be explored in this area.

CHAPTER 5

CONCLUSIONS

In this dissertation, we establish a novel two-dimensional (2D) fast multipole algorithm which has high accuracy and efficiency in broadband. Combining it with the 2D volume integral equation, the solver can handle the simulations of devices built with photonic crystals and imaging algorithms with inverse scattering problems. Then we design a metasurface platform composed of transition-metal dichalcogenide (TMDC) flake to generate structured light at second harmonics, in which the electric field integral equation with impedance boundary condition is employed. The monolayer of transition-metal dichalcogenide has strong quadratic nonlinear susceptibility in visible regime with three-fold rotation symmetrical crystalline structure. Radial polarization and azimuthal polarization can be achieved at second-harmonic generation with the incidence of linear polarized plane-wave at the fundamental frequency. This platform can also generate orbital angular momentum of lower orders at second harmonics with the incidence of circular polarized plane-wave at the fundamental frequency. After the analysis of TMDC, we propose a fluctuating-surface-current formulation of radiative heat transfer for graphene-wrapped objects by surface integral equations with impedance boundary conditions. This generalized form can be restored to the scenarios of pure dielectric objects without graphene coatings.

Future work can be done in establishing the surface integral equations for the configurations in which the coating of the 2D materials covers part of the object, for instance, graphene patch antennas and the TMDC metasurface with substrates. The nonlinear analysis of graphene is also another interesting topic, since graphene has large third-harmonic generation. More applications can be explored with the optical properties of the 2D materials and complex geometric configurations.

REFERENCES

[1] W. C. Chew, J. M. Jin, E. Michielssen, and J. M. Song, *Fast and Efficient Algorithms in Computational Electromagnetics*. Norwood, MA: Artech House, 2001.

[2] K. Yee, "Numerical solution of initial boundary value problems involving Maxwell's equations in isotropic media," *IEEE Trans. Antennas Propag.*, vol. 14, no. 3, pp. 302–307, 1966.

[3] J. M. Jin, *The Finite Element Method in Electromagnetics*. John Wiley & Sons, 2015.

[4] W. C. Chew, *Waves and Fields in Inhomogeneous Media*. New York: IEEE Press, 1995.

[5] W. C. Chew, M. S. Tong, and B. Hu, "Integral equation methods for electromagnetic and elastic waves," *Synthesis Lectures on Computational Electromagnetics*, vol. 3, no. 1, pp. 1–241, 2008.

[6] L. J. Jiang and W. C. Chew, "A mixed-form fast multipole algorithm," *IEEE Trans. Antennas Propag.*, vol. 53, no. 12, pp. 4145–4156, Dec. 2005.

[7] L. L. Meng, X. Y. Z. Xiong, T. Xia, and L. J. Jiang, "The error control of mixed-form fast multipole algorithm based on the high order multipole rotation," *IEEE Antennas Wirel. Propag. Lett.*, vol. 16, pp. 1655–1658, Jan. 2017.

[8] T. Xia, L. L. Meng, Q. S. Liu, H. H. Gan, and W. C. Chew, "A low-frequency stable broadband multilevel fast multipole algorithm using plane wave multipole hybridization," *IEEE Trans. Antennas Propag.*, vol. 66, no. 11, pp. 6137–6145, 2018.

[9] L. L. Meng, M. Hidayetoğlu, T. Xia, W. E. I. Sha, L. J. Jiang, and W. C. Chew, "A wideband 2-D fast multipole algorithm with a novel diagonalization form," *IEEE Trans. Antennas Propag.*, vol. 66, no. 12, pp. 7477–7482, 2018.

[10] M. Weismann and N. C. Panoiu, "Theoretical and computational analysis of second-and third-harmonic generation in periodically patterned graphene and transition-metal dichalcogenide monolayers," *Phys. Rev. B*, vol. 94, no. 3, p. 035435, 2016.

[11] L. L. Meng, X. Y. Z. Xiong, T. Xia, Q. S. Liu, L. J. Jiang, W. E. I. Sha, and W. C. Chew, "Second-harmonic generation of structured light by transition-metal dichalcogenide metasurfaces," *Phys. Rev. A*, vol. 102, no. 4, p.043508, 2020.

[12] L. Greengard, *The Rapid Evaluation of Potential Fields in Particle Systems.* London, U.K.: Ph.D. dissertation, MIT Press, 1987.

[13] R. Coifman, V. Rokhlin, and S. Wandzura, "The fast multipole method for the wave equation: a pedestrian prescription," *IEEE Antennas Propag. Mag.*, vol. 35, pp. 7–12, 1993.

[14] W. C. Chew, S. Koc, J. M. Song, C. C. Lu, and E. Michielssen, "A succinct way to diagonalize the translation matrix in three dimensions," *Microw. Opt. Technol. Lett.*, vol. 15, no. 3, pp. 144–147, 1997.

[15] T. Xia, H. Gan, M. Wei, Z. G. Q. K. A. W. C. Chew, H. Braunisch, and A. Aydiner, "An enhanced augmented electric field integral equation formulation for dielectric objects," *IEEE Trans. Antennas Propag.*, vol. 64, no. 6, pp. 2339–2347, 2016.

[16] B. Michiels, J. Fostier, I. Bogaert, and D. D. Zutter, "Full-wave simulations of electromagnetic scattering problems with billions of unknowns," *IEEE Trans. Antennas Propag.*, vol. 63, no. 2, pp. 796–799, Feb. 2015.

[17] I. Bogaert, D. Pissoort, and F. Olyslager, "A normalized plane-wave method for 2D Helmholtz problems," *Microw. Opt. Technol. Lett.*, vol. 48, no. 2, pp. 237–243, Feb. 2006.

[18] M. Hidayetoğlu, C. Pearson, I. E. Hajj, L. Gürel, W. C. Chew, and W.-M. Hwu, "A fast and massively-parallel solver for nonlinear tomographic image reconstruction," *Int. Parallel Distributed Processing Symp. (IPDPS)*, Vancouver, Canada, May, 2018.

[19] Ö. Ergül and B. Karaosmanoğlu, "Broadband multilevel fast multipole algorithm based on an approximate diagonalization of the Green's function," *IEEE Trans. Antennas Propag.*, vol. 63, no. 7, pp. 3035–3041, July, 2015.

[20] J. Gu, D. Ding, Z. He, and R. Chen, "A low-frequency EFIE-MLFMA solver based on approximate diagonalization of Green's function," *IEEE Trans. Antennas Propag.*, vol. 65, no. 12, pp. 7150–7156, Dec. 2017.

[21] H. Wallén and J. Sarvas, "Translation procedures for broadband MLFMA," *Progress in Electromagnetics Research*, vol. 55, pp. 47–78, 2005.

[22] I. Bogaert, J. Peeters, and F. Olyslager, "A nondirective plane wave MLFMA stable at low frequencies," *IEEE Trans. Antennas Propag.*, vol. 56, no. 12, pp. 3752–3767, Dec. 2008.

[23] H. Cheng, W. Y. Crutchfield, Z. Gimbutas, L. F. Greengard, J. F. Ethridge, J. Huang, V. Rokhlin, N. Yarvin, and J. Zhao, "A wideband fast multipole method for the Helmholtz equation in three dimensions," *J. Comp. Phys.*, vol. 216, pp. 300–325, Jan. 2006.

[24] A. F. Peterson, S. L. Ray, and R. Mittra, *Computational Methods for Electromagnetics*. New York: IEEE Press, 1998.

[25] S. Guo and S. Albin, "Numerical techniques for excitation and analysis of defect modes in photonic crystals," *Opt. Express*, vol. 11, no. 9, pp. 1080–1089, May 2003.

[26] A. Mekis, J. C. Chen, I. Kurland, S. Fan, P. R. Villeneuve, and J. D. Joannopoulos, "High transmission through sharp bends in photonic crystal waveguides," *Phys. Rev. Lett.*, vol. 77, no. 18, pp. 3787–3790, Oct. 1996.

[27] F. Cardano and L. Marrucci, "Spin-orbit photonics," *Nat. Photonics*, vol. 9, no. 12, p. 776, 2015.

[28] S. Restuccia, D. Giovannini, G. Gibson, and M. Padgett, "Perspectives on advances in high-capacity, free-space communications using multiplexing of orbital-angular-momentum beams," *Opt. Express*, vol. 24, no. 24, pp. 27 127–27 136, 2016.

[29] L. Zhu and J. Wang, "Demonstration of obstruction-free data-carrying n-fold Bessel modes multicasting from a single Gaussian mode," *Opt. Lett.*, vol. 40, no. 23, pp. 5463–5466, 2015.

[30] M. J. Padgett, "Orbital angular momentum 25 years on," *Opt. Express*, vol. 25, no. 10, pp. 11 265–11 274, 2017.

[31] Q. Zhan, "Cylindrical vector beams: from mathematical concepts to applications," *Adv. Opt. Photonics*, vol. 1, no. 1, pp. 1–57, 2009.

[32] Y.-Q. Zhang, X.-Y. Zeng, R.-R. Zhang, Z.-J. Zhan, X. Li, L. Ma, C.-X. Liu, C.-W. He, and C.-F. Cheng, "Generation of a plasmonic radially polarized vector beam with linearly polarized illumination," *Opt. Lett.*, vol. 43, no. 17, pp. 4208–4211, 2018.

[33] K. Y. Bliokh, F. Rodríguez-Fortuño, F. Nori, and A. V. Zayats, "Spin–orbit interactions of light," *Nat. Photonics*, vol. 9, no. 12, p. 796, 2015.

[34] X. Xie, Y. Chen, K. Yang, and J. Zhou, "Harnessing the point-spread function for high-resolution far-field optical microscopy," *Phys. Rev. Lett.*, vol. 113, no. 26, p. 263901, 2014.

[35] C. Min, Z. Shen, J. Shen, Y. Zhang, H. Fang, G. Yuan, L. Du, S. Zhu, T. Lei, and X. Yuan, "Focused plasmonic trapping of metallic particles," *Nat. Commun.*, vol. 4, p. 2891, 2013.

[36] M. D. Lew and W. Moerner, "Azimuthal polarization filtering for accurate, precise, and robust single-molecule localization microscopy," *Nano Lett.*, vol. 14, no. 11, pp. 6407–6413, 2014.

[37] L. Carretero, P. Acebal, C. Garcia, and S. Blaya, "Periodic trajectories obtained with an active tractor beam using azimuthal polarization: Design of particle exchanger," *IEEE Photonics J.*, vol. 7, no. 1, pp. 1–12, 2015.

[38] N. Bozinovic, Y. Yue, Y. Ren, M. Tur, P. Kristensen, H. Huang, A. E. Willner, and S. Ramachandran, "Terabit-scale orbital angular momentum mode division multiplexing in fibers," *Science*, vol. 340, no. 6140, pp. 1545–1548, 2013.

[39] H. Rubinsztein-Dunlop, A. Forbes, M. V. Berry, M. R. Dennis, D. L. Andrews, M. Mansuripur, C. Denz, C. Alpmann, P. Banzer, and T. Bauer, "Roadmap on structured light," *J. Opt*, vol. 19, no. 1, p. 013001, 2016.

[40] D. Pohl, "Operation of a ruby laser in the purely transverse electric mode TE_{01}," *Appl. Phys. Lett.*, vol. 20, no. 7, pp. 266–267, 1972.

[41] Y. Kozawa and S. Sato, "Generation of a radially polarized laser beam by use of a conical Brewster prism," *Opt. Lett.*, vol. 30, no. 22, pp. 3063–3065, 2005.

[42] M. A. Ahmed, A. Voss, M. M. Vogel, and T. Graf, "Multilayer polarizing grating mirror used for the generation of radial polarization in Yb:YAG thin-disk lasers," *Opt. Lett.*, vol. 32, no. 22, pp. 3272–3274, 2007.

[43] T. Hirayama, Y. Kozawa, T. Nakamura, and S. Sato, "Generation of a cylindrically symmetric, polarized laser beam with narrow linewidth and fine tunability," *Opt. Express*, vol. 14, no. 26, pp. 12 839–12 845, 2006.

[44] T. Su, R. P. Scott, S. S. Djordjevic, N. K. Fontaine, D. J. Geisler, X. Cai, and S. Yoo, "Demonstration of free space coherent optical communication using integrated silicon photonic orbital angular momentum devices," *Opt. Express*, vol. 20, no. 9, pp. 9396–9402, 2012.

[45] P. Yu, S. Chen, J. Li, H. Cheng, Z. Li, W. Liu, B. Xie, Z. Liu, and J. Tian, "Generation of vector beams with arbitrary spatial variation of phase and linear polarization using plasmonic metasurfaces," *Opt. Lett.*, vol. 40, no. 14, pp. 3229–3232, 2015.

[46] A. Arbabi, Y. Horie, M. Bagheri, and A. Faraon, "Dielectric metasurfaces for complete control of phase and polarization with subwavelength spatial resolution and high transmission," *Nat. Nanotechnol.*, vol. 10, no. 11, p. 937, 2015.

[47] Y. He, G. Guo, T. Feng, Y. Xu, and A. E. Miroshnichenko, "Toroidal dipole bound states in the continuum," *Phys. Rev. B*, vol. 98, no. 16, p. 161112, 2018.

[48] W. Buono, L. Moraes, J. Huguenin, C. Souza, and A. Khoury, "Arbitrary orbital angular momentum addition in second harmonic generation," *New J. Phys.*, vol. 16, no. 9, p. 093041, 2014.

[49] G. Gariepy, J. Leach, K. T. Kim, T. J. Hammond, E. Frumker, R. W. Boyd, and P. B. Corkum, "Creating high-harmonic beams with controlled orbital angular momentum," *Phys. Rev. Lett.*, vol. 113, no. 15, p. 153901, 2014.

[50] A. Fleischer, O. Kfir, T. Diskin, P. Sidorenko, and O. Cohen, "Spin angular momentum and tunable polarization in high-harmonic generation," *Nat. Photonics*, vol. 8, no. 7, p. 543, 2014.

[51] A. E. Minovich, A. E. Miroshnichenko, A. Y. Bykov, T. V. Murzina, D. N. Neshev, and Y. S. Kivshar, "Functional and nonlinear optical metasurfaces," *Laser & Photonics Rev.*, vol. 9, no. 2, pp. 195–213, 2015.

[52] W. Ye, F. Zeuner, X. Li, B. Reineke, S. He, C.-W. Qiu, J. Liu, Y. Wang, S. Zhang, and T. Zentgraf, "Spin and wavelength multiplexed nonlinear metasurface holography," *Nat. Commun.*, vol. 7, p. 11930, 2016.

[53] G. Li, S. Zhang, and T. Zentgraf, "Nonlinear photonic metasurfaces," *Nat. Rev. Mater*, vol. 2, no. 5, p. 17010, 2017.

[54] P. Chen, S.-J. Ge, W. Duan, B.-Y. Wei, G.-X. Cui, W. Hu, and Y.-Q. Lu, "Digitalized geometric phases for parallel optical spin and orbital angular momentum encoding," *ACS Photonics*, vol. 4, no. 6, pp. 1333–1338, 2017.

[55] W. Luo, S. Sun, H.-X. Xu, Q. He, and L. Zhou, "Transmissive ultrathin Pancharatnam-Berry metasurfaces with nearly 100% efficiency," *Phys. Rev. Appl.*, vol. 7, no. 4, p. 044033, 2017.

[56] X. Ling, X. Zhou, K. Huang, Y. Liu, C.-W. Qiu, H. Luo, and S. Wen, "Recent advances in the spin hall effect of light," *Rep. Prog. Phys.*, vol. 80, no. 6, p. 066401, 2017.

[57] X. Y. Xiong, A. Al-Jarro, L. J. Jiang, N. C. Panoiu, and E. Wei, "Mixing of spin and orbital angular momenta via second-harmonic generation in plasmonic and dielectric chiral nanostructures," *Phys. Rev. B*, vol. 95, no. 16, p. 165432, 2017.

[58] G. Li, L. Wu, K. F. Li, S. Chen, C. Schlickriede, Z. Xu, S. Huang, W. Li, Y. Liu, E. Y. Pun, T. Zentgraf, K. W. Cheah, Y. Luo, and S. Zhang, "Nonlinear metasurface for simultaneous control of spin and orbital angular momentum in second harmonic generation," *Nano Lett.*, vol. 17, no. 12, pp. 7974–7979, 2017.

[59] S. Keren-Zur, L. Michaeli, H. Suchowski, and T. Ellenbogen, "Shaping light with nonlinear metasurfaces," *Adv. Opt. Photonics*, vol. 10, no. 1, pp. 309–353, 2018.

[60] H.-X. Xu, G. Hu, Y. Li, L. Han, J. Zhao, Y. Sun, F. Yuan, G.-M. Wang, Z. H. Jiang, X. Ling, T. J. Cui, and C.-W. Qiu, "Interference-assisted kaleidoscopic meta-plexer for arbitrary spin-wavefront manipulation," *Light: Science & Applications*, vol. 8, no. 1, p. 3, 2019.

[61] P. Li, I. Dolado, F. J. Alfaro-Mozaz, F. Casanova, L. E. Hueso, S. Liu, J. H. Edgar, A. Y. Nikitin, S. Vélez, and R. Hillenbrand, "Infrared hyperbolic metasurface based on nanostructured van der Waals materials," *Science*, vol. 359, no. 6378, pp. 892–896, 2018.

[62] C.-H. Liu, J. Zheng, S. Colburn, T. K. Fryett, Y. Chen, X. Xu, and A. Majumdar, "Ultrathin van der Waals metalenses," *Nano Lett.*, vol. 18, no. 11, pp. 6961–6966, 2018.

[63] X. Hong, G. Hu, W. Zhao, K. Wang, S. Sun, R. Zhu, J. Wu, W. Liu, K. P. Loh, A. T. S. Wee, B. Wang, Alù, C.-W. Qiu, and P. Lu, "Structuring nonlinear wavefront emitted from monolayer transition-metal dichalcogenides," *Research*, vol. 2020, p. 9085782, 2020.

[64] F. Spreyer, R. Zhao, L. Huang, and T. Zentgraf, "Second harmonic imaging of plasmonic Pancharatnam-Berry phase metasurfaces coupled to monolayers of WS_2," *Nanophotonics*, vol. 9, no. 2, pp. 351–360, 2020.

[65] S. Yang, D. C. Liu, Z. L. Tan, K. Liu, Z. H. Zhu, and S. Q. Qin, "CMOS-compatible WS_2-based all-optical modulator," *ACS Photonics*, vol. 5, no. 2, pp. 342–346, 2018.

[66] M.-H. Chiu, H.-L. Tang, C.-C. Tseng, Y. Han, A. Aljarb, J.-K. Huang, Y. Wan, J.-H. Fu, X. Zhang, W.-H. Chang, D. A. Muller, T. Takenobu, V. Tung, and L.-J. Li, "Metal-guided selective growth of 2d materials: Demonstration of a bottom-up CMOS inverter," *Adv. Mater.*, vol. 31, no. 18, p. 1900861, 2019.

[67] L. M. Malard, T. V. Alencar, A. P. M. Barboza, K. F. Mak, and A. M. de Paula, "Observation of intense second harmonic generation from MoS_2 atomic crystals," *Phys. Rev. B*, vol. 87, no. 20, p. 201401, 2013.

[68] H. Zeng, G.-B. Liu, J. Dai, Y. Yan, B. Zhu, R. He, L. Xie, S. Xu, X. Chen, W. Yao, and X. Cui, "Optical signature of symmetry variations and spin-valley coupling in atomically thin tungsten dichalcogenides," *Sci. Rep.*, vol. 3, p. 1608, 2013.

[69] M. C. Lucking, K. Beach, and H. Terrones, "Large second harmonic generation in alloyed TMDs and boron nitride nanostructures," *Sci. Rep.*, vol. 8, no. 1, pp. 1–13, 2018.

[70] Z. Bomzon, G. Biener, V. Kleiner, and E. Hasman, "Space-variant Pancharatnam-Berry phase optical elements with computer-generated subwavelength gratings," *Opt. Lett.*, vol. 27, no. 13, pp. 1141–1143, 2002.

[71] M. L. Chen, L. J. Jiang, and W. E. Sha, "Artificial perfect electric conductor-perfect magnetic conductor anisotropic metasurface for generating orbital angular momentum of microwave with nearly perfect conversion efficiency," *J. Appl. Phys.*, vol. 119, no. 6, 2016.

[72] R. Ottens, V. Quetschke, S. Wise, A. Alemi, R. Lundock, G. Mueller, D. H. Reitze, D. B. Tanner, and B. F. Whiting, "Near-field radiative heat transfer between macroscopic planar surfaces," *Phys. Rev. Lett.*, vol. 107, no. 1, p. 014301, 2011.

[73] A. Narayanaswamy and N. Gu, "Heat transfer from freely suspended bimaterial microcantilevers," *J. Heat Transfer*, vol. 133, no. 4, 2011.

[74] A. W. Rodriguez, M. H. Reid, and S. G. Johnson, "Fluctuating-surface-current formulation of radiative heat transfer: Theory and applications," *Phys. Rev. B*, vol. 88, no. 5, p. 054305, 2013.

[75] C. R. Otey, L. Zhu, S. Sandhu, and S. Fan, "Fluctuational electrodynamics calculations of near-field heat transfer in non-planar geometries: A brief overview," *J. Quant. Spectrosc. Radiat. Transfer*, vol. 132, pp. 3–11, 2014.

[76] O. Ilic, M. Jablan, J. D. Joannopoulos, I. Celanovic, H. Buljan, and M. Soljačić, "Near-field thermal radiation transfer controlled by plasmons in graphene," *Phys. Rev. B*, vol. 85, no. 15, p. 155422, 2012.

[77] A. Volokitin and B. Persson, "Near-field radiative heat transfer between closely spaced graphene and amorphous SiO_2," *Phys. Rev. B*, vol. 83, no. 24, p. 241407, 2011.

[78] X. Liu and Z. Zhang, "Graphene-assisted near-field radiative heat transfer between corrugated polar materials," *Appl. Phys. Lett.*, vol. 104, no. 25, p. 251911, 2014.

[79] X. Liu and Z. Zhang, "Giant enhancement of nanoscale thermal radiation based on hyperbolic graphene plasmons," *Appl. Phys. Lett.*, vol. 107, no. 14, p. 143114, 2015.

[80] V. Svetovoy, P. Van Zwol, and J. Chevrier, "Plasmon enhanced near-field radiative heat transfer for graphene covered dielectrics," *Phys. Rev. B*, vol. 85, no. 15, p. 155418, 2012.

[81] P. Van Zwol, S. Thiele, C. Berger, W. De Heer, and J. Chevrier, "Nanoscale radiative heat flow due to surface plasmons in graphene and doped silicon," *Phys. Rev. Lett.*, vol. 109, no. 26, p. 264301, 2012.

[82] R. Messina, P. Ben-Abdallah, B. Guizal, and M. Antezza, "Graphene-based amplification and tuning of near-field radiative heat transfer between dissimilar polar materials," *Phys. Rev. B*, vol. 96, no. 4, p. 045402, 2017.

[83] F. V. Ramirez, S. Shen, and A. J. McGaughey, "Near-field radiative heat transfer in graphene plasmonic nanodisk dimers," *Phys. Rev. B*, vol. 96, no. 16, p. 165427, 2017.

[84] B. Liu, Y. Liu, and S. Shen, "Thermal plasmonic interconnects in graphene," *Phys. Rev. B*, vol. 90, no. 19, p. 195411, 2014.

[85] P. Ben-Abdallah, A. Belarouci, L. Frechette, and S.-A. Biehs, "Heat flux splitter for near-field thermal radiation," *Appl. Phys. Lett.*, vol. 107, no. 5, p. 053109, 2015.

[86] R. Yu, A. Manjavacas, and F. J. G. De Abajo, "Ultrafast radiative heat transfer," *Nat. Commun.*, vol. 8, no. 1, pp. 1–13, 2017.

[87] K. S. Novoselov, V. Fal, L. Colombo, P. Gellert, M. Schwab, K. Kim et al., "A roadmap for graphene," *Nature*, vol. 490, no. 7419, pp. 192–200, 2012.

[88] V. Nayyeri, M. Soleimani, and O. M. Ramahi, "Modeling graphene in the finite-difference time-domain method using a surface boundary condition," *IEEE Trans. Antennas Propag.*, vol. 61, no. 8, pp. 4176–4182, 2013.

[89] J. D. Jackson, *Classical Electrodynamics*, John Wiley & Sons, 1999.

[90] K. Zhang, Y. Huang, A. E. Miroshnichenko, and L. Gao, "Tunable optical bistability and tristability in nonlinear graphene-wrapped nanospheres," *J. Phys. Chem. C*, vol. 121, no. 21, pp. 11 804–11 810, 2017.

[91] Z. M. Zhang, *Nano/Microscale Heat Transfer*. Springer, 2007.

[92] S. Basu, Z. Zhang, and C. Fu, "Review of near-field thermal radiation and its application to energy conversion," *Int. J. Energy Res.*, vol. 33, no. 13, pp. 1203–1232, 2009.

[93] S. M. Rytov, Y. A. Kravtsov, and V. I. Tatarskii, *Principles of Statistical Radiophysics 2. Correlation Theory of Random Processes*, 1989.

[94] W. Eckhardt, "Macroscopic theory of electromagnetic fluctuations and stationary radiative heat transfer," *Phys. Rev. A*, vol. 29, no. 4, p. 1991, 1984.

[95] M. Krüger, G. Bimonte, T. Emig, and M. Kardar, "Trace formulas for nonequilibrium Casimir interactions, heat radiation, and heat transfer for arbitrary objects," *Phys. Rev. B*, vol. 86, no. 11, p. 115423, 2012.